

# Novel Transmission Thermal Model

*The creation and analysis of a thermal model that can predict the steady-state temperature of a novel planetary friction transmission*

T.J. Verschoor

**Aerospace Master Thesis:**  
Flight Performance and Propulsion

SN: 4001346



# Novel Transmission Thermal Model

*The creation and analysis of a thermal model that  
can predict the steady-state temperature of a novel  
planetary friction transmission*

by

T.J. Verschoor

to obtain the degree of Master of Science  
at the Delft University of Technology,  
to be defended on Thursday August 16, 2018 at 14:00.

Student number: 4001346  
Project duration: October 1, 2017 – June 30, 2018  
Thesis committee: Dr. ir. W.A.A.M. Bierbooms, TU Delft, supervisor  
Dr. ir. R.A.J. van Ostayen, TU Delft  
Prof. dr. S.J. Watson, TU Delft

*This thesis is confidential and cannot be made public until July 31, 2020.*

An electronic version of this thesis is available at <http://repository.tudelft.nl/>.



# Abstract

In this thesis, a thermodynamic model of a novel traction transmission in an off-shore wind turbine was created. This system relies on friction rather than gear teeth to transfer torque, improving multiple characteristics compared to current transmissions. It is not yet known how much heat this novel system will generate therefore a general thermal model was developed to calculate the steady-state temperature as a function of the transmission's geometry and operating conditions. This model could then be used early in the designing process of similar transmissions.

To create the thermal model an analysis was conducted in multiple parts. The first part of the analysis was to determine the relations governing the heat generation. Then, the heat transfer relations for the system were determined using preliminary assumptions. It was concluded that conduction and convection are dominant inside the transmissions while radiation and convection are dominant outside the transmission. Using the appropriate heat transfer relations a nodal network of the transmission was created to determine the temperature at a given point on the system's cross-section. Each node in this network has a unique heat transfer relation which is dependent on its position in the system. The temperature was assumed to be homogeneous around the circumference, therefore the model only takes the radial and axial heat transfer into consideration. This set of non-linear heat transfer equations was then solved simultaneously to determine the steady-state temperature. The results of the model are shown on a heat map representing the transmission's cross-section.

The model was then verified and validated. To verify the model at a given phase, the results of a third party software (ANSYS) were compared with that of the thermal model using the same inputs and boundary conditions. There was a strong relation between the two methods, verifying the thermal model at a given phase. Validation was conducted with a scaled model of the transmission's working principle found in the wind-turbine. The model was operated at multiple constant input rotational speeds until steady-state condition was reached. Those measured temperatures were then compared with the results of the model. The validation procedure showed that there was a difference in temperature between the thermal model and the validation test. This difference was because the model did not incorporate conduction from the transmission to the external environment. Once the validation procedure was altered to remove conduction from the test, the results of the thermal model related with that of the validation tests.

The verified and validated model was then used to predict the steady-state temperature of the wind-turbine transmission. Using the model it was concluded that the type of lubrication used by the transmission plays a critical role in the final temperature. The steady-state temperature of the un-lubricated case could be determined using the model. Additional tests are required before the model can predict the temperature for lubricated cases.

## Nomenclature

Variable	Description
$A$	Area
$a$	Thermal diffusivity
$B$	Bearing width
$C_s$	Static basic load
$c$	Thermal conduction
$C_p$	Specific heat capacity at constant pressure
$D$	Diameter
$d_m$	Bearing pitch diameter
$F$	Radial or axial force
$f_o$	Bearing lubrication factor
$f_l$	Torque due to applied load factor
$G_D$	Body gravity function
$Gr$	Grashof number
$g$	Gravitational acceleration
$H$	Thermal energy
$h_v$	Film coefficient of heat transfer
$J(X)$	Jacobian matrix
$k$	Thermal conductivity coefficient
$L$	Length
$M$	Friction moment
$m$	Mass of the transmission
$Nu$	Nusselt number
$n$	Rotational velocity
$P$	Power of system
$Pr$	Prandtl number
$Q$	Normal load
$R$	Thermal resistance
$Ra$	Rayleigh number
$R_{i,o}$	Inner and outer radii
$R$	Thermal radiation
$S$	Surface area
$S_D$	Shape factor
$step$	Flex-roller step size
$T$	Temperature
$u$	Bearing cage/flow velocity
$v$	Thermal convection
$V_{1-4}$	Velocity of flex-roller sections
$\nu_o$	Kinematic viscosity
$v_{nxj}$	Sliding velocity on contact surface
$W$	Width of annular structure
$x$	Bearing pitch diameter
$Z$	Number of flex-rollers
$\alpha$	Bearing contact angle
$\beta$	Volume coefficient of expansion
$\epsilon$	Thermal emissivity
$\eta$	Efficiency
$\mu$	Coefficient of friction
$\mu_o$	Dynamic viscosity
$\epsilon$	Thermal emissivity

# List of Figures

2.1	Overview of geared and direct drive wind turbines . . . . .	5
2.2	Layout of a wind turbine drive-train . . . . .	6
2.3	Overview of a three stage wind turbine gearbox . . . . .	6
2.4	DOT concept internal layout . . . . .	7
2.5	DOT concept . . . . .	8
2.6	Working principle of a planetary drive compared to an Archimedes drive . . . . .	9
2.7	Archimedes drive working principle . . . . .	9
2.8	Overview of the DOT gearing system . . . . .	10
2.9	Asymmetric drive & symmetric drive Archimedes drive . . . . .	11
2.10	Components in DOT transmission . . . . .	11
4.1	Deformation of a roller and the raceway . . . . .	16
4.2	Roller-raceway contact . . . . .	16
4.3	Rolling and spinning velocities . . . . .	16
4.4	Contact ellipse showing point of pure rolling and sliding lines . . . . .	16
4.5	Bearing series illustration . . . . .	19
4.6	The front and simplified side view of a flex-roller . . . . .	20
4.7	The effect of flex-roller geometry on velocity . . . . .	20
4.8	Decomposition of flex-roller velocity profile . . . . .	21
4.9	Illustration of SKF 61804 deep-groove ball bearing . . . . .	22
4.10	Illustration of desired solver 1D paths . . . . .	24
4.11	Nodal network notation used in the thermal model . . . . .	24
5.1	Overview of the model with all key components (not to scale) . . . . .	29
5.2	Example of a single node calculation . . . . .	30
5.3	Illustration of structure components . . . . .	31
5.4	Convective heat transfer interaction . . . . .	31
5.5	Illustration of the flex-roller geometry with node . . . . .	32
5.6	Illustration of flex-roller node simplification . . . . .	32
5.7	Overview of flex-roller nodal network . . . . .	33
5.8	Illustration of circle-circle intersection [28] . . . . .	33
5.9	Location of the area that needs to be calculated . . . . .	33
5.10	Detailed overview of flex-roller node interaction in the flex-roller section . . . . .	34
5.11	Thermal resistance in axial direction in the flex-roller section . . . . .	35
5.12	Thermal resistance in radial direction in the flex-roller section . . . . .	35
5.13	Illustration of the steps taken in the program . . . . .	36
5.14	Example result of thermal model . . . . .	37
5.15	Geometry used in nodal density example . . . . .	40
5.16	The effect of node size on the resulting heat-map . . . . .	40
5.17	Computational time as a function of node size . . . . .	41
6.1	Illustration of geometry used in solver verification . . . . .	44
6.2	Illustration of the nodes in solver verification . . . . .	44
6.3	The change in temperature T2 as a function of T1 in solver verification . . . . .	46
6.4	Heat-map generated by the thermal model . . . . .	47
6.5	Heat-map generated by ANSYS . . . . .	47
6.6	Illustration of geometry . . . . .	47
6.7	Temperature distribution 3D . . . . .	48
6.8	Temperature distribution 2D cut-out . . . . .	48

6.9	Temperature distribution thermal model . . . . .	48
6.10	Temperature distribution ansys . . . . .	48
6.11	Transmission used for validation . . . . .	49
6.12	Dimensions of validation transmission with bearing locations . . . . .	49
6.13	Working principle of validation drive . . . . .	50
6.14	Flex-roller velocities of validation drive . . . . .	50
6.15	Bearing type and dimensions . . . . .	50
6.16	Validation test-bench . . . . .	51
6.17	The thermocouple numbering . . . . .	51
6.18	An overview of the modification to the test set-up . . . . .	52
6.19	Maximum operating rotational velocity and temperature of validation transmission . . . . .	53
6.20	Steady-state temperature of validation transmission without thermal insulation . . . . .	54
6.21	Torque and power of validation transmission without thermal insulation . . . . .	54
6.22	Steady-state temperature of validation transmission with thermal insulation . . . . .	55
6.23	Torque and power of validation transmission with thermal insulation . . . . .	56
6.24	Caged cylindrical roller bearing and full-complement roller bearing . . . . .	57
6.25	Illustration of cage in validation transmission with location of components . . . . .	58
6.26	Power as a function of rotational velocity for validation transmission . . . . .	59
6.27	Input geometry used in thermodynamic model for validation transmission . . . . .	59
6.28	Validation transmission steady-state temperature at 45 rad/s . . . . .	60
6.29	Illustration of test-bench simulation used in ANSYS . . . . .	60
6.30	Steady-state temperature at 45 rad/s with thermal insulation . . . . .	61
6.31	Steady-state temperature at 55 rad/s without thermal insulation . . . . .	61
6.32	Modified validation transmission housing used in the ANSYS simulation . . . . .	61
6.33	Steady-state temperature as a function of input rotational velocity for validation transmission . . . . .	62
6.34	The 3D results from the ANSYS simulation of the validation transmission . . . . .	62
6.35	The 2D section plane results from the ANSYS simulation of the validation transmission . . . . .	62
6.36	Ambient temperature sensitivity analysis . . . . .	64
6.37	Torque due to applied load factor sensitivity analysis . . . . .	64
6.38	Conduction coefficient sensitivity analysis . . . . .	65
6.39	Change in temperature as a function of change in input variable . . . . .	65
7.1	The dimensions in DOT transmission . . . . .	67
7.2	The dimensions of the flex-roller . . . . .	68
7.3	Heat-map of the DOT system under minimum grease condition . . . . .	69
7.4	Heat power of the DOT transmission . . . . .	70
8.1	Flow-chart comparing traditional heat analysis to the thermal model . . . . .	75
10.1	Chain transmission . . . . .	81
10.2	Gear transmission . . . . .	81
10.3	Comparing gear teeth to friction transmission . . . . .	82
10.4	Comparing the different drive technologies . . . . .	83
10.5	Backlash illustration . . . . .	83
11.1	Overview and positioning of market . . . . .	85
11.2	Market forecast of wind turbine industry . . . . .	86
11.3	Wind supplier global market . . . . .	86
11.4	Component layout of geared wind turbine . . . . .	87
11.5	Wind turbine gearbox supplier market share . . . . .	88
11.6	The growth in industrial robots market . . . . .	89
11.7	Market share of industrial robot manufactures . . . . .	90
11.8	Collaborative robots . . . . .	91
11.9	Market share of drive manufactures . . . . .	91
11.10	Annual sales EV industry . . . . .	93
11.11	Top Selling EV in Europe by brand [61] . . . . .	93

A.1	Values for $f_o$ . . . . .	107
A.2	Values for $f_f$ . . . . .	108
A.3	Values for z and y . . . . .	108
A.4	Values for $f_1$ for roller bearings . . . . .	108
A.5	Values for X and Y for radial ball bearings . . . . .	109
A.6	Values for X and Y for radial roller bearings . . . . .	109



# List of Tables

2.1	The name and numbering of the components in the DOT transmission . . . . .	11
4.1	SKF 61804 dimensions and data [18] . . . . .	22
4.2	Heat transfer types present in the transmission system . . . . .	23
4.3	Heat transfer chart of all components in the DOT transmission . . . . .	23
5.1	Input variables in nodal density example . . . . .	40
6.1	Input variables in solver verification program . . . . .	44
6.2	The heat of the nodes used in solver verification under different input situations . . . . .	46
6.3	Input variables in roller verification . . . . .	47
6.4	Design requirements . . . . .	50
6.5	Thermocouple location description . . . . .	51
6.6	Bearing heat power for validation test . . . . .	57
6.7	Comparing heat power values calculated by the thermal model with the measured values . . . . .	59
7.1	DOT bearing dimensions . . . . .	67
7.2	Dimensions and variables of the DOT transmission . . . . .	68
7.3	DOT Transmission Bearing Variables . . . . .	68
7.4	Maximum steady-state temperature and thermal efficiency of DOT transmission . . . . .	70
11.1	Wind turbine component weight and cost . . . . .	87
12.1	Estimated production costs . . . . .	98



# Contents

<b>List of Figures</b>	<b>v</b>
<b>List of Tables</b>	<b>ix</b>
<b>I Aerospace Engineering Thesis</b>	<b>1</b>
<b>1 Introduction</b>	<b>3</b>
<b>2 Wind Turbine Transmissions</b>	<b>5</b>
2.1 Geared and Direct Drive Wind Turbines. . . . .	5
2.2 The DOT Concept. . . . .	7
2.3 Transmission Concept . . . . .	8
2.4 Drive-Train Heating. . . . .	11
<b>3 Research Objective</b>	<b>13</b>
<b>4 Theory of the Thermal Model</b>	<b>15</b>
4.1 Heat Generation . . . . .	15
4.1.1 Main Forms of Heat Generation . . . . .	15
4.1.2 Empirical Relations . . . . .	17
4.1.3 Flex-Roller Heat Generation . . . . .	19
4.1.4 Bearing Heat Calculation . . . . .	22
4.2 Heat Dissipation . . . . .	23
4.2.1 Nodal Network. . . . .	23
4.2.2 Conduction . . . . .	25
4.2.3 Convection. . . . .	25
4.2.4 Radiation . . . . .	27
4.2.5 Heat Transfer in Series and Parallel . . . . .	28
<b>5 The Thermal Model</b>	<b>29</b>
5.1 Modeling Approach . . . . .	29
5.1.1 Modeling the General Structure . . . . .	30
5.1.2 Modeling the Flex-Rollers . . . . .	31
5.2 Non-Linear Equation Solver . . . . .	36
5.3 Program Explanation . . . . .	36
5.3.1 Working Principle of Model . . . . .	37
5.3.2 Nodal Density . . . . .	40
<b>6 Verification and Validation</b>	<b>43</b>
6.1 Verification . . . . .	43
6.1.1 Simultaneous Equation Solver Verification. . . . .	43
6.1.2 Simple Geometry Verification . . . . .	46
6.2 Validation. . . . .	49
6.2.1 The Test Set-Up . . . . .	49
6.2.2 The Test Procedure. . . . .	52
6.2.3 The Results. . . . .	53
6.2.4 Heat Power Validation . . . . .	56
6.2.5 Steady-State Temperature Validation. . . . .	59
6.2.6 Sensitivity Analysis. . . . .	63
<b>7 Full Scale Prediction</b>	<b>67</b>
7.1 Requirements, Dimensions and Assumptions. . . . .	67
7.2 Prediction Results. . . . .	69

<b>8</b>	<b>Evaluation, Conclusion and Future Work</b>	<b>73</b>
8.1	Evaluation and Conclusion . . . . .	73
8.2	Outlook and Future Work . . . . .	76
<b>II</b>	<b>Annotation Entrepreneurship</b>	<b>77</b>
<b>9</b>	<b>Introduction Annotation Entrepreneurship</b>	<b>79</b>
<b>10</b>	<b>Innovation Explanation</b>	<b>81</b>
10.1	Current Technologies . . . . .	81
10.2	The Innovation . . . . .	82
<b>11</b>	<b>Market Analysis</b>	<b>85</b>
11.1	Wind Turbines . . . . .	86
11.1.1	Market Background and Size. . . . .	86
11.1.2	Competitors . . . . .	87
11.1.3	Value Proposition . . . . .	88
11.2	Robotics . . . . .	89
11.2.1	Market Background and Size. . . . .	89
11.2.2	Competitors . . . . .	91
11.2.3	Value Proposition . . . . .	92
11.3	Electric Vehicles. . . . .	93
11.3.1	Market Background and Size. . . . .	93
11.3.2	Competitors . . . . .	94
11.3.3	Value Proposition . . . . .	95
11.4	Market Penetration Strategy. . . . .	95
<b>12</b>	<b>Business Plan</b>	<b>97</b>
12.1	Producing the Technology . . . . .	97
12.2	Licensing the Technology . . . . .	98
12.3	Intellectual Property Protection. . . . .	99
<b>13</b>	<b>Conclusion Annotation Entrepreneurship</b>	<b>101</b>
	<b>Bibliography</b>	<b>103</b>
<b>A</b>	<b>Calculation Tables</b>	<b>107</b>

# I

## Aerospace Engineering Thesis



# Introduction

The company Delft Offshore Turbines (hereinafter: DOT) is developing a new wind turbine for the off-shore industry. In this turbine a new gearing system is used which relies on friction and elastic deformation of steel rather than gear teeth to transfer torque. This new method of transferring torque could result in an increase in heat in the system, affecting its performance. The full extent of the heat that is generated is not fully known and needs to be investigated. In the thesis this new system is analyzed and a general thermal model (also referred to as thermodynamic model) is created to predict the heat behavior for this specific transmission. This general model reduces the computational time of traditional methods and would be able to be used earlier in the development process.

During this process, well documented thermodynamic relations will be used extensively. The heat increase of different materials during frictional contact and their interaction with one another will need to be analyzed. Additionally, all other critical locations regarding to heat generation will be investigated. Once the heat is generated, the thermal conduction, convection and radiation in the system with multiple movable parts needs to be determined. The resulting model which will predict the thermal characteristics will have to be applicable to a variety of transmission sizes. This thesis combines material thermodynamics in combination with heat transfer.

The research in this report consists of multiple parts. The first is the thermodynamic analysis of rolling components to determine how much heat is being generated. Then, through the use of conduction, convection and radiation theory, an analysis is conducted on the heat propagating through the system. From these results a detailed general model is created which can predict the steady-state thermal behavior of this traction based transmission. This model is then validated with a scaled model of the transmission used in the wind turbine to determine the accuracy. Finally, using the gathered information a prediction is made to determine the final steady-state temperature of the transmission used in the DOT system.

This report is split into multiple chapters, each focusing on a different topic. Firstly, in chapter 2, an overview of the problem is given by discussing current wind turbine transmissions and explaining what makes the DOT system unique. Using this, the current state-of-the-art of thermodynamic models for this specific transmission is discussed and the reason why the model is novel is given. Then in chapter 3, the research questions is given focusing on different aspects of the model. Using those research questions, chapter 4 gives the thermodynamic theory behind the model. Once given, an overview of the the complete model and its working principles is shown in chapter 5. That model is then verified and validated in chapter 6, using a third party thermodynamic software (ANSYS) and a scaled model of the wind turbine transmission. The knowledge gained during this thermodynamic analysis is then used to calculate the steady-state temperature of the complete wind turbine transmission used in the DOT systems in chapter 7.



# 2

## Wind Turbine Transmissions

This chapter gives an overview of current wind turbine transmission technology. Currently, there are two main types of wind turbines, these are, geared systems and direct drive systems, an explanation for both of those systems is given in section 2.1. Once given, the novelty of the DOT system is discussed in section 2.2. That section is followed by an explanation of the working principle for the novel transmission used in the DOT wind turbine, given in section 2.3. This chapter concludes with section 2.4, which is an explanation of the heat sources in current wind turbine drive-trains and how they differ from the DOT system.

### 2.1. Geared and Direct Drive Wind Turbines

Wind turbines for large-scale power generation can be split into two main categories these are geared and direct drive. A schematic of both types of wind turbines is shown in figure 2.1. Both types of wind turbines are in use today with around 70% of installed wind turbines being geared systems.[38] However, direct drive wind turbines are becoming more popular and are expected to increase their market share the coming years. Both of these types of turbines have positive and negative aspects which need to be considered before a design is chosen.

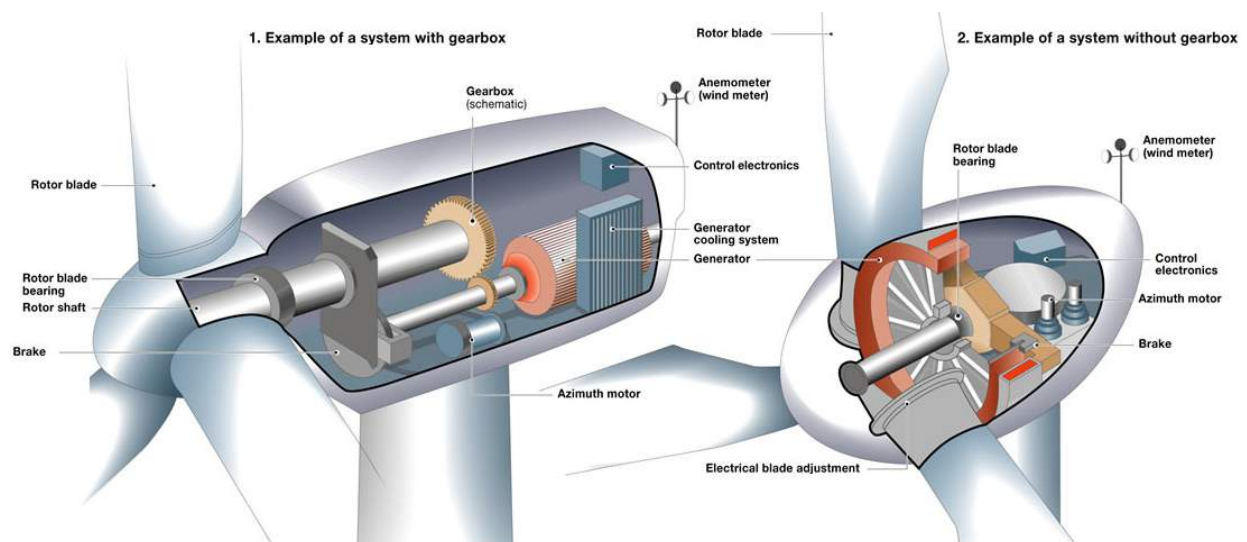


Figure 2.1: Overview of geared (left) and direct drive (right) wind turbines [3]

Geared wind turbines have been in use the longest, with the first mega-watt class being installed in 1941 in the United States.[4] Since then, great progress has been made in the overall reliability and performance of geared wind turbines. As stated in its name, geared wind turbines use a transmission to alter the torque and rotational velocity of the drive-train between the rotor and the generator. A transmission is used within a

wind turbine to transfer the wind energy captured by the blades to electrical energy within the generator. The transmission is placed in between the shaft directly connected to the blades and the shaft running through the electrical generator, this is shown in figure 2.2. The main purpose of the transmission is to alter the high torque and low rotational velocity input to a low torque and high rotational velocity output. This is because most wind turbine generators work effectively at higher speeds.

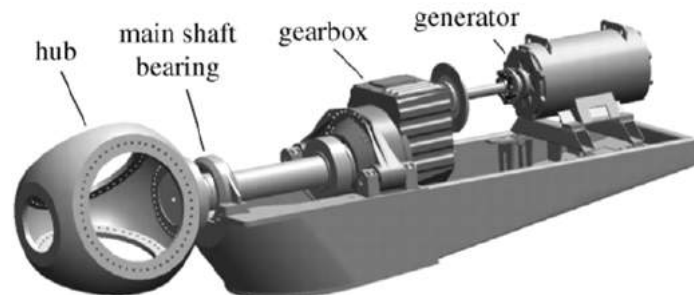


Figure 2.2: Layout of a wind turbine drive-train consisting of the hub, main shaft bearing, gearbox and generator [1]

The gearing in the transmission converts the rotational velocity from between 15 to 20 rpm to around 1,800 rpm.[5] In general the gear ratio is around 1:90 but for some applications it could be as low as 1:30.[2] A gear ratio of 1:90 means that the output rotational speed is 90 times greater than the input. Most commonly, the transmission is a planetary system and is divided into three parts, where the complete gear ratio is split into separate gearing stages, each adding up to final requirement, as shown in figure 2.3.

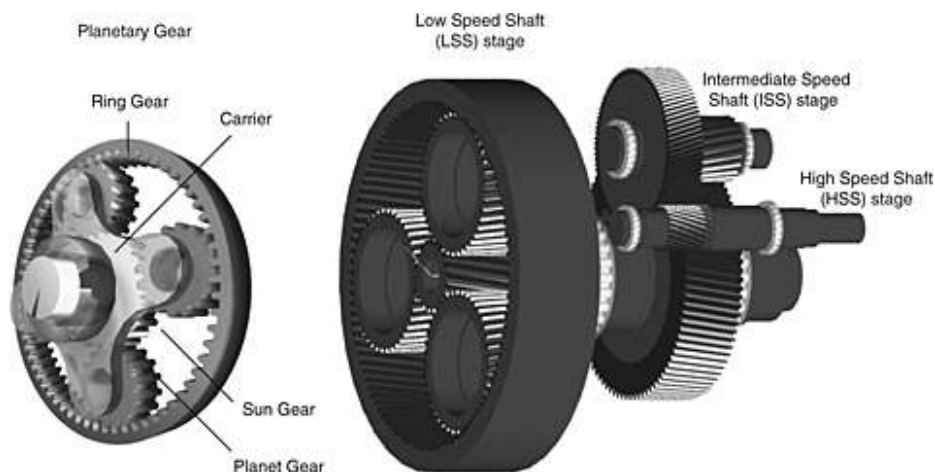


Figure 2.3: Overview of a three stage wind turbine gearbox consisting of a low (input), intermediate and high speed (output) shaft stage [6]

The low speed shaft is connected to the rotor blades and the high speed shaft to the generator. Using a transmission allows for the implementation of a simple generator, greatly decreasing the initial cost and weight of the turbine. The transmission system also has to operate in challenging loading and environmental conditions. This is because the torque of the rotor applies large forces and moments on the drive-train. Meaning that the transmission must withstand those forces while being able to generate power. Wind turbines are also placed in demanding environments with large fluctuations in temperature and humidity, all affecting the durability of the system. Therefore, the system must be robust enough to decrease the build-up of moisture, rust and dirt. The transmission also experiences a wide range of loading cases that must be accounted for in the design. During start-up, shut-down, emergency stops and normal operation the loads can vary greatly, design choices must be made to incorporate all those different loading cases. These aspects result in the transmission being one of the subsystems of the drive-train which require the most maintenance and also makes them difficult and expensive to exchange.

Due to their long operational lifespan all failure modes need to be analyzed. Some of these include gear

tooth breakage, manufacturing error, grind temper, material inclusion, surface related problems and fretting problems. Additionally, a wind turbine transmission can suffer from design issues. These are a few of the many aspects that need to be taken into consideration to design a transmission for a wind turbine. Improving on those aspects is crucial for the future development of this technology. Older wind turbine models that are still in operation need to be serviced annually because of these issues.[5] The most frequent failures arise from the particles released by the continually rotating bearings which contaminate the gear teeth.[5] Additionally, surface wear and misalignment also affect the performance after numerous cycles. These problems have become significantly less as manufacturing and installation techniques have improved but will always remain present to a certain degree. During the design process there will always be a trade-off between the number of stages, the reliability of the transmission and the costs of the generator.[2]

Direct drive wind turbines have become more popular over the years. These wind turbines started being used in the early 2000's for large scale power generation. Instead of having a transmission system in the nacelle, the drive-train connects the rotor blades directly to the generator. Doing this removes the need for a gearbox, reducing the maintenance requirement of the wind turbine. The draw-back of this system is that it requires the use of a low-speed generator which is more expensive and heavier compared to the high speed generators used in traditional geared systems.[4] Currently, progress is being made in low speed generators which would bring down the cost, making direct drive wind turbines more competitive. Overall, these systems are preferred in remote areas due to their lower long-term maintenance costs. However, the initial costs of such a system is still a major issue that needs to be resolved before this technology can be fully adopted.

While looking at these two technologies for the off-shore wind turbine industry, a clear choice needs to be made by the customer before choosing a system. On one side there are geared wind turbines, these have a lower initial cost but could result in higher maintenance costs due to reliability issues. The other option, direct drive, is more reliable for off-shore applications but results in much higher initial costs. There seems to be no technology currently available that has good reliability while still having a relatively minimum initial investment requirement. The DOT system explained further in section 2.2 tries to solve this problem by having both lower installation and maintenance costs.

## 2.2. The DOT Concept



Figure 2.4: DOT concept internal layout (Right) compared to traditional geared windturbines (Left) [7]

A traditional wind turbine generates electricity from the generator placed in its nacelle. This is beneficial for on-shore wind farms since power can be generated by a single unit and wind farms situated on land are generally easily accessible. However, for off-shore applications accessibility becomes an issue, that is why a better solution was found using the water surrounding the wind turbine's platform. DOT is developing a revolutionary new off-shore wind turbine which can drastically reduce the cost of installation and maintenance. This is

done by replacing the conventional mechanical-electrical drive with a water pump, shown in figure 2.4 on the right.

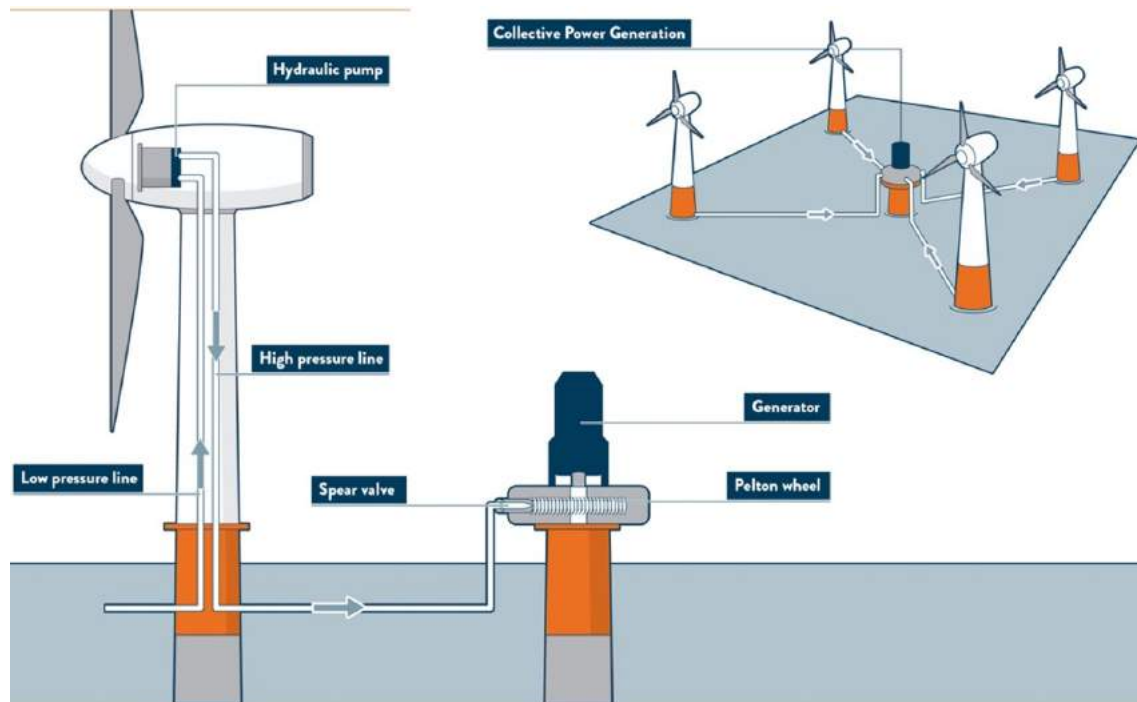


Figure 2.5: DOT illustration indicating the working principle of the complete system [7]

The wind turbine layout shown in figure 2.5 allows the system to pump sea water to a stationary central generator platform, removing the need for a generator in each nacelle of the wind turbine. The pump used to pressurize the water is placed in the wind turbine's hub, directly connected to the rotor blades. A transmission located around the pump is used to transfer the torque from the rotor to the water pump's pistons. This layout requires all sub-systems to be compact while still being strong enough to transfer the required torque for the pump. The pump operates at a different rotational velocity than the blades requiring the use of a gearbox. The gearbox needs to have a gear ratio of 1:20 with an input velocity of 28 rpm and needs to withstand a torque of 280 kNm.[8] The transmission would also need to be hollow from the inside to leave room for the pump. Current available transmissions used in existing wind turbine applications are not able to meet these requirements therefore a new transmission was developed. This transmission concept is explained in more detail in section 2.3.

### 2.3. Transmission Concept

The DOT wind turbine uses a novel transmission that combines the working principle of established technologies. This transmission, named the Archimedes drive[9] , is referred to as a 'compound planetary friction drive'. Therefore, the three working principles which are combine to form this novel transmission are planetary , friction and compound based transmission principles. These principles are explained at the beginning of this section. Once explained, the section will conclude with a description of the working principle for the transmission used in the DOT wind turbine.

Planetary transmissions (also called planetary drives) are used frequently in wind turbine gearboxes, illustrated as the low speed shaft (LSS) stage in the transmission shown in figure 2.3. This transmission consists out of an outer fixed ring gear (ground annulus) with a sun gear positioned in the middle of it. Between the two gears there are multiple circular gears (planets) meshing to the teeth of the sun and fixed ring gear. The planet wheel carrier, attached to all the planets, receives rotational input from the blades. These planets then rotate around the fixed ring gear (ground annulus). Fixing the ring gear, forces the sun gear (located in the center of the transmission) to rotate slowly as the the planets rotate around the transmission. That rotation of the sun

gear is used as the output of the system. The difference in rotational speed between the planet wheel carrier (high speed) and the sun gear (low speed) is the gear ratio of the transmission. This gear ratio can be altered by changing the diameter of the components within the system. The torque of the system in standard planetary drives is transferred through the gear teeth which mesh with each other. An overview of the working principle of planetary drives and how they compare to the Archimedes drive is shown in figure 2.6.

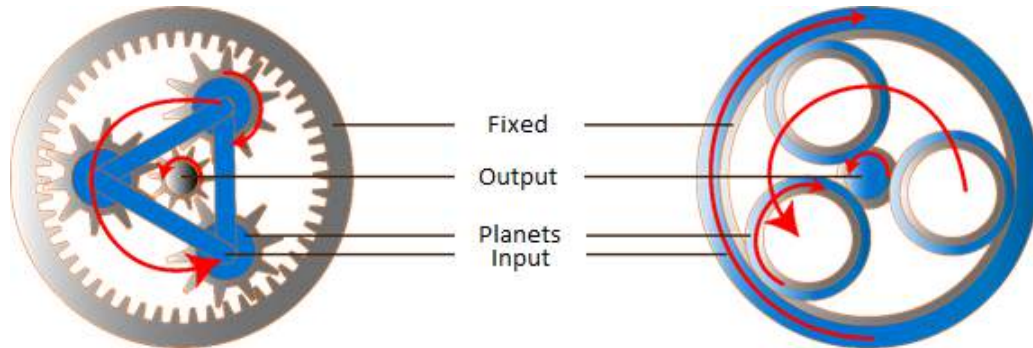


Figure 2.6: Working principle of standard planetary transmission (left) compared to the novel transmission in the DOT wind turbine (right)

Figure 2.6 shows that both systems use the planetary transmission principle, however the way these two systems transfer torque is different. The way the Archimedes drive transfers torque is explained by the second working principle (friction transmission). Standard planetary drives rely on teeth to transfer torque from one gear to the other, the Archimedes drive transfer that same torque using the friction of surfaces rolling over each other. In order for the transmission to transfer torque there must be sufficient frictional contact between the surfaces of the planets, sun wheels and annuli. Insuring sufficient frictional contact is done by generating the required amount of normal force on the rolling surface. To generate that force, slightly over-sized hollow planet wheels (named flex-roller) are compressed into an oval shape and inserted into the gearbox. When inserted, those flex-rollers, which have been elastically deformed, would want to naturally expand back to their original shape, acting like springs. This elastic expansion will generate the contact force required in order to allow the transfer of torque. The system in the DOT wind turbine will primarily be using steel, meaning that the force that can be transmitted at the contact surfaces is the friction coefficient of steel multiplied by the force used to press the rollers onto the inner wheels and annuli. The high Young's modulus of steel will only result in a small total flex-roller deformation in order to meet the required contact forces.

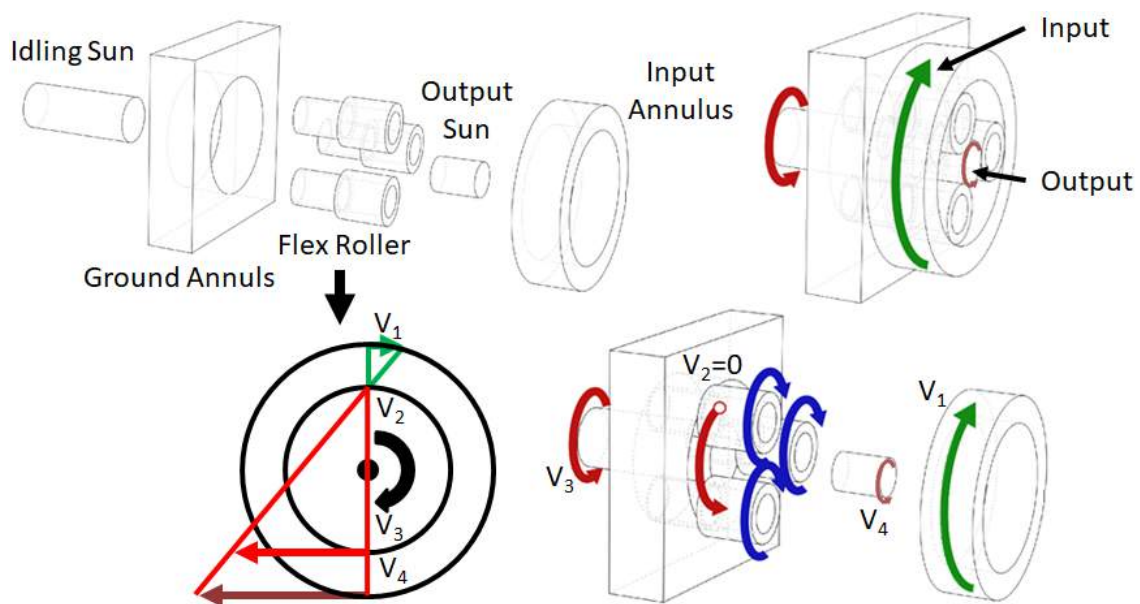


Figure 2.7: Exploded view (top left), input and output locations (top right), flex-roller velocities (bottom left) and component movement directions (bottom right) of the Archimedes drive [9]

Since the Archimedes drive has hollow flex-rollers that deform, no connecting carrier can be used for the planets, meaning that the input cannot be fixated. Using the third working principle (compound transmissions), the Archimedes drive would have an input to the system. The compound principle for the transmission is explained using figure 2.7. Looking at the figure, the input annulus is used as input and will drive the planet wheels. These planet wheels roll over the surface of a fixed ground annulus. Each planet (flex-roller) have two sections with different diameters, the first half makes contact with the input annulus and the output sun wheel and the second half will stick out from the input annulus to make contact with the ground annulus and idling sun wheel. The flex-roller is made to roll around the contact with the ground annulus, making the instantaneous velocity at that location zero. The resulting velocities at all the other contact points are shown in the bottom left of figure 2.7. The difference in the input velocity ( $V_1$ ) and the output velocity ( $V_4$ ) is the final gear ratio of the system. Changing the diameter between the two sections of the flex-rollers also affects the final gear ratio. The smaller the difference in diameter between the two sections, the higher the gear ratio becomes. The relation to calculate the gear ratio is shown in equation 2.1.

$$GR = \frac{D_{outer-annulus}}{D_{input-sun}} * \frac{D_{flex-roller} + step}{step} \quad (2.1)$$

The variables for relation 2.1 are, the diameter of the outer annullus ( $D_{outerannulus}$ ), the diameter of the input sun ( $D_{inputsun}$ ), the diameter of the smaller side of the flex-roller ( $D_{flex-roller}$ ) and the step size ( $step$ ). Equation 2.1 shows that as the step size decreases the gear ratio increases. The limit of the gear ratio is influenced by production tolerances related to this diameter step size.

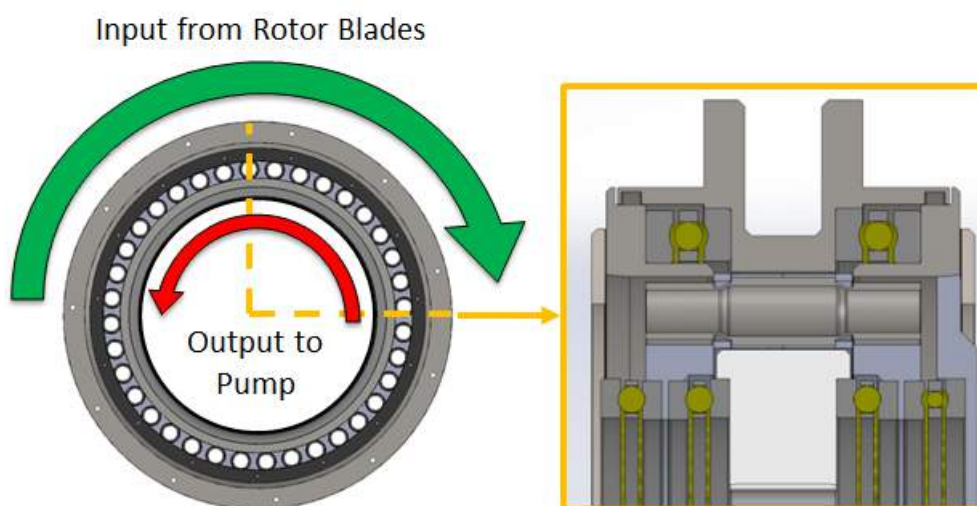


Figure 2.8: Side (left) and cross-sectional cut-out (right) of the DOT transmission with the input and output location indicated [8]

The working principle of the DOT transmission, shown in figure 2.8, is identical to the one shown in figure 2.7, however there are some geometrical differences. Firstly, the diameter of the sun wheel in the DOT systems is much larger and hollow. This was done so that the water pump can be placed inside the transmission. Secondly, the DOT transmission uses 36 flex-rollers instead of three, allowing the system to be able to handle more torque. Thirdly, in the wind turbine application, the flex-rollers are mirrored on the edge with the larger diameter, this was done to greatly reduce the turning moment the planet experiences during operation. The mirroring of the planets can be seen in symmetric drive shown in figure 2.9. In this figure all the major components are labeled and the legend is situated above the two cross-sections. On the left is a cross-sectional view of the transmission shown in figure 2.7 and on the right is the transmission used in the DOT system. As can be seen in figure 2.9, the flex-rollers, indicated by the number 3, are mirrored in the symmetric drive, this allows the transmission to be moment neutral, decreasing the wear of the system. Lastly, to keep the components from moving in axial direction, a cage (also known as a carrier) for the planet wheels was added in the system.

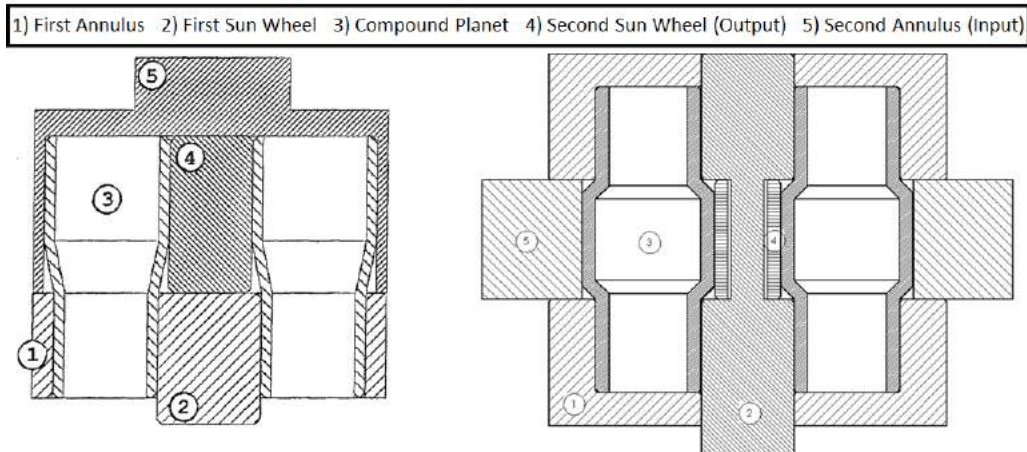


Figure 2.9: Illustration of an asymmetric (left) & symmetric (right) Archimedes drive with all core components labeled [9]

Overall, this new gearbox is fundamentally different compared to current systems on the market, therefore traditional heat generation relations used for wind turbine transmissions cannot be used. The complete overview of the gearbox used in the DOT drive with all components labeled is shown in figure 2.10. In addition to the previously mentioned components, there are six bearings separating the different rotating elements from each other. Each rotating element and the six bearings generate heat in the system. A more in-depth overview of heating in the drive-train can be seen in section 2.4.

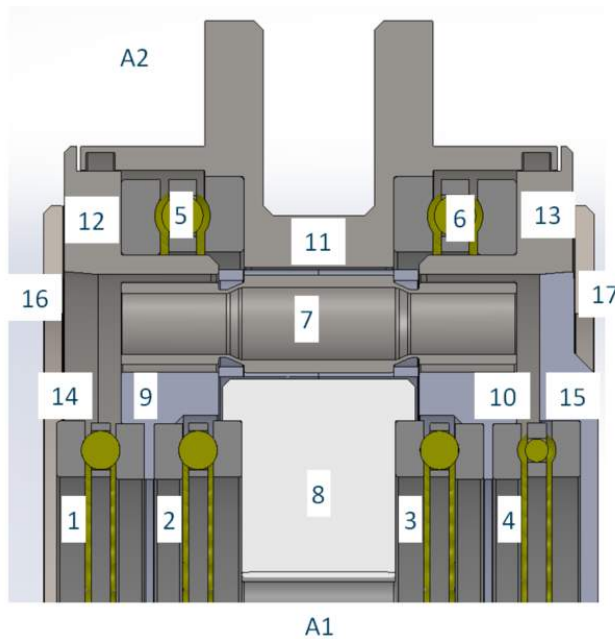


Table 2.1: The name and numbering of the components in the DOT transmission

Part Name	Part Number
1, 4	Idling Sun Wheel Bearing
2, 3	Output Sun Wheel Bearing
5, 6	Input Annulus Bearing
7	Flex-Roller
8	Output Sun Wheel
9, 10	Idling Sun Wheel
11	Input Annulus
12, 13	Ground Annulus
14, 15, 16, 17	Housing

Figure 2.10: Overview of all components in DOT transmission[8]

## 2.4. Drive-Train Heating

Most of the heating from traditional wind turbines come from two sources; the gearbox and the generator. The efficiency loss, which is responsible for the heat generation is caused by mechanical losses in the transmission and conduction losses in the generator.[10] Both of these losses need to be minimized in order to decrease the heat build-up in the system. The DOT concept will not use a generator, therefore that contribution will not need to be taken into consideration. This results in the transmission being the largest source of heat.

The transmission generates heat because of the mechanical losses. This loss can be split into two categories; load dependent and load independent losses.[10] An overview of those losses can be found below:

- Load dependent losses
  - Friction generated by gear teeth sliding
  - Bearing rolling contact losses
- Load independent losses
  - Friction losses between the transmission fluid and rotating elements
  - Friction losses between the transmission fluid and stationary elements

As shown above, the load dependent losses are mainly caused by two things. These are the friction generated by the sliding of the gear teeth over each other and the rolling contact losses of the bearing elements inside of the transmission. The load independent losses or churning losses, are the viscous friction losses between the transmission fluid and the mechanical elements which are submerged in that fluid. The transmission fluid plays a vital role in the durability of the gearbox because it decreases the friction between the gear teeth and it can be used to remove heat from the system.

In the DOT system the heat generation would be different from that in a traditional planetary transmission. The Archimedes drive concept does not use any gear teeth, this removes the heat generation caused by the teeth sliding over each other. However, the Archimedes drive will have a large amount of rolling components in traction based contact, increasing the generated heat from rolling elements. This system can therefore be theoretically seen as being built up of multiple bearings. This means that the rolling friction contribution to the load dependent losses will increase to compensate for removal of gear teeth. Lubrication will also be different in the DOT concept because all components will be rolling over each other rather than sliding. Therefore the lubrication thermal properties would resemble that of multiple bearings in a single system. The Archimedes drive relies on frictional contact to transmit torque meaning that if lubrication needs to be used, the amount of normal force applied by the flex-rollers would have to increase to compensate for the reduction in static and dynamic friction coefficient. It is yet unknown how lubrication affects the temperature in the DOT transmission. Creating the thermal model would make it possible to determine what lubrication is desirable.

# 3

## Research Objective

It is still unknown how much heat the DOT system will generate. This is because it uses a novel transmission which has never been used in wind turbine conditions. It is therefore important to have a thermal understanding of the complete system. Therefore a general thermodynamic model is created to determine and predict the heat properties of this novel transmission. Based on that model, future transmissions can be designed taking the heat generation into consideration at an early stage in development.

This model makes it possible to calculate the heat of the complete system during the preliminary design process. With current available software it is not possible to calculate the heat generation and final steady-state temperature distribution of this specific system until the design is close to completion. Additionally, to calculate the final temperature of the system an iterative process needs to be used. In order to determine the final temperature, the amount of convection and radiation present in the system needs to be known. To determine this, the temperature of the system is required. This results in an iterative loop where an initial temperature is given and based on that value all other unknown variables are solved. Those variables are then used as input to determine the new temperature. In each iterative step the value of the temperature inserted in the model is checked with the one calculated by the model to determine if they are the same. Multiple iterations are required before the final steady-state heat-map can be determined. Using current programs, based on the mesh size and computational power, it takes 5-10 minutes to solve one iteration, having multiple iterations would drastically increase the computational time. Additionally, they only calculate the temperature once the input power and all geometric related thermal coefficients are known. The model created in this thesis will make it possible to calculate the final temperature of the transmission based only on initial sizing and the desired operation conditions. This would allow for fast and accurate preliminary design thermodynamic calculations which can be used in the design process. The process of creating this model can be summed up by the following research objective:

**The research objective is to develop a general thermal model for a novel compound planetary traction transmission used in a wind turbine by implementing heat transfer relations in combination with non-linear numerical analysis and validating the results with a scaled prototype.**

The research objective can be broken down into multiple research questions. These research questions will be further analyzed in this thesis in order to be able to generate the thermodynamic model. The research questions are as follows:

1. Which components generate heat and how can they be numerically modeled?
  - (a) What is the number of components in the system?
  - (b) How many of those components generate heat?
  - (c) What relations can be used to model the heat generation?
  - (d) What assumptions need to be made for the relations?
2. Which derivation of the heat transfer equations need to be used?

- (a) Is there conduction, convection and radiation present in the system?
  - (b) Which forms of heat transfer are dominant?
  - (c) How can the standard heat transfer relations be applied to this situation?
3. Which solving method can be used to find the temperature during the drive's operation?
- (a) Can the system be solved linearly or non-linearly?
  - (b) How many dimensions does the solver need to be?
  - (c) What is the accuracy of the model?
4. How can the thermal model be verified and validated?
- (a) Is there a relation between the results of the thermal model and a third party software?
  - (b) Can the prototype be scaled?
  - (c) How can the thermal data be gathered from the test procedure?
  - (d) Is there a relation between the results of the thermal model and the validation test?

Answering these research questions will make it possible to create the desired thermodynamic model. The research questions can be split into three separate groups; these are those related to thermodynamics, modeling and verification and validating. Once these research questions are answered a prediction of the steady-state temperature of the DOT transmission can be made.

# 4

## Theory of the Thermal Model

The thermodynamic model can be split into two categories. The first category is the theory related to modeling the heat generation and the second is the theory related to heat dissipation. Using both of these theories a complete thermal understanding can be made for this novel transmission. The heat generation is explained in section 4.1 and the heat dissipation model is explained in section 4.2.

### 4.1. Heat Generation

In the DOT transmission system there are different types of bearings, each heating up differently depending on the load and rotational speed it experiences. These bearings can be categorized into two groups, these are ball bearings and roller bearings. The flex-rollers used to generate the gear ratio can also be seen as bearings, therefore their heat generation resembles that of a bearing, for more information see section 4.1.3. Many variables contribute to heat generation in a bearing, the dominant variables are given below:[11]

- Bearing load
- Bearing speed
- Bearing friction torque
- Lubrication type and viscosity
- Bearing housing design
- Environment of operation

The heat generated by roller bearings is caused by the factors which resist the rotation. Those factors are the rolling, sliding and lubrication frictions.[16] Rolling friction occurs when the rolling elements roll over the raceway. Sliding friction occurs in the cage, roller and raceway at the guiding surfaces and lips. Lubricating friction results from the lubrication's internal properties at the contact surfaces as well as churning and working action.[16]. A brief explanation on the three main forms of heat generation in bearings is given in section 4.1.1 and the empirical relations are given in section 4.1.2.

#### 4.1.1. Main Forms of Heat Generation

As stated previously heat generation in bearings is mainly caused by rolling, sliding and lubrication friction. These three types of friction are explained in this section. If there is no pure rolling contact between two surfaces, sliding will occur which will contribute to rolling friction. To have pure rolling contact the following conditions must be met: [11]

1. Mathematical line contact under zero load
2. Line contact in which the contacting bodies are identical in length
3. Mathematical point contact under zero load

Rolling friction is a complex phenomenon between the rolling elements and the raceway. It is composed partly out of elastic hysteresis and partly out of associated sliding resistance.[16]. The cause of rolling resistance is visualized in figure 4.1.

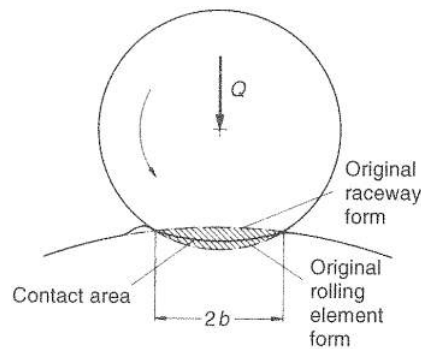


Figure 4.1: Deformation of a roller and the raceway, indicating rolling contact area and hysteresis[16]

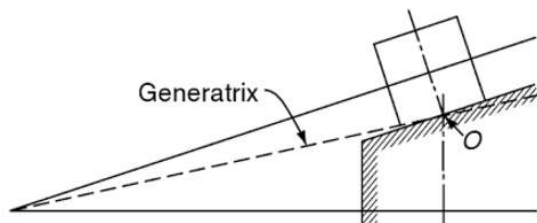


Figure 4.2: Roller-raceway contact with generatrix of motion[11]

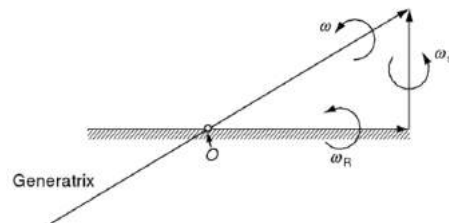


Figure 4.3: Sliding velocities about the point of pure rolling[11]

Figure 4.1 illustrates the contact between a rotating rolling element and its raceway. It can be seen that both bodies are deformed over the width of the contact area  $2b$ . At this contact location the raceway is stretched and the roller is depressed. Those deformations cause sliding during the rolling motion, which produces friction.[16] Having a groove in the raceway, like a deep-groove ball bearing, also increases the roller friction.[16] This is because the surface velocity of the ball varies along the contact surface with the raceway, only allowing for pure rolling contact at finite points within the contact area. At the locations where no pure rolling is present there will be slip, generating heat. The larger the curvature of the groove the larger the slip.[16] Additional slip in a bearing can be visualized by showing its rotation about the generatrix of motion.[11] Figure 4.2 shows a "straight-line" contact surface between a roller and the race-way, the generatrix of motion only intersects the surface at one location. Only at that location pure rolling is present.[11] The rest of the contact area can be illustrated as shown in figure 4.3. The angular velocity ( $\omega$ ) is split into its rolling motion ( $\omega_R$ ) and spinning motion ( $\omega_S$ ) components. The further the distance away from where the generatrix of motion crosses the contact surface the greater the sliding.[11] An illustration of this phenomenon can be seen in figure 4.4. In this figure the sliding lines and the point of pure rolling are shown.

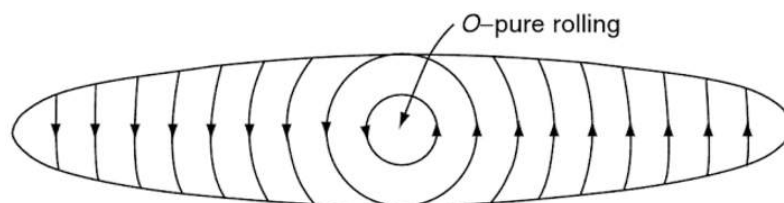


Figure 4.4: Contact ellipse showing point of pure rolling and sliding lines [11]

The heat generation from sliding is generated on the contact ellipse of the balls or rollers shown in figure 4.4. The rolling element has a different sliding velocity and experiences different friction along the contact area due to the varying geometry. The summation of those sliding friction lines on the contact ellipse results

in the total heat generated by sliding.[11] Another factor which generates rolling friction is the hysteresis of the material. When the rolling element is rolling over the raceway, the material of the raceway in front of the roller is deformed. This is visualized in figure 4.1 on the contact surface left of the rolling element. The energy required for this deformation is partly covered by the relief deformation behind the roller which aids the rolling movement, the rest is converted into heat.[16] These forms of sliding caused by rolling are all categorized into rolling friction.

Sliding friction is caused by the sliding motion of the rolling surfaces over the guiding surfaces in the cage (also referred to as carrier) or raceway.[16] If a cage is not present in a bearing the sliding friction is generated by adjacent rollers slipping over each other. Additionally, if a lip is used in the bearing's design, the heat generated by the slipping on that contact surface needs to be taken into consideration.[16] The total force causing the sliding friction is dependent on the weight of the cage, the displacement of the center of gravity from the cage pocket clearance and the acceleration and deceleration that the rolling elements exert on the cage.[16] During normal operating conditions under a normal load with good lubrication, the sliding friction should be minimal. Despite this, the sliding friction could increase if poor lubrication is used, contamination is present or operating speeds increase.[16] Therefore, the amount of sliding friction in a bearing system changes with different bearing internal layout and operating conditions.

The final main form of heat is generated by lubrication friction. This friction is caused by the internal frictional properties of the lubricant between the working surfaces, the churning of the lubricant and the working action that occurs with a large amount of lubricant at high speeds.[16] The geometry can affect the amount of lubrication friction inside of a bearing, some of the geometric features are given below:[16]

- Rolling element size
- Shape of the ring lip and cage
- Width of the guiding gap between the cage and ring lip
- Presence of free passages from one side of the bearing to the other

The viscosity of the oil and the amount of lubrication used in the bearing also plays a large roll in the lubrication friction. The higher the viscosity and the more oil used, the higher the lubrication friction value. If a large amount of oil is pumped through the system to dissipate the heat, it could have a detrimental effect on the temperature. This is because the bearing's cavities could be completely filled with oil forcing the lubrication to be additionally worked by the cage and rolling elements, increasing the friction.[16] Bearing grease, due to its higher viscosity, may not completely fill the bearing's cavity. To ensure this does not happen, excess grease would need to be expelled from the side of the rolling elements. Increasing the rotational speed also increases the lubrication friction in the system. Overall, the total lubrication friction in a bearing is dependent on multiple factors which could change the total amount of friction greatly. Many factors determine the total heat generation of a bearing, making it difficult to analytically determine it, therefore empirical relations were created which can be used to predict the heat power across a wide range of bearings.[16]

#### 4.1.2. Empirical Relations

A multitude of variables are required to calculate the heat generation of a bearing. These variables can be categorized into the three friction categories responsible for the heat generation explained in section 4.1.1. Due to the large amount of unknowns, empirical methods were developed to effectively calculate the temperature based on previously tested and well-known systems. Those empirical relations can be used to solve the thermodynamic properties of standard bearings.[17] The DOT system uses six thrust ball bearings. The heat these bearings generate can be calculated using this method. Additionally, with some modifications, the flex-roller's heat generation can also be calculated using this method. The applicable equations used to calculate the total heat generating power are shown in this section. The total heat power generated by the system for low speed bearings can be defined by the equation shown in relation 4.1. High speed bearings have to include the heat generated from high speed sliding friction. This value is added to the value calculated in equation 4.1. Since the bearings used in this transmission system are not considered high-speed bearings, this aspect can be neglected.[11]

$$H_f = 1.047 * 10^{-4} * nM \quad (4.1)$$

In this equation ( $n$ ) represents the rotational velocity in rpm and ( $M$ ) represents the friction moment in Nmm. The friction moment is the resistance that the bearing exerts against its movement. This is a function of the total friction in a bearing, which is the sum of the rolling, sliding and lubricant friction explained in section 4.1.1. The relation to determine that friction moment is given in equation 4.2.[16]

$$M = \mu_B F d / 2 \quad (4.2)$$

In which ( $\mu_B$ ) is the rolling friction coefficient of the bearing, ( $F$ ) is the resultant bearing load in N and ( $d$ ) is the bearing bore diameter in mm. The coefficient of friction is dependent on many factors, some of which are; the bearing type and size, the lubrication condition, the load and the rotational velocity. If no lubrication is used in the system or the bearing is operating under unfavorable conditions (high load or low velocity) the rolling element makes direct contact with the race-way causing an increase in the friction moment as ( $\mu_B$ ) increases. In this condition the frictional moment is difficult to quantify and will need to be determined by a test procedure.[16] Once lubrication is used and the bearing operates under favorable conditions a lubrication film is formed in between the rolling element and the raceway. The friction moment of this normal operating condition can be calculated using relation 4.3.[11]

$$M = M_1 + M_v + M_f \quad (4.3)$$

The friction moment can be split into three categories. These are the torque due to the applied load ( $M_1$ ), the viscous friction torque ( $M_v$ ) and the torque due to an additional applied thrust load ( $M_f$ ). The rolling and sliding friction are responsible for the torque due to an applied load ( $M_1$ ) and the lubricant friction is responsible for the viscous friction torque ( $M_v$ ). If a bearing is only loaded in a single direction the torque due to an additional applied thrust load ( $M_f$ ) does not need to be added to the equation [11]. The equation for the torque due to an applied load is shown in equation 4.4.[17]

$$M_1 = f_1 F_B d_m \quad (4.4)$$

In equation 4.4 the inputs are, ( $f_1$ ) which stands for the torque due to a applied load factor, ( $F_B$ ) which is the radial or axial force (depending on the bearing) and ( $d_m$ ) is the mean diameter of the bearing in mm. To determine the load factor equation 4.5 is used for ball bearings, and for roller bearings the chart in figure A.4 of the appendix is used.[17]

$$f_1 = z(F_s / C_s)^y \quad (4.5)$$

In equation 4.5 the variable ( $F_s$ ) stands for the static equivalent load and the variable ( $C_s$ ) is the basic static load. Inputs ( $z$ ) and ( $y$ ) can be found in figure A.3 in appendix A and are dependent on the type of bearing. To determine ( $F_s$ ) equation 4.6 is used for radial bearings and equation 4.7 is used for thrust bearings.[11] The value for ( $C_s$ ) varies with each bearing and is given by the supplier.

$$F_s = X_s F_r + Y_s F_a \quad (4.6)$$

$$F_{sa} = F_a + 2.3 F_r \tan(\alpha) \quad (4.7)$$

In the above mentioned equations ( $F_r$ ) and ( $F_a$ ) stand for the radial and axial force respectively. The values for ( $X_s$ ) and ( $Y_s$ ) can be acquired from the data table given in figure A.5 in appendix A, they are dependent on ( $\alpha$ ) which is the contact angle of the bearing.

The viscous friction torque ( $M_v$ ) relation depends on the rotational velocity of the bearing, the two relations are shown in equations 4.8 and 4.9.[17]

$$M_v = 10^{-7} f_o (v_o n)^{2/3} d_m^3 \quad v_o n \geq 2000 \text{ cSt/min} \quad (4.8)$$

$$M_v = 160 * 10^{-7} f_o d_m^3 \quad v_o n \leq 2000 \text{ cSt/min} \quad (4.9)$$

Relations 4.8 and 4.9 use the bearing lubrication factor ( $f_o$ ), the kinematic viscosity ( $v_o$ ) in centistokes, the rotation velocity ( $n$ ) given in rpm and the pitch diameter ( $d_m$ ) in mm as inputs. Values for ( $f_o$ ) can be found in figure A.1 in appendix A, the other inputs are given by the design requirements and the manufacturer.

The equation to determine ( $M_f$ ) is given in relation 4.10.[17]

$$M_f = f_f F_a d_m \quad (4.10)$$

All inputs for equation 4.10 besides ( $f_f$ ) have been mentioned previously. The values for ( $f_f$ ) can be found in figure A.2 of the appendix. All variables can now be determined to calculate the friction moment and the heat that a bearing generates.

For the factors taken from the tables in appendix A, a range of possible values can be chosen. This range is dependent on the series number of the bearing. Looking at a standard bearing, a series number is given by the first two numbers in their bearing code.[16] For example, a bearing with code 'NU2314' has a series number of '23', with the number '2' describing the width series and '3' describing the diameter series. The prefix in the bearing code 'NU' stands for the type of bearing, in this case, a cylindrical roller bearing with two guiding lips on the outer surface. Lastly, the remaining number '14' stands for the bore number, the higher the number the larger the internal diameter of the bearing.[16] Each bore number has a standardized series number that sets the diameter and width of the bearing, an illustration of this is given in section 4.5.

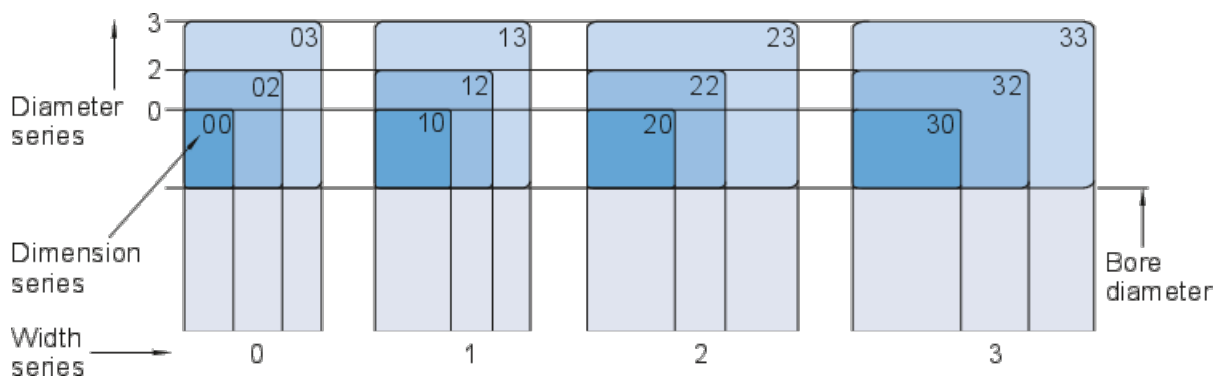


Figure 4.5: Illustration showing the change in diameter and width for a given bore number as a result of the bearing series [54]

The width series are numbered 8, 0, 1, 2, 3, 4, 5 and 6, with the 8 series having the smallest width and the 6 series the largest. The diameter series, ordered in increasing diameter are 7, 8, 9, 0, 1, 2, 3 and 4 .[54] This indicates that a bearing with a series number of 64 has the largest width and diameter for a given bore diameter. As shown in figure 4.5, if the width series number (indicates by the number '2' in the example) changes, only the bearing width is altered. However, if the diameter series number (indicates by the number '3' in the example) changes, the diameter and width of the bearing is altered.[54] The factors given in the charts in the appendix are largely determined by the width of the bearing,[16] therefore both numbers in the bearing series must be taken into consideration. Taking this into account, it is assumed that the factors change linearly as the bearing diameter and width series increases. The factors in the appendix will therefore be determined by looking at the diameter and width series individually, then determining how the factor changes as the series increases. Using this, a factor will be calculated for the two series and the highest value will be taken in the model.

Using the example 'NU2314' (cylindrical roller bearing with width series 2 and diameter series 3) the resulting value for ( $f_1$ ), as shown in figure A.4, can vary between 0.0002 and 0.0004 depending on the series number. It is assumed that the change in ( $f_1$ ) is linear across the different series. The next step is to calculate ( $f_1$ ) for both the width and diameter series separately, assuming a linear increase in ( $f_1$ ) as the series number increases. The resulting ( $f_1$ ) factor when only looking at the width series is 0.00029 and when only looking at the diameter series is 0.00037. The largest value of 0.00037 will then be taken as the ( $f_1$ ) factor for the model. This method is a rough approximation and will need to be validated with numerous test to determine if it is accurate enough. However, this extensive validation is beyond the scope of this thesis. Therefore if there is still an uncertainty within the range of possible factor values given, the model would take the value which results in the highest heat generation, making the model conservative.

#### 4.1.3. Flex-Roller Heat Generation

Additional steps are required in combination with the equations shown in section 4.1.2 to calculate the heat generation caused by the flex-rollers. In order to calculate this, the flex-roller's working principle must first be

explained. The flex-roller used in the wind turbine is shown in figure 4.6. This figure shows the flex-roller from the front and side view. The side view has been simplified to only show the change in diameter between the two sections. As indicated in the figure, the flex-roller is split between an outer and inner section. The inner section is located in the middle of the flex-roller and has the largest diameter, the outer sections located on both ends of the flex-roller have identical diameters which are less than the inner section. Each section is a hollow cylinder with a specified wall thickness and length. These dimensions are determined by how much tangential force the flex-roller needs to generate once compressed and inserted within the annuli. This working principle is explained further in section 2.3. To calculate this tangential force the relation in equation 4.11 is used.

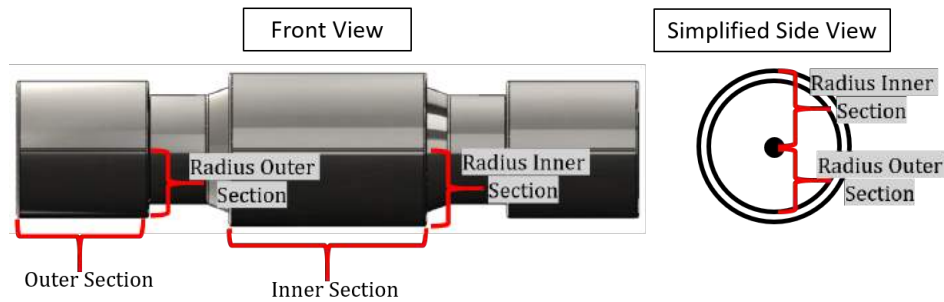


Figure 4.6: The front and simplified side view of a flex-roller indicating the radii of the different sections

$$F_t = \frac{M}{Z R_{in} \mu_s} \quad (4.11)$$

In which ( $M$ ) is the required input torque/moment, ( $Z$ ) is the number of flex-rollers, ( $R_{in}$ ) is the radius of the contact point between input annulus/sun and the flex-roller and ( $\mu_s$ ) is the static friction coefficient of the material used. This tangential force ( $F_t$ ) is applied by each section of each flex-roller around the circumference of the drive. Since there is a variation in diameter between the two sections, the wall thickness and length are different to ensure the same tangential contact force throughout the three sections. Additionally, the three sections each make contact with a different set of annuli, resulting in them independently acting like three separate roller bearings. Each section has a different diameter. The difference in this diameter is largely responsible for the gear ratio in the system. This effect is illustrated in figure 4.7.

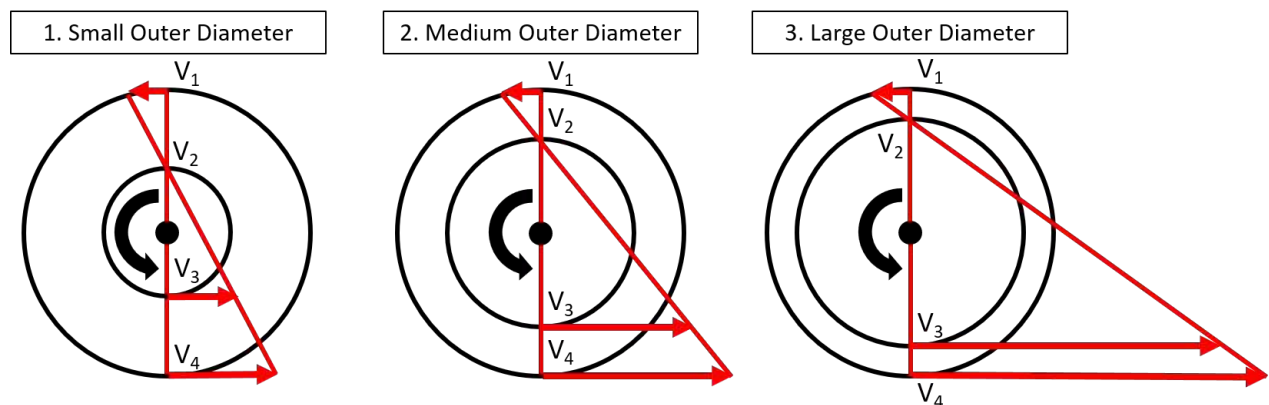


Figure 4.7: The effect of three different flex-roller geometries on the velocity profile, the closer the diameter of the two sections become the greater the velocity gradient

Figure 4.7 illustrates three different flex-rollers with slightly different geometries. The diameter of the inner section remains the same for all three cases while the diameter of the outer sections change from small, medium to large. Each case shows four different velocities; the input annulus contact velocity ( $V_1$ ); the ground annulus contact velocity ( $V_2$ ); the idling annulus contact velocity ( $V_3$ ); and the output annulus contact velocity ( $V_4$ ). In this illustration the input annulus contact velocity ( $V_1$ ) remains the same for all three cases and

the ground annulus contact velocity ( $V_2$ ) is zero. As can be seen in the figure, the larger the diameter of the flex-roller's outer section becomes in comparison to the inner section, the larger the idling ( $V_3$ ) and output velocities ( $V_4$ ) become. This is because the flex-rollers are forced to roll over the ground annulus, which is fixed and not rotating, resulting in the contact velocity being zero at that location. Having that contact velocity of zero makes the flex-roller, as a whole, act like a lever with that contact point on the ground annulus being the base. The closer that base is moved towards the location where the initial input is applied (increasing the diameter of the outer section), the faster the lever's output moves. However, more input force will be required to push that lever. Indicating that situation three in figure 4.7, compared to the other two situations, will result in the fastest output velocity but will require more input force to run. This shows that depending on the gear ratio requirement and the available input torque of the system, the ratio between these two diameters can be altered to meet the performance required. In theory, the system can generate an infinitely large output speed if the difference between the two sections is infinitely small and the system can generate a large enough input force.

A relation can be determined which calculates all the velocities shown in figure 4.7 based on the input velocity. The velocities in the system at a fixed moment in time can be linearly illustrated. At that fixed moment in time the diameters and two velocities ( $V_1$  and  $V_2$ ) are known. From these known variables all resulting velocities can be calculated. The relation used is shown in equation 4.12.

$$V_n = \frac{V_i(l_n)}{l_i} \quad (4.12)$$

In which ( $V_i$ ) is the input velocity, ( $l_i$ ) is the radial distant between where the input velocity is applied and the ground annulus contact location and ( $l_n$ ) is the radial distance between where the velocity needs to be determined and the ground annulus contact location. All required velocities can be calculated for the flex-roller using that equation. It is important to note that the location of the input, ground, idling and output annulus can change based on the design. For example, ( $V_3$ ) could be the input and ( $V_1$ ) could be the output making the system a speed reducer rather than speed increaser.

Using the calculated velocities the heat generated by the flex-roller system needs to be determined. The first step is to split the flex-roller in it's specified sections. As stated previously, the flex-roller is composed out of three sections, with each section acting like an independent roller bearing. The flex-roller shown in situation two in figure 4.7 was split-up to illustrate the velocities in each section. This decomposition can be seen in figure 4.8.

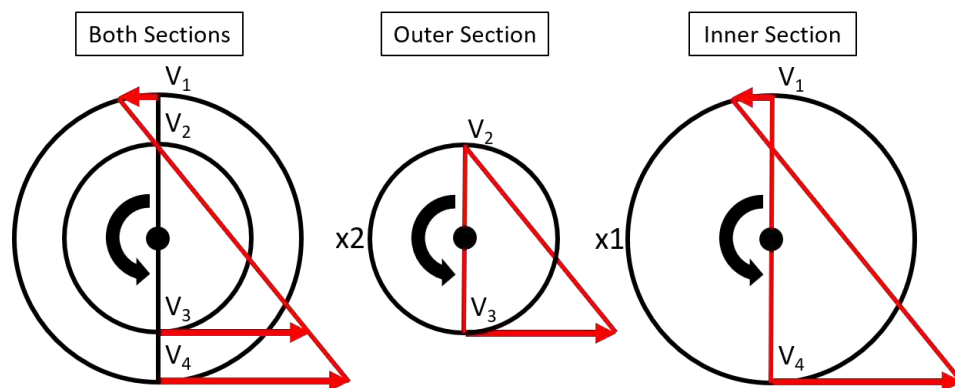


Figure 4.8: Decomposition of the velocity profile for the flex-roller, the thermal model assumes that the flex-roller is separate cylindrical roller bearings

Figure 4.8 illustrates the velocities per section of the flex-roller. As indicated in the figure there are two outer sections with velocities ( $V_2$ ) and ( $V_3$ ) and one inner section with velocities ( $V_1$ ) and ( $V_4$ ). Using these velocities three independent heat generation calculations can be made using the equations shown in section 4.1.2. The steps to calculate the heat generation resemble that of a bearing, therefore the same process as shown in section 4.1.4 can be used. The only difference is that the total heat generation of the flex-roller is the summation of the three separate sections, which are seen as three independent bearings.

#### 4.1.4. Bearing Heat Calculation

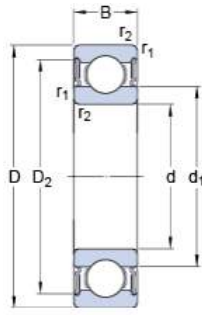


Figure 4.9: Illustration of SKF 61804 deep-groove ball bearing [18]

Table 4.1: SKF 61804 dimensions and data [18]

Description	Symbol	Value	Unit
Inner Diameter	$d$	20	mm
Outer Diameter	$D$	32	mm
Mean Diameter	$d_m$	26	mm
Width	$B$	7	mm
Rotational Velocity	$n$	620	rpm
Basic Static Load	$C_s$	2.32	kN
Fatigue Load Limit	$P_u$	0.104	kN
Nominal Contact Angle	$\alpha$	0	$^\circ$
Lubricant Viscosity	$\nu_0$	110	cSt

In order to get a good understanding of how to calculate the heat generation of the system an example calculation is made. The heat generation of a bearing within the gearing systems tested in section 6.2 will be calculated. The example bearing is a SKF 61804 deep groove ball bearing, all the relevant dimensions and input criteria are indicated in figure 4.9 and table 4.1. The heat power generated by the bearing will be calculated at the fatigue load with the operational rotational velocity of 620 rpm. To calculate the heat generated by the bearing the equations in section 4.1.2 are used.

The first step is to calculate the different friction moments in the bearing. The torque due to the applied load ( $M_1$ ) is calculated as follows:

From equation 4.6 with inputs from table 4.1 and figure A.5.

$$F_s = X_s F_r + Y_s F_a = 0.6(104) + 0.5(0) = 62.4N \quad (4.13)$$

From equation 4.5 with inputs from equation 4.13, table 4.1 and figure A.3.

$$f_1 = z(F_s/C_s)^y = 0.004(62.4/2320)^{0.55} = 0.0005475 \quad (4.14)$$

From equation 4.4 with inputs from equation 4.14 and table 4.1.

$$M_1 = f_1 F_B d_m = 0.0005475(104)26 = 1.480Nmm \quad (4.15)$$

The viscous friction torque ( $M_v$ ) is calculated next. In order to determine the correct relation the rotational velocity, in rpm, of the bearing needs to be multiplied by the viscosity of the lubricating fluid. This is done in equation 4.16.

$$\nu_0 n = 110(620) = 68200cSt/min \quad (4.16)$$

Since the value of ( $\nu_0 n$ ) is larger than 2000 relation 4.8 will be used. All the variables are known except the bearing lubrication factor ( $f_o$ ). This value depends on the type of bearing and lubrication used. The bearing is a deep groove ball bearing and grease is used as lubrication. The calculation of the viscous friction torque ( $M_v$ ) is as follows:

From equation 4.8 with inputs from table 4.1 and figure A.1.

$$M_v = 10^{-7} f_o (\nu_0 n)^{2/3} d_m^3 = 10^{-7} 0.7(110(620))^{2/3} 26^3 = 2.054Nmm \quad (4.17)$$

In this systems the torque due to an additional applied thrust load ( $M_f$ ) does not need to be calculated since there is only one load acting on the system in radial direction. Therefore, the total friction moment of the system can now be calculated.

From equation 4.3 with inputs from equations 4.15 and 4.17.

$$M = M_1 + M_v + M_f = 1.480 + 2.054 + 0 = 3.534Nmm \quad (4.18)$$

The total heat generated by the bearing can now be calculated, this is done in equation 4.1 with inputs from equations 4.18 and table 4.1.

$$H_f = 1.047 * 10^{-4} * nM = 1.047 * 10^{-4} * 620(3.534) = 0.23W \quad (4.19)$$

In this system at the given rpm and radial force the bearing generates 0.23 W of heat power. The heat power generated by this bearing is combined with the total power generation of the other bearings and flex-rollers to give the total heat power of the system. The final heat power is largely dependent on the type of bearing and lubrication used, meaning that each separate bearing in the transmission must be analyzed.

## 4.2. Heat Dissipation

In this section the theory used to determine the heat dissipation is discussed. Heat is dissipated throughout the gearing system using the three heat transfer methods shown in table 4.2.

Table 4.2: Heat transfer types present in the transmission system

Heat Transfer	Abbreviation	Application in Model
Conduction	<i>C</i>	Transfer through the metal structure and working components of the gearing
Convection	<i>V</i>	Transfer caused by the airflow over the external gearing sections
Radiation	<i>R</i>	Transfer of heat from the gearing structure to ambient environment

A nodal network will be constructed using the heat transfer relations discussed in this section. In this nodal network the heat transfer in radial and axial direction will be taken into consideration. Each type of heat transfer will have different equations used to calculate the heat flow throughout the gearing structure. These equations will be given first, once the equations are described the complete heat transfer model can be discussed. An introduction on the nodal network is given in section 4.2.1. The equations used to calculate the thermal conduction, convection and radiation are shown in sections 4.2.2, 4.2.3 and 4.2.4 respectively.

### 4.2.1. Nodal Network

Table 4.3: Heat transfer chart of all components in the DOT transmission, part numbering shown in figure 2.10

Surface	A1	A2	1	2	3	4	5	6	7	8	9	10	11	12	13	14	15	16	17
A1	-	-	V	V	V	V	-	-	-	V	V	V	-	-	-	V	V	-	-
A2	-	-	-	-	-	-	-	-	-	-	-	-	V,R						
1	V	-	H	-	-	-	-	-	-	-	C	-	-	-	-	C	-	-	-
2	V	-	-	H	-	-	-	-	-	C	C	-	-	-	-	-	-	-	-
3	V	-	-	-	H	-	-	-	-	C	-	C	-	-	-	-	-	-	-
4	V	-	-	-	-	H	-	-	-	-	-	C	-	-	-	-	C	-	-
5	-	-	-	-	-	-	H	-	-	-	-	-	C	C	-	-	-	-	-
6	-	-	-	-	-	-	-	H	-	-	-	-	C	-	C	-	-	-	-
7	-	-	-	-	-	-	-	-	H	C	C	C	C	C	C	V	V	-	-
8	V	-	-	C	C	-	-	-	C	-	C	C	-	-	-	-	-	-	-
9	V	-	C	C	-	-	-	-	C	C	-	-	-	-	-	V	-	-	-
10	V	-	-	-	C	C	-	-	C	C	-	-	-	-	-	-	V	-	-
11	-	V,R	-	-	-	-	C	C	C	-	-	-	-	C	C	-	-	-	-
12	-	V,R	-	-	-	-	C	-	C	-	-	-	C	-	-	C	-	C	-
13	-	V,R	-	-	-	-	-	C	C	-	-	-	C	-	C	-	C	-	C
14	V	V,R	C	-	-	-	-	-	V	-	V	-	-	C	-	-	-	C	-
15	V	V,R	-	-	-	C	-	-	V	-	-	V	-	-	C	-	-	-	C
16	-	V,R	-	-	-	-	-	-	-	-	-	-	-	C	-	C	-	-	-
17	-	V,R	-	-	-	-	-	-	-	-	-	-	-	-	C	-	C	-	-

Once the heat generation of the system is known, the next step is to calculate the heat transfer. This is done by looking at the interaction between the multiple components in the design. An overview of the systems and their numbering can be seen in figure 2.10 and table 4.3. Using the part numbering shown in figure 2.10 the

thermal interaction between individual components and their forms of heat transfer are indicated in table 4.3. Based on the interaction of those components the heat transfer equations can be determined. These equations will form a sequence of non-linear relations which will need to be solve simultaneously in the model, in order to achieve the desired steady-state temperature values.

In table 4.3 the lettering (C,V,R and H) stand for conduction, convection, radiation and heat generation respectively. Additionally the variables (A1 and A2) shown in figure 2.10 are for the external and internal boundary condition temperature. As can be seen from table 4.3, the transmission system has 17 components, resulting in a minimum 17 non-linear thermodynamic equations. The component's non-linear relation depends on the number and type of thermal interaction.

Because there is convection and radiation, the heat transfer relations that describe the system are non-linear. The solving method for these non-linear equations is explained further in section 5.2. Looking at the solving approach multiple options are possible. The transmission is a circular structure, meaning that the solver can consider the axial, radial and circumferential directions. Since the transmission has the same internal layout throughout its circumference it can be assumed that the temperature will be the same around the circumference at a fixed axial and radial location. This means that the cylindrical equations for heat transfer can be used, only taking the radial and axial heat transfer directions into consideration. A cut-out of the gearbox with the directions and desired solver paths is shown in figure 4.10.

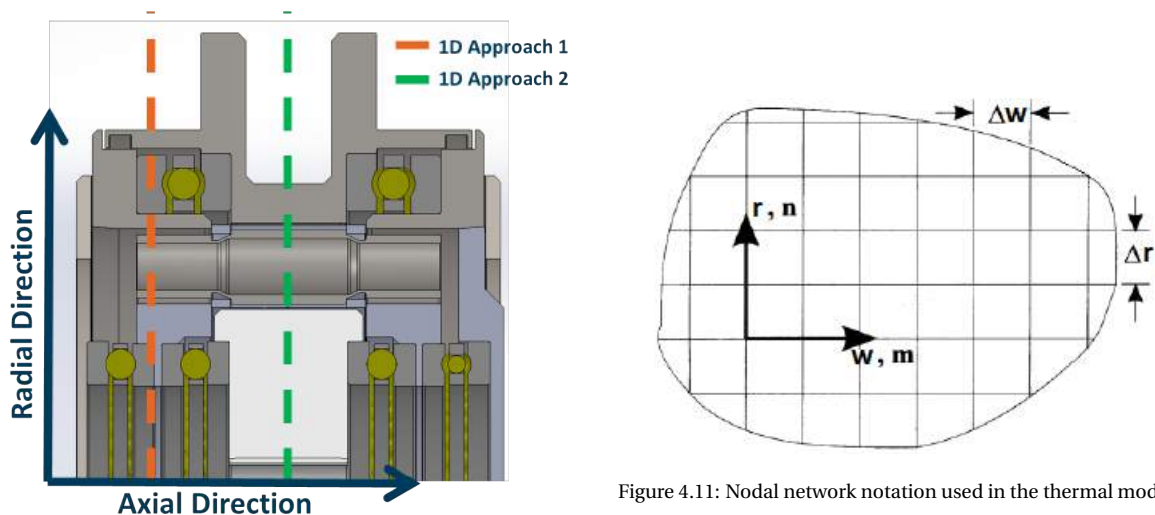


Figure 4.10: Illustration of desired solver 1D paths

Figure 4.10 shows that the model can be solved by 1D or 2D approach. The 1D approach results in only taking the interaction of components in the radial direction meaning that no axial heat transfer will be considered. The two possible 1D approaches are shown in 4.10. Approach 1 will run through the side of the transmission taking all the bearings into consideration while approach 2 runs through the center of the drive only modeling the interaction between the flex-roller, the input anullus and output anullus. The model could be further simplified, because all components are made out of steel which has high conductive properties. It can therefore be assumed that each component in the design has a homogeneous temperature. This makes it possible for the model to make two 1D calculations, one per line indicated in figure 4.10, then checking which path results in the highest temperature for that specific component. That higher temperature would then be used as the output. This model is simpler, however it will not be as accurate as taking the 2D approach.

The 2D approach will result in modeling the interaction of the components in the radial and axial direction, taking all 17 components with all the thermal interactions into consideration. This is done by creating a nodal network of the system, the basic overview of the nodal network is shown in Figure 4.11. The figure shows that a grid is created in the radial ( $r$ ) and axial ( $w$ ) direction where each node on the grid represents a temperature. Based on the location of the node with respect to its surrounding nodes the heat transfer relations discussed in sections 4.2.2 through 4.2.4 can be combined to give a complete heat-map of the transmission. Each node

has a unique equation based on its position within the drive and will be a function of the temperature of the surrounding nodes. Two main boundary conditions are used for the model; the heat power generated by the flex-rollers and the bearings and the ambient temperature and airflow conditions on the exterior of the drive. These two boundary conditions would allow the model to create a sequence of simultaneous equations which are used to calculate the steady-state temperature of each node within the system. More information on this modeling method is given in section 5.3. This approach compared to the 1D approach results in a more complex and accurate model. Since the transmission does not have the same composition throughout the axial direction the thermal model that was created was two dimensional, running in the radial and axial direction. The 2D model is then verified and validated in chapter 6 to determine its accuracy.

#### 4.2.2. Conduction

The heat dissipation throughout the structure will mainly be through conduction. In the created thermodynamic model the heat dissipation in axial and radial direction needs to be calculated. Looking at the axial direction, the general heat conduction formula, shown in equation 4.20, can be used.[12]

$$H_c = \frac{kS}{L}(T_1 - T_2) \quad (4.20)$$

In this equation ( $k$ ) is the thermal conductivity coefficient, ( $S$ ) is the surface area normal to the heat transfer, ( $L$ ) is the length of the conductive heat transfer and ( $T_1$ ) and ( $T_2$ ) are the temperatures on both sides of the conductive surface. The relation shown in 4.20 will need to be rewritten for conduction in radial direction. Since the gearing is constructed out of multiple cylindrical annuli the heat transfer relation can be rewritten to the relation shown in equation 4.21.[12]

$$H_c = \frac{2\pi kW(T_i - T_o)}{\ln(R_o/R_i)} \quad (4.21)$$

In this equation ( $k$ ) is the thermal conductivity coefficient, ( $W$ ) is the width of the annular structure, ( $T_i$ ) and ( $T_o$ ) are the inner and outer temperatures and ( $R_i$ ) and ( $R_o$ ) are the inner and outer radii respectively. Within the nodal network used to describe the thermal dissipation in the gearing each node will have an axial and radial component. This means that both equations 4.20 and 4.21 will be used for a single node.

#### 4.2.3. Convection

To calculate the convective heat transfer the general relation shown in equation 4.22 is used.[11] Using this relation the thermal convection of the housing can be determined.

$$H_v = h_v S(T_1 - T_2) \quad (4.22)$$

In which ( $h_v$ ) is the convective film coefficient of heat transfer, ( $S$ ) is the surface area normal to the heat transfer and ( $T_1$ ) and ( $T_2$ ) are the temperatures on both sides of the convective surface. The convective film coefficient is a function of the fluid and surface temperatures, the fluid's thermal conductivity, the fluid's velocity adjacent to the surface, the surface's dimensions and the fluid's density and viscosity. Depending on the flow's condition and the geometry of the convective surface the film coefficient changes. The different film coefficient relations can be categorized in two sections, these are free and forced heat convection. Free heat convection can be used for non-rotating components in contact with the external environment while forced convection is used for components which are rotating. Forced convection is also present inside of the drive, mainly in the flex-roller section. The lubrication and air pockets in the flex-roller section increase the internal heat transfer as they are forced to flow over the structure by the rotating rollers. The relations used to calculate the convective film coefficient for free and forced convection are given below. The nodal network used to create the heat-map of the transmission will incorporate both forms of convective heat transfer, section 5.1 describes how these equations are applied in the thermodynamic model.

#### Free Convection

The design is composed out of multiple cylinders of a specific diameter and thickness. This means that the drive makes contact with the ambient air with two different types of geometry. These are the a vertical wall contact on the side of the gearing and a horizontal cylinder contact around the circumference of the drive. To

calculate the film coefficient for the vertical walls, equation 4.23 is used and for the horizontal cylinder, equation 4.24 is used.[12]

$$h_v = Nu \frac{k}{L} \quad (4.23)$$

$$h_v = Nu \frac{k}{D} \quad (4.24)$$

In which ( $Nu$ ) is the Nusselt number, ( $k$ ) is the thermal conductivity, ( $L$ ) the length of the vertical plate and ( $D$ ) the diameter of the horizontal cylinder. The relation to describe the Nusselt number differs per situation. The relation for a vertical wall is shown in equation 4.25 and for the horizontal cylinder it is shown in relation 4.26.[12]

$$Nu^{1/2} = 0.825 + \frac{0.387Ra^{1/6}}{[1 + (0.492/Pr)^{9/16}]^{8/27}} \quad (4.25)$$

$$Nu^{1/2} = 0.60 + 0.387 \left( \frac{Ra}{[1 + (0.559/Pr)^{9/16}]^{16/9}} \right)^{1/6} \quad (4.26)$$

In which, ( $Ra$ ) is the Rayleigh number and ( $Pr$ ) is the Prandtl number. The Prandtl number can be calculated with relation 4.27.[12]

$$Pr = \frac{\nu_o}{a} = \frac{Cp\mu_o}{k} \quad (4.27)$$

In which ( $\nu_o$ ) is the kinematic viscosity ( $a$ ) is the thermal diffusivity, ( $Cp$ ) is the specific heat at constant pressure and ( $\mu_o$ ) is dynamic viscosity. The Prandtl number changes depending on the temperature, therefore data sheets sorted by film temperature for a specific fluid/gas are mainly used to find the Prandtl number. Looking back at equations 4.25 and 4.26, the Rayleigh number is calculated with equation 4.28. Rayleigh number is a function of the Grashof and Prandtl number. To calculate the Grashof number, equation 4.29 is used.[12]

$$Ra = GrPr \quad (4.28)$$

$$Gr = \frac{g\beta(T_w - T_\infty)x^3}{\nu_o^2} \quad (4.29)$$

In which ( $g$ ) is the gravitational acceleration, ( $\beta$ ) is the volume coefficient of expansion, ( $T_w$ ) and ( $T_\infty$ ) are the wall and ambient temperatures, ( $x$ ) is the length of the wall (for convection over a cylinder the diameter is used) and ( $\nu_o$ ) is the kinematic viscosity of the air. As can be seen the film coefficient is function of multiple variables which alter with the temperature of the fluid/gas that is in contact with the surface. Simplified relations of the ones shown above can be made for air at atmospheric pressure with moderate temperatures, these are shown in equation 4.30 for a vertical wall and equation 4.31 for a horizontal cylinder.[12]

$$h_v = 1.42 \left( \frac{\Delta T}{L} \right)^{1/4} \quad (4.30)$$

$$h_v = 1.32 \left( \frac{\Delta T}{L} \right)^{1/4} \quad (4.31)$$

If the free convection coefficient of a finite circular cylinder needs to be determined more accurately, a more comprehensive equations can be used. This relation is shown in equation 4.32.[13]

$$Nu_D = S_D + F(Pr)G_D Ra_D^{1/4} \quad (4.32)$$

The variables for equation 4.32 which have not been previously defined are ( $S_D$ ) the shape factor, ( $F(Pr)$ ) the Prandtl number function and ( $G_D$ ) the body gravity function. The equations to calculate these variables are shown in relations 4.33, 4.34 and 4.35 respectively.[14][15][13]

$$S_D = \frac{2.547 + 2.212(L/D)^{0.76}}{1 + 2(L/D)} \quad (4.33)$$

$$F(Pr) = \frac{0.670}{[1 + (0.5/Pr)^{9/16}]^{4/9}} \quad (4.34)$$

$$G_D = 0.78 \frac{2/3 + L/D}{1/2 + L/D} \quad (4.35)$$

In which  $(L/D)$  is the length over diameter ratio of the cylinder. In the thermodynamic model the cylindrical equations shown in relation 4.32 were used to calculate the Nusselt number for free convection. The resulting value was then verified with the other calculation methods discussed in this section.

### Forced Convection

At specific locations in the model forced convection is used as a mode of thermal heat transfer. These locations include the exterior of the drive, the spacing between the components and the location in the drive where the flex-rollers are located. The general heat convection formula is the same as the one shown in relation 4.22. However, the convective film coefficient is different and is depended on the condition of the flow. The forced flow can either be laminar or turbulent, this is determined by the Reynolds number, to calculate the Reynolds number equation 4.36 is used.[12]

$$Re_L = \frac{\rho u_m L}{\mu_o} = \frac{u_m L}{\nu_o} \quad (4.36)$$

In which,  $(\rho)$  is the density,  $(u_m)$  is the velocity of the flow,  $(L)$  is the length of the surface (for a cylinder the diameter is used) and  $(\mu_o)$  is dynamic viscosity. For a flat plate, if the convective fluid's Reynolds number is lower than  $5 \times 10^5$  laminar flow is assumed, if it is above, turbulent flow is assumed. Using this, the average Nusselt number of the convective flow over a flat plate can be calculated for that situation. The Nusselt number for laminar and turbulent flow are shown in equations 4.37 and 4.38 respectively.[12]

$$Nu_L = 0.664 Re_L^{1/2} Pr^{1/3} \quad (4.37)$$

$$Nu_L = Pr^{1/3} (0.037 Re_L^{0.8} - 871) \quad (4.38)$$

The Nusselt number is a function of the Reynolds number ( $Re$ ) and the Prandtl number ( $Pr$ ). The Prandtl number is determined in the same way as in free convection, shown in equation 4.27. Once the Nusselt number is calculated using the Reynold and Prandtl number the convective film coefficient can be determined. This is done using equation 4.39.[12]

$$h_v = \frac{Nu k}{L} \quad (4.39)$$

The resulting convective film coefficient can now be used to determine the total forced convective heat transfer in the transmission's thermal model. A further explanation on how these equations will be applied in model can be seen in section 5.1.

### 4.2.4. Radiation

The general relation for thermal radiation of the housing's external surface to the surrounding structures is shown in relation 4.40.[26]

$$H_r = h_r S (T - T_a) \quad (4.40)$$

In which,  $(h_r)$  is the pseudofilm coefficient of radiation,  $(S)$  is the surface area and  $(T)$  is the temperature. The pseudofilm coefficient of radiation can be calculated using equation 4.41.[11]

$$h_r = 5.73 * 10^{-8} \epsilon (T + T_a) (T^2 + T_a^2) \quad (4.41)$$

The remaining variable  $(\epsilon)$  is the thermal emissivity. Equations 4.40 and 4.41 can be combined resulting in equation 4.42.[11]

$$H_r = 5.73\epsilon S \left[ \left( \frac{T}{100} \right)^4 - \left( \frac{T_a}{100} \right)^4 \right] \quad (4.42)$$

All the relevant thermal equations have been determined to calculate the steady-state heat transfer. These equations are used to construct the sequence of non-linear equations in order to solve the model.

#### 4.2.5. Heat Transfer in Series and Parallel

If a heat transfer needs to be determined through multiple surface or through different forms of heat transfer with one relation, the previous mentioned equations can be coupled to each other. In order to accomplish this the thermal resistance of each phase in the heat transfer needs to be determined. The thermal resistance for a conduction heat transfer relation is shown in equations 4.43.[12]

$$H_c = \frac{T_1 - T_2}{\underbrace{L/kS}_{\text{Thermal Resistance}}} \quad (4.43)$$

Depending on the form of transfer and the geometry of the system the heat resistance relation can vary. These thermal resistances can then be added in parallel or in series similar to electrical resistances. An example of a conductive and convective resistances added in series is shown in equation 4.44 and in parallel is shown in equation 4.45.[12]

$$H = \frac{\Delta T}{R_1 + R_2} = \frac{T_1 - T_2}{L/kS + 1/h_v A} \quad (4.44)$$

$$H = \frac{\Delta T}{\frac{1}{R_1} + \frac{1}{R_2}} = \frac{T_1 - T_2}{\frac{1}{L/kS} + \frac{1}{1/h_v A}} \quad (4.45)$$

In which ( $\Delta T$ ) is the change in temperature between the two desired locations and ( $R$ ) is the thermal resistance. The model uses a combination of heat transfer relations with thermal resistances in series and in parallel. The specific locations where these equations are applied are shown in section 5.1.

# 5

## The Thermal Model

Using the theory given in chapter 4 the thermodynamic model was constructed. This is a general model that can predict the steady-state temperature of this novel transmission for numerous applications, one of which is the DOT wind-turbine. In this chapter an overview of the model will be given, starting with the modeling approach, given in section 5.1 and concluding with an explanation of the model, given in section 5.3.

### 5.1. Modeling Approach

In this section the modeling approach will be discussed. The assumptions made and the thought behind the model are explained and an overview of the solving method is given. The model takes the geometry of the drive and splits it up into key components. An overview of all the main components can be seen in figure 5.1.

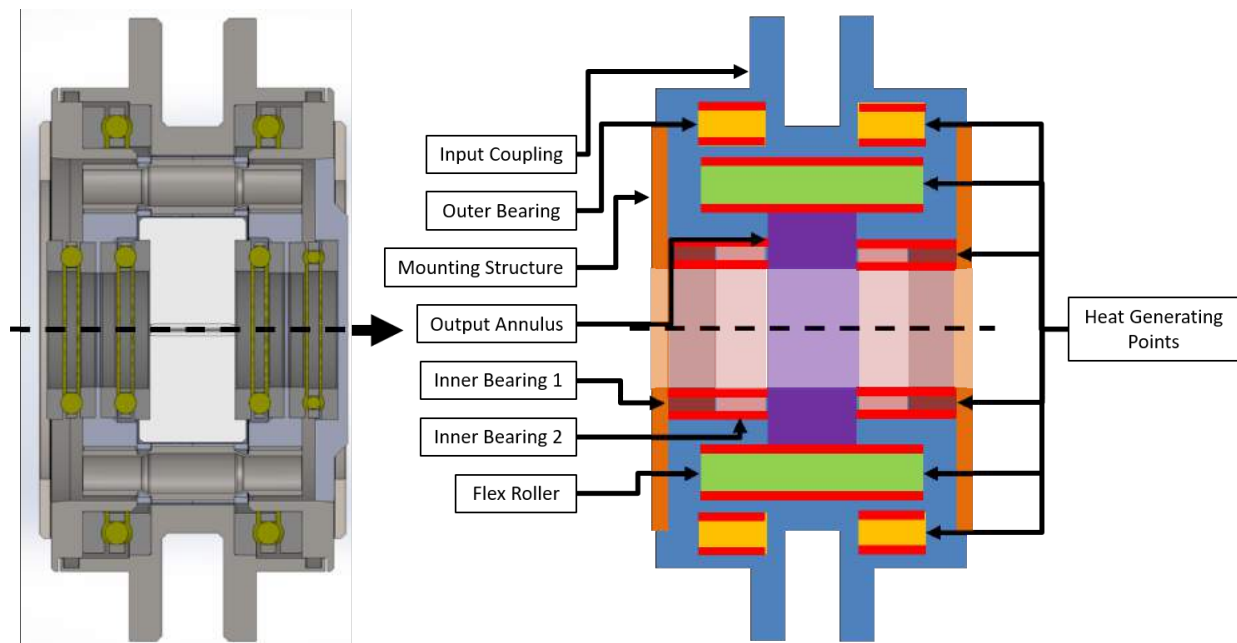


Figure 5.1: Overview of the model with all key components (not to scale)

Figure 5.1 shows a cross-section cut-out of the DOT transmission on the left and a simplified version of it on the right. The figure indicates that the drive can be split-up into seven separate components. These components affect the final temperature of the system in different ways. These will be discussed further in this section. Additionally, the heat generation points are identified, these points coincide with the location of the bearings and flex-rollers. At those locations the heat generation power, calculated using the equations shown in section 4.1, were implemented. A single node in this model is seen as a thin and narrow cylindrical

curved beam, with user defined axial length and radial thickness. Within this 'nodal cylinder' the temperature will be homogeneous throughout its thickness and across its circumference. The model can be split-up into two main sections; the modeling of the general structure (section 5.1.1) and the modeling of the flex-rollers (section 5.1.2). Each of these sections use a different set of heat transfer equations. These equations depend on the assumptions made and the boundary conditions of the system.

### 5.1.1. Modeling the General Structure

The modeling approach in the general structure uses the nodal network which is discussed in section 4.2.1. As stated a nodal network is used to calculate the temperature at a specific point in the gearbox. These multiple nodes are arranged into a matrix and are location dependent, meaning that each node interacts with those directly around it. Based on the type of heat transfer interaction and the boundary conditions a thermal heat transfer equation can be written for each node. There are two main types of boundary conditions in the thermal model; the ambient temperature during operation and the thermal energy generated by the bearings and flex-roller discussed in section 4.1. Each of the equations describing the heat transfer per node has the temperature of the surrounding nodes and the flow/material properties as input to calculate the temperature of that specific node. The nodal network will result in a string of a non-linear equations that will need to be solved simultaneously to calculate the steady-state temperature of all the nodes. In the main structure, the heat transfer relations stated in section 4.2 were used. An example of a relation used to calculate the temperature of a node is shown in figure 5.2 and equation 5.1.

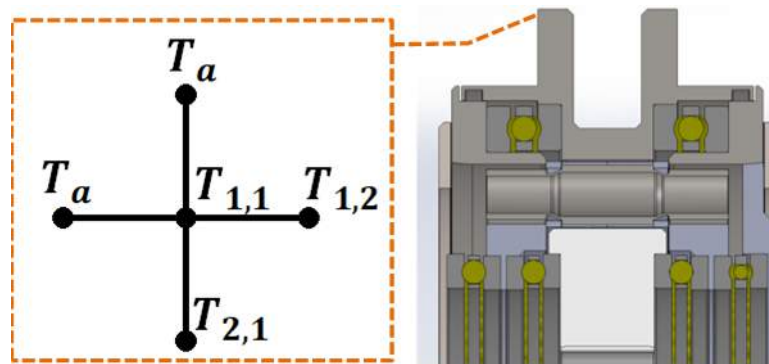


Figure 5.2: Example of a single node calculation in nodal network of the DOT transmission

$$\begin{aligned}
 0 = & \underbrace{\frac{kS_{wall}}{L}(T_{1,2} - T_{1,1}) + \frac{2\pi kW(T_{2,1} - T_{1,1})}{\ln(R_{1,1}/R_{2,1})}}_{\text{Conduction}} + \underbrace{(h_{axial})S_{wall}(T_a - T_{1,1})}_{\text{Convection}} \\
 & + \underbrace{(h_{radial})S_{cylinder}(T_a - T_{1,1})}_{\text{Convection}} + \underbrace{5.73\epsilon(S_{wall} + S_{cyl})\left[\left(\frac{T_{1,1}}{100}\right)^4 - \left(\frac{T_a}{100}\right)^4\right]}_{\text{Radiation}}
 \end{aligned} \tag{5.1}$$

As can be seen in figure 5.2 the chosen node is on the top left corner of the input annulus. In this example node, there are four nodes which have a thermal interaction with it. There will be conductive heat transfer in the axial and radial direction with the nodes to the right and below, convective heat transfer from a vertical wall with the node to the left and from a horizontal cylinder with the node on top and radiation with the external environment. The resulting equation to describe the node is shown in equation 5.1. As can be seen this node is in contact with a boundary condition, the ambient temperature. Using this boundary condition the temperature of the surrounding nodes can be calculated. Depending on the location there are a variety of different equations that need to be used. If the node is situated in the structure only, conduction takes place in both radial and axial directions. If a node makes contact with the external environment a convection and radiation equation must be used. Finally, if the node is located on the contact point of the bearing or the flex-roller the heat generation equations shown in section 4.1 needs to be implemented in the heat transfer equation. The structure is composed out of multiple rotating annuli, meaning that it cannot be seen as a single solid cylinder. Additional measures have been taken in the thermodynamic model to ensure that the

interaction of those cylinders with different rotational velocities are taken into consideration. An illustration of how the annuli are divided in the model is shown in figure 5.3.

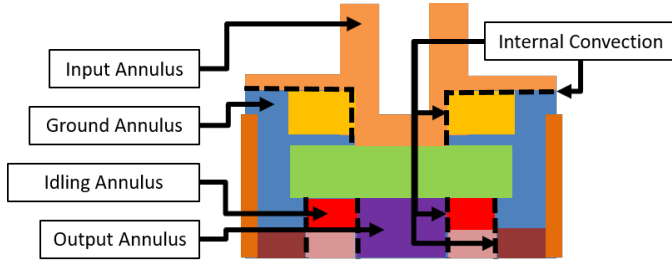


Figure 5.3: Illustration of structure components

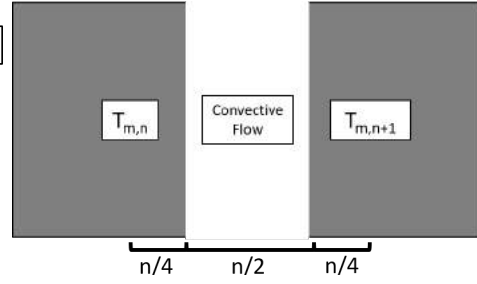


Figure 5.4: Convective heat transfer interaction

Figure 5.3 illustrates the location of the annuli with their dividing lines in the main structure of the drive. It can be deduced that there are four annuli rotating at different velocities. Each of these annuli are not in contact with each other, meaning that an air/lubricant pocket is present in between them. Therefore, convection is the main form of heat transfer in between those four rotating cylinders. The nodal interaction at that location is different, an illustration of that interaction can be seen in figure 5.4. The two nodes indicated in the figure are separated by a layer of convective air. It is assumed that this layer starts at a quarter of the node length. Additionally, velocity of the air is assumed to be equal to the rotational velocity of the node at that point. Each annuli has a different rotational velocity, with that velocity corresponding to the flex-roller's contact velocity with that annulus, as shown in section 4.1.3. The final velocity of the flow is the difference in velocity between the two rotating components. Once the velocity is known, the equations for forced convective heat transfer in section 4.2 can be used to determine the convective film coefficient. The heat transfer equation for axial heat transfer between the annuli is shown in equation 5.2 and in radial direction in equation 5.3. These equations use the theory of heat resistances in series and parallel explained in section 4.2.5.

$$H_{ax} = \frac{T_{m,n+1} - T_{m,n}}{\frac{0.25n}{kA} + \frac{1}{h_{avg}A} + \frac{1}{h_{avg}A} + \frac{0.25n}{kA}} \quad (5.2)$$

$$H_{rad} = \frac{T_{m-1,n} - T_{m,n}}{\frac{\ln((r_{m-1,n})/(r_{m-1,n}-0.25n))}{2\pi kn} + \frac{1}{h_{avg}A} + \frac{1}{h_{avg}A} + \frac{\ln((r_{m,n}+0.25n)/(r_{m,n}))}{2\pi kn}} \quad (5.3)$$

In which ( $T$ ) is the temperature of the nodes, ( $n$ ) is the node length, ( $k$ ) is the conductive thermal coefficient, ( $h$ ) is the convective film coefficient, ( $r$ ) is the radius of the node and ( $A$ ) is the area perpendicular to the heat transfer. Equation 5.2 describes the situation shown in figure 5.4, there are four different thermal resistances in the heat transfer equation. These are conduction through the material of the structure, convection from the wall to the air, convection from the air to the wall and the final conduction through the material. Equation 5.3 has the same thermal resistances as equation 5.2, described in radial direction rather than axial. These two equations are used together with the other heat transfer equations to determine the final steady-state temperature of the system.

### 5.1.2. Modeling the Flex-Rollers

At the location of the flex-rollers, the heat propagates through multiple surfaces and materials. In this section of the drive, the geometry consists of multiple hollow cylinders rolling in a bath of lubrication. This is shown in figure 5.5.

Figure 5.5 shows the cross-section of the drive from multiple angles. The picture on the left is the side view, the one on the top right is the side view with only the outline of the flex-rollers showing and the bottom right is a front view cut-out of the drive. The red box on the bottom right picture indicates one node in the drive and as explained previously, it is a square section with equal length in radial and axial direction. Since the model assumes that the circumferential temperature is homogeneous, the model must be made so that the heat transfer is modeled accurately in the flex-roller section. Looking at the top right picture it can be seen that one node passes through the material of multiple flex-rollers and the lubrication in between those flex-rollers.

This means that multiple forms of heat transfer are present in a single node. To take these multiple forms into account the model needs to be adjusted. The assumption used by the model can be seen in figure 5.6.

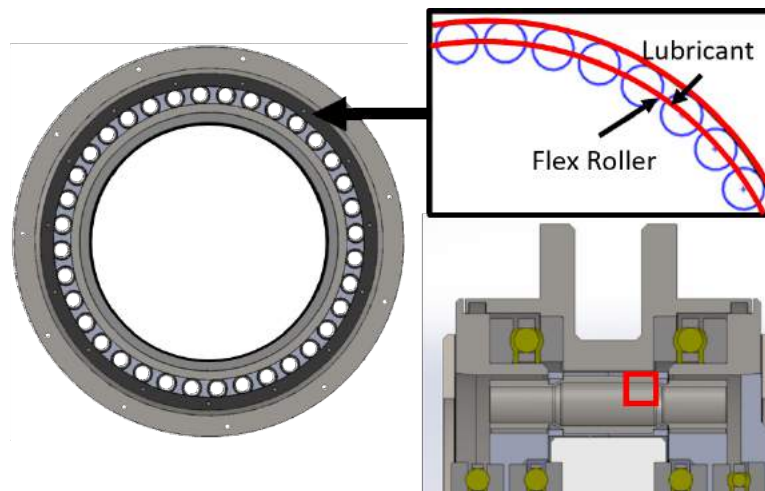


Figure 5.5: Illustration of the flex-roller geometry with node, one node is illustrated by the red square (bottom right) and it propagates in circumferential direction through the multiple flex-rollers (top right)

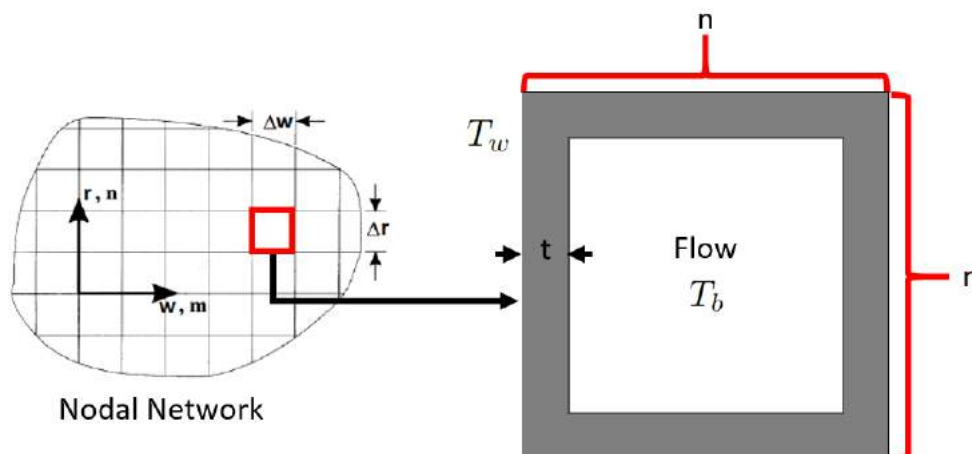


Figure 5.6: Illustration of flex-roller node simplification, node is assumed to be a square beam with thickness ( $t$ ) depending on the flex-roller density around the transmission's circumference, with a lubricant flowing inside of it

Figure 5.6 illustrates that a single node in the flex-roller section is assumed as a node with a specific wall thickness ( $t$ ) forming a 'nodal channel' around the circumference of the drive, where the lubricant is flowing through. In between the walls, convective heat transfer is assumed and within the wall's structure, conduction is assumed. Depending on the Reynolds number of the flow, either laminar or turbulent flow is present in between the walls. The velocity of the liquid inside of the walls is assumed to be equal to the velocity that the flex-rollers move around the circumference of the drive. The wall thickness is determined by the amount of volume the flex-rollers take up around the circumference of the 'nodal cylinder' compared to the lubricating liquid. This thickness is a function of the flex-roller geometry, node size and node position. If the number or thickness of the flex-roller increases, the wall thickness of the node increases. Since multiple nodes in radial direction are used to describe the flex-roller section and the geometry of the flex-roller is not constant throughout the drive's radius, the wall thickness will change depending on the node's radial position. An overview of the nodal network is shown in figure 5.7.

Figure 5.7 illustrates multiple nodes with varying wall thicknesses in radial direction. The figures on the left shows the position of the nodes from the front and side. As can be seen a node is a thin and narrow circular

curved beam with the same thickness in radial and axial direction. The illustration on the right in figure 5.7 shows that the wall thickness of the nodes remain the same in axial direction but varies in radial direction. The nodal section with thickness ( $t_1$ ) is located at the top of the flex-roller, meaning that around the circumference, the volume of the top section of all the flex-rollers need to be taken into consideration. While for section with ( $t_2$ ), only the volume of the flex-roller's middle section is taken. Additionally, the radius is different, affecting the thickness further. To calculate the total volume that the flex-rollers occupy in a node, equation 5.4 is used. This results is then multiplied by the length and number of flex-rollers.[28]

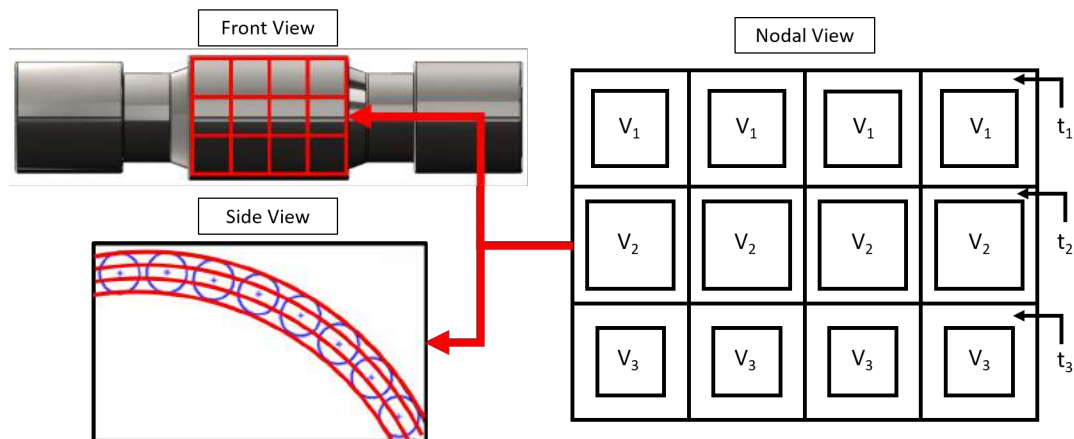


Figure 5.7: Overview of flex-roller nodal network

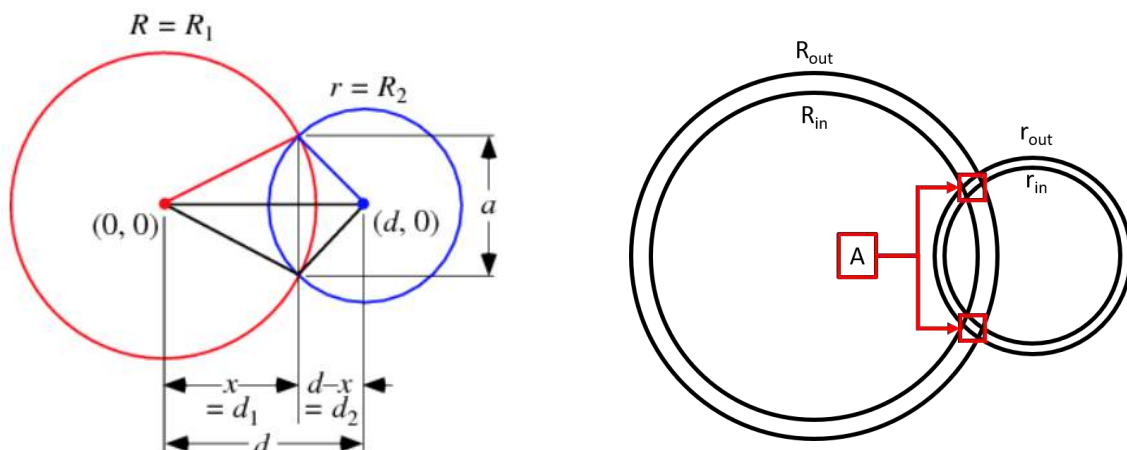


Figure 5.8: Illustration of circle-circle intersection [28]

Figure 5.9: Location of the area that needs to be calculated

Figures 5.8 illustrates the variables used in the area calculation. With the aid of this figure the area of two overlapping circles with different radii can be calculated. Since the area of the flex-roller, a hollow cylinder, needs to be calculated within a 'nodal cylinder', the area of multiple overlapping circles need to be determined. Figure 5.9 shows a specific area that the model calculates. The resulting equations used to calculate the area and the volume of that section are shown in equations 5.4 [28] and 5.5.

$$A = r^2 \cos^{-1} \left( \frac{d^2 + r^2 - R^2}{2dr} \right) + R^2 \cos^{-1} \left( \frac{d^2 + R^2 - r^2}{2dR} \right) - 1/2 \sqrt{(-d+r+R)(d+r-R)(d-r+R)(d+r+R)} \quad (5.4)$$

$$V = L_{FR} Z_{FR} (A(R_{out}, r_{out}) - A(R_{out}, r_{in}) - (A(R_{in}, r_{out}) - A(R_{in}, r_{in}))) \quad (5.5)$$

In which  $(R_{in}, R_{out})$  are the radius of the inner and outer 'nodal cylinder',  $(r_{in}, r_{out})$  are the radius if the inner and outer part of the flex-roller,  $(d)$  is the distance between both mid-points,  $(L_{FR})$  the length of the flex-roller and  $(Z_{FR})$  is the number of flex-rollers. Using the result of equation 5.5 and dividing it by the total volume of the 'nodal cylinder' makes it possible to find the percentage that the flex-roller occupies. This percentage is then used to determine the wall thickness of each node as shown in figure 5.7. The next step is determining the heat equations which describe the heat transfer. A detailed overview of a single flex-roller node and its interaction in radial and axial direction is shown in figure 5.10.

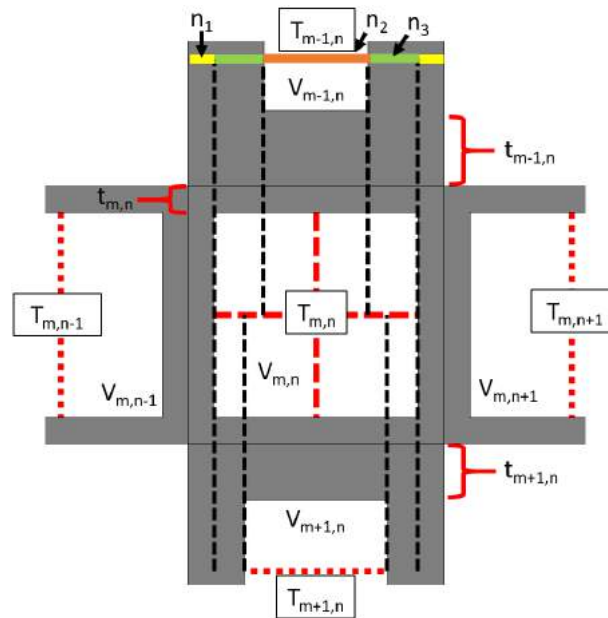


Figure 5.10: Detailed overview of flex-roller node interaction in the flex-roller section, wall thickness and flow velocity changes in radial direction per node'

Figure 5.10 shows a single node with its surrounding nodes. In the figure, each node has a different temperature which affects the final temperature of the selected node. Looking at the nodes in axial direction the wall thickness and velocity of the lubricant in the "nodal channel" is the same. This is because in axial direction the flex-roller volume and lubricant velocity does not change due to them having the same "nodal cylinder" radius. The nodes in radial direction do have a different wall thickness and fluid velocity due to the changing radius of the "nodal cylinder". The heat from one node to another needs to pass through two materials with different forms of heat transfer. Additionally, depending on where the heat transfer takes place, there could be only conduction through the walls or a combination of conduction and convection. At the top of figure 5.10 three lengths ( $n_1$ ,  $n_2$  and  $n_3$ ) are identified. It is assumed that the propagation of heat is only in radial directions with the nodes directly on top and below of the selected node and only in axial direction with the nodes directly next to the selected node. Looking at the heat transfer relation in radial direction for section length ( $n_1$ ) only conductive heat transfer is assumed, for section length ( $n_2$ ) convective then conductive then convective heat transfer is assumed and for section length ( $n_3$ ) conductive then convective heat transfer is assumed. To determine the complete heat transfer between the interaction of the two nodes equation 5.6 is used, this equations is explained further in section 4.2.5.

$$H_{tot} = \frac{\Delta T}{1/\sum_{n=1}^n R_n} \quad (5.6)$$

In which  $(\Delta T)$  is the change in temperature between the two nodes and  $(R_n)$  is the thermal resistance of the different nodal section lengths acting in parallel. An illustration of the thermal resistance in axial direction is shown in figure 5.11 and in radial direction with the top node is shown in figure 5.12.

Figure 5.11 shows that in axial direction there are two parallel thermal resistances, one through the "nodal channel" wall and one through the lubricant liquid and the wall. The variables  $(A_1)$  and  $(A_2)$  in figure 5.11 are the areas of these two parallel thermal resistance paths. In radial direction, there are three parallel thermal

resistance paths as explained previously. The variables ( $n_1$ ,  $n_2$  and  $n_3$ ) and ( $A_1$ ,  $A_2$  and  $A_3$ ) represent the three separate section lengths and areas for the each path, as shown in figure 5.10. The resulting two thermal resistance equations for axial direction are shown in equation 5.7 and 5.8.

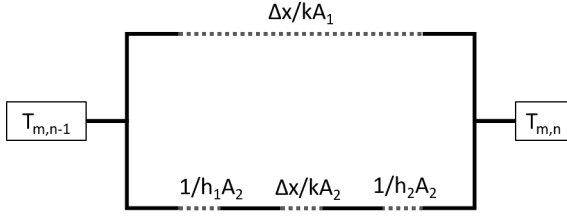


Figure 5.11: Thermal resistance in axial direction in the flex-roller section

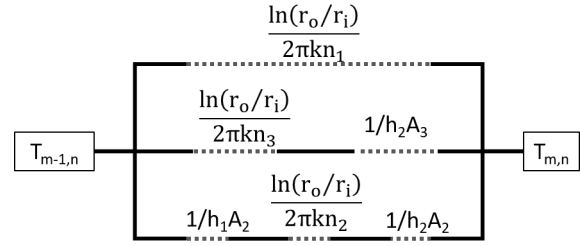


Figure 5.12: Thermal resistance in radial direction in the flex-roller section

$$R_{ax1} = \frac{n}{kA_1} \quad (5.7)$$

$$R_{ax2} = \frac{1}{h_{avg}A_2} + \frac{2t}{kA_2} + \frac{1}{h_{avg}A_2} \quad (5.8)$$

These equations are determined using the thermal resistance paths shown in figure 5.11. The areas ( $A_1$ ) and ( $A_2$ ) are the areas of the two thermal channels and ( $h_{avg}$ ) is the convective heat transfer coefficient at the midpoint of the node, calculated using the relations for forced convection shown in section 4.2.3. The resulting three thermal resistance equations for radial direction with the top node are shown in equation 5.9, 5.10 and 5.11.

$$R_{rad1} = \frac{\ln(r_{n-1,m}/r_{n,m})}{2\pi kn_1} \quad (5.9)$$

$$R_{rad2} = \frac{1}{h_{wall}n_2 2\pi(r_{n,m} + 0.5n + t_{m-1,n})} + \frac{\ln((r_{n,m} + 0.5n + t_{m-1,n})/(r_{n,m} + 0.5n - t_{m,n}))}{2\pi kn_2} + \frac{1}{h_{wall}n_2 2\pi(r_{n,m} + 0.5n - t_{m,n})} \quad (5.10)$$

$$R_{rad3} = \frac{\ln(r_{n-1,m}/(r_{n,m} + 0.5n - t_{m,n}))}{2\pi kn_3} + \frac{1}{h_{wall}n_3 2\pi(r_{n,m} + 0.5n - t_{m,n})} \quad (5.11)$$

In which ( $r$ ) is the radius of the midpoint of the node, ( $t$ ) is the wall thickness of the thermal channel as shown in figure 5.10, ( $n$ ) is the nodal section length and ( $h_{wall}$ ) is the convective heat transfer coefficient at the wall. These equations are determined using the thermal resistance paths shown in figure 5.12. The convective heat transfer coefficient ( $h_{wall}$ ) is calculated by using the velocity of the flow at the wall in between the nodes, using the relations shown in section 4.2.3. Depending on the channel wall thickness of the two nodes, equation 5.11 could change by first having convective heat transfer then conductive. Additionally, if the surrounding nodes are within the main structure of the drive the heat transfer relations are changed. This is because if a surrounding node is not in the flex-roller section it is assumed that a singular solid material is modeled rather than a 'nodal channel'. The resulting thermal resistance equations for axial direction are shown in equations 5.12 and 5.13 and radial direction are shown in equations 5.14 and 5.15

$$R_{ax1} = \frac{n}{kA_1} \quad (5.12)$$

$$R_{ax2} = \frac{0.5n + t}{kA_2} + \frac{1}{h_{avg}A_2} \quad (5.13)$$

$$R_{rad1} = \frac{\ln(r_{n-1,m}/r_{n,m})}{2\pi kn_1} \quad (5.14)$$

$$R_{rad2} = \frac{\ln(r_{n-1,m}/(r_{n,m} + 0.5n - t_{m,n}))}{2\pi kn_2} + \frac{1}{h_{wall}n_2 2\pi(r_{n,m} + 0.5n - t_{m,n})} \quad (5.15)$$

The relations differ because only conductive heat transfer in the surrounding node is taken into consideration. The final heat transfer relations for axial and radial direction are calculated using equations 5.16 and 5.17.

$$H_{ax} = \frac{T_{m,n-1} - T_{m,n}}{1/R_{ax1} + 1/R_{ax2}} \quad (5.16)$$

$$H_{rad} = \frac{T_{m-1,n} - T_{m,n}}{1/R_{rad1} + 1/R_{rad2} + 1/R_{rad3}} \quad (5.17)$$

Each node will have a heat transfer relation taking the two axial and two radial directions into account. This relations can then be solved simultaneously to find the final steady-state temperature.

## 5.2. Non-Linear Equation Solver

The matrix filled with non-linear thermodynamic equations is solved simultaneously using the python script 'scipy.optimize.fsolve'. [29] This script uses hybrid algorithms within MINPACK, which is a library of the FORTRAN subroutines. [29] The script solves the sequence of equations by using a modification of the Powell hybrid method. [31] The Powell method is a derivative-free and robust optimization method. [30] Additionally, it does not require the input of a Jacobian matrix, making it better applicable to solve a large set of multidimensional non-linear equations. [31] To solve the system of non-linear equations the unique heat transfer equation and an initial guess of the final steady-state temperature per node is entered in the python script. Using the first estimate, a new optimized estimate is calculated. This optimized estimate is then used as input and the process repeats until the estimation error (difference between input and output) decreased to an acceptable value. In the thermal model the amount of non-linear equations changes depending on the chosen node size. An analysis on how node size affect computational time and accuracy can be found in section 5.3.2.

## 5.3. Program Explanation

The program created to model the thermodynamic properties of the system is explained in this section. An introduction of the model will be given first, then the working principles are explained using a pseudo-code. Once the pseudo-code is given the effects of the nodal network spacing are discussed. The thermodynamic model takes the geometry and operating condition of the drive as input and generates a steady-state temperature heat-map as output. There are two main loops in the program; (1) determining the geometry and input heat of the components in the system and modeling those over the cross-section and (2) using a nodal network to model the heat distribution to determine the final steady-state temperature throughout its cross-section. These steps are visualized in figure 5.13.

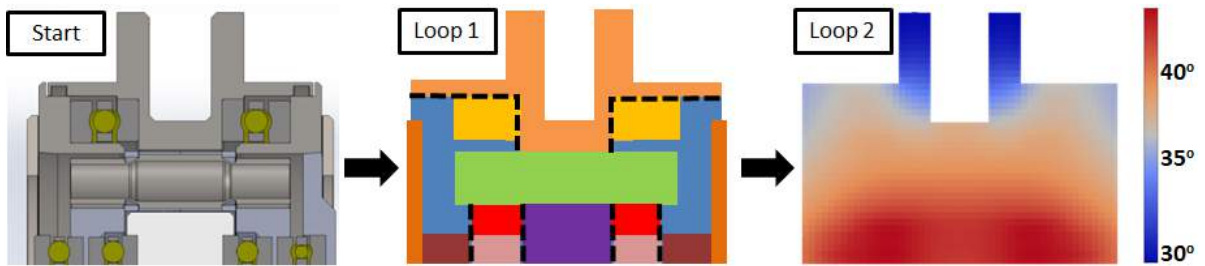


Figure 5.13: Illustration of the steps taken in the program, loop 1 divides the input in main components, loop 2 uses main components to create heat-map

Looking at figure 5.13 the general working principle of the model can be identified. The first illustration visualizes the initial cross-section of the drive. Based on this cross-section the geometry of all the components is identified and inserted as input into the program. Based on these inputs the second figure is generated. The geometry of all components shown in the second figure in combination with the heat generated per component, which is calculated in the program and is based on the operating condition, results in the final figure.

This final figure (on the right) is a heat-map of the steady-state temperature.

An overview of the cross-section of the drive with all the components identified by the program is given in figure 5.1. The program identifies the seven main components; the input coupling (or annulus), the outer bearings, the two inner bearings, the flex-roller section, the output annulus and the mounting structure. Additionally, it locates the position where there is an air gap in between the annuli, as explained in section 5.1.1. Based on the sizing and design properties of the components the system's heat inputs can vary. These heat properties are calculated by the model and are inserted into the system to calculate the final steady-state temperature. The geometry of all components can be altered to match the drive that is being designed. An example heat-map generated by the model is shown in figure 5.14. This heat-map is used to illustrate the output of the thermal model, the resulting heat-map of the DOT wind-turbine is shown in chapter 7.

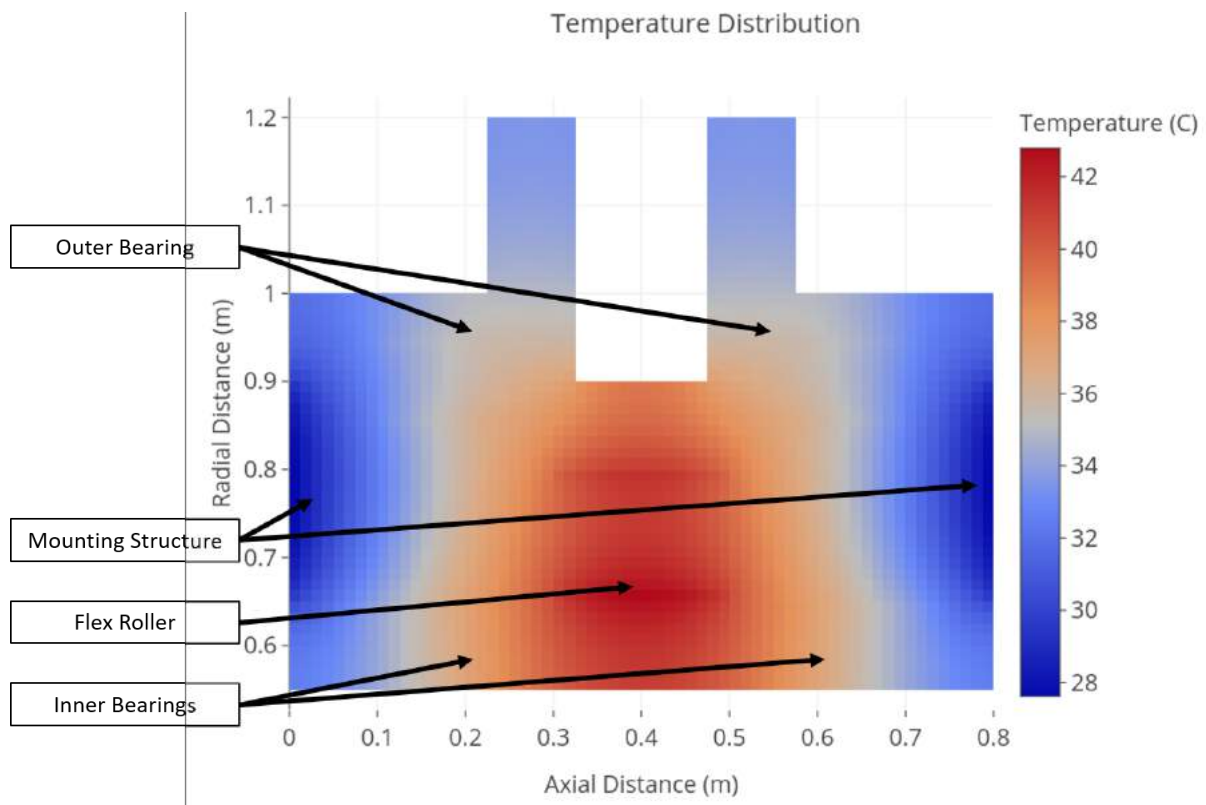


Figure 5.14: Example result of thermal model showing the effect of each component

Figure 5.14 indicates the final steady state heat-map of a given system. This heat-map illustrates the heat distribution throughout the structure in radial and axial direction. It is assumed as stated previously, that the drive transfers heat homogeneously around the circumference. Therefore figure 5.14 indicates the given temperature at any point around the circumference of the transmission. The figure models the drive with a radius of 0.55 to 1.2 meters and a width of 0.8 meter as indicated by the x and y axis. The steady-state temperature, varying from red (hot) to blue (cold) is indicated in the legend on the right. For this example the temperature varies between of 42 to 28°C. The location of each component is also indicated, this shows how it affects the heat generation and propagation of the system. The bearings and flex-roller are responsible for the heat increase in the system. This power is determined by the operating condition and is calculated using the equations in section 4.1. The heat is dissipated to the environment through convection, radiation and conduction through the mounting structure. Using this heat-map the final steady-state temperature can be visualized. A more detailed explanation of the working principle of the model is given in section 5.3.1.

### 5.3.1. Working Principle of Model

The top level pseudo-code for the model is given in algorithm 1. The code consists of all the theoretical information described in chapter 4. Looking at the pseudo-code it can be seen that the model takes the geometry,

boundary conditions, constants and operating condition of the drive as input and returns a matrix of the resulting steady-state temperature of the drive system.

Firstly, the heat generated by all the key components are determined. This is done by using the relations shown in section 4.1. The key heat generating components are the inner and outer large diameter bearings, the inner and outer small diameter bearings and the flex-rollers. Depending on the drive the amount of bearings may vary resulting in a lower amount of heat generating components. This information is implemented by the user at the start of the code. From the drives operating condition and geometry the heat power is calculated per component and is implemented in the vector ( $Q$ ). The thermodynamic heat dissipation functions can now be created. The theory behind the functions that are used is explained in section 4.2. There are 5 sets of heat transfer relations; conduction within the structure (section 4.2.2), free or forced convection with the external environment (section 4.2.3), radiation with the external environment (section 4.2.4), forced convection internally between the rotating annuli (section 5.1.1) and heat transfer within the flex-roller section (section 5.1.2). These sets of heat transfer relations have a separate axial and radial function, resulting in a minimum of 10 heat transfer functions. These heat transfer function depend on the geometry and the temperature. The functions are named according to their form of heat transfer and their direction. These functions will be used at a later stage in the code, once the heat transfer equation per node needs to be made.

The next section of the code determines the number of rows and columns required in the output temperature matrix. These values depend on the initial user defined nodal spacing. All heat generating components are also identified so they can be called on later in the code. Once the nodal spacing, component numbering and heat transfer functions have been determined the next phase of the code can commence. A double for-loop is executed which runs from zero to the previously determined number of rows and columns in the system. This part of the code runs through every node in the system and determines where that node is based on the geometry. When the position is known it assigns a number to that node indicating what component it is on. This is done through multiple if-else statements. There are seven key components in the system ranging from the bearings to the annuli. The boundaries between these components are also identified so that it can be modeled later using internal forced convection. If a node is within the flex-roller section, the code determines the volume ratio of that node by using relations 5.4 and 5.5. This ratio is then inserted in a separate flex-roller vector ( $FR$ ). This double for-loop returns a position matrix ( $X$ ) which has its values numbered 0 through 7 depending on which component the node simulates and a flex-roller volume ratio ( $FR$ ).

When the position of each node is determined, the function to calculate the heat transfer power per node can be determined. This function has a matrix as input which gives the temperature for each node ( $T$ ), based on those temperatures the total heat power of each node can be calculated. The value for ( $T$ ) is unknown and needs to be calculated using a non-linear simultaneous equation solver used at a later stage in the code. In order to calculate the temperature power, a unique heat transfer equation must be written for each node. To do this a heat power function ( $Pwr$ ) was written. It uses a double for-loop which goes through all the rows and columns. The double for-loop looks at every node and its surrounding nodes using the position matrix ( $X$ ). It then uses an if-else statement to determine first, which node it is, then, looks at the nodes it is in contact with in both radial and axial directions. Based on those findings, it assigns a heat transfer equation, defined earlier in the code, to each interaction it has with its surrounding nodes. Additionally, if a given node falls on a heat source (this includes the rolling surface of the bearings or flex-rollers) a heat input calculated in vector ( $Q$ ), will be added to the heat equation. This results in multiple unique heat transfer relations for different nodes, describing the heat dissipation throughout the complete system. The heat power generated by each node is then calculated using matrix ( $T$ ) and the result is set in a matrix ( $p$ ).

Using the function ( $Pwr$ ) the system can then be solved for steady-state condition by setting the power of each node ( $p$ ) to zero and solving for the temperature ( $T$ ). This is done in the function ( $fsolve$ ), by using the modified Powell hybrid method to determine the roots to non-linear equations. The user must implement an initial guess and the code will run the power function ( $Pwr$ ) with that guess and use the output to determine new input values. This process continues until the output matrix ( $p$ ) is equal to zero. A more detailed explanation on this method is given in section 5.2. Once the steady-state temperature has been solved, it is the plotted in radial and axial direction to result in the heat-map shown in figure 5.14.

**Data:** Radius, diameter and width of key components as geometry matrix ( $G$ )  
 Rotational velocity ( $rpm$ ) and torque of drive ( $Tor$ )  
 Bearing ( $B$ ), flex-roller ( $FR$ ), lubricant ( $Lub$ ), air ( $Air$ ) and structural material constants  
 Nodal Spacing ( $n$ )

**Result:** Matrix with steady-state temperature distribution in the drive ( $T$ )

**begin**

- Calculate force and velocities of flex-rollers and bearings using ( $G$ ), ( $rpm$ ) and ( $Tor$ );
- Calculate heat generation power ( $Q$ ) of the flex rollers and bearings using forces and velocities;
- Calculate the Prandtl number ( $Pr$ ) of air and lubrication using ( $Lub$ ) and ( $Air$ );
- Function:** Conduction in axial ( $Con_{ax}$ ) and radial ( $Con_{rad}$ ) direction;  
 Using geometry ( $G$ ), structural material constants and node temperature ( $t$ );
- end**
- Function:** Convection free or forced externally in axial ( $Cov_{ax}$ ) and radial ( $Cov_{rad}$ ) direction;  
 Using geometry ( $G$ ), air constants and node temperature ( $t$ );
- end**
- Function:** Radiation in axial ( $Rad_{ax}$ ) and radial ( $Rad_{rad}$ ) direction;  
 Using geometry ( $G$ ), structural material constants and node temperature ( $t$ );
- end**
- Function:** Convection forced internally in axial ( $fiCov_{ax}$ ) and radial ( $fiCov_{rad}$ ) direction;  
 Using geometry ( $G$ ), air and lubrication constants and node temperature ( $t$ );
- end**
- Function:** Heat transfer flex-roller section in axial ( $Cov_{FRax}$ ) and radial ( $Cov_{FRrad}$ ) direction;  
 Using geometry ( $G$ ), lubrication and material constants and node temperature ( $t$ );
- end**
- Determine amount of rows ( $r$ ) and columns ( $c$ ) based on geometry ( $G$ ) and nodal spacing ( $n$ );
- Create empty position ( $X$ ), temperature ( $T$ ) and power ( $p$ ) Matrix/Vector using ( $r$ ) and ( $c$ );
- for** Row in nodal network. first (0) to last ( $r$ ) **do**
- for** Column in nodal network, first (0) to last ( $c$ ) **do**
- Determine position of node based on geometry ( $G$ );
- Number node indicating different component (0) to (7);
- Insert number in position matrix ( $X$ );
- Calculate the volume ratio of nodes in flex-roller section;
- Insert number in volume ratio vector ( $FR$ );
- end**
- end**
- Calculate the wall thickness ( $dn_t$ ) of flex-roller section
- Function:** Heat power per node ( $Pwr$ );
- for** Row in nodal network. first (0) to last ( $r$ ) **do**
- for** Column in nodal network, first (0) to last ( $c$ ) **do**
- Determine interaction of node with surrounding nodes using ( $X$ );
- Write thermodynamic equilibrium equation per node using heat transfer functions;
- Insert heat transfer equation per node in power distribution vector ( $p$ );
- Calculate the power per node ( $p$ ) using input temperature matrix ( $T$ );
- end**
- end**
- end**
- Function:** Non-linear equation root solver ( $f solve$ );  
 Using function( $Pwr$ ) and initial guess ( $T_g$ );
- end**
- Return:** Non-linear root solver ( $f solve$ ) returns value of ( $T$ ) when power ( $p$ ) is set to zero;

**end**

**Algorithm 1:** Top-level pseudo-code of thermodynamic temperature solver

### 5.3.2. Nodal Density

Once the working principles of the program have been discussed the effect of the nodal density can be analyzed. In order to show how the nodal spacing affects the heat-map, the geometry shown in figure 5.15 was modeled. This geometry is a solid cylinder with an outer and inner radius of 1 and 0.4 m respectively and a width of 1 m. In this cylinder a single bearing is acting, modeled by an additional cylinder inside the given outer cylinder. The contact point of the bearing cylinder on the main geometry is where the heat will be generated. The bearing will have a total power of 100 W going into heat generation and the structure is assumed to be made out of 52100 bearing steel. The remaining variables used are shown in table 5.1.

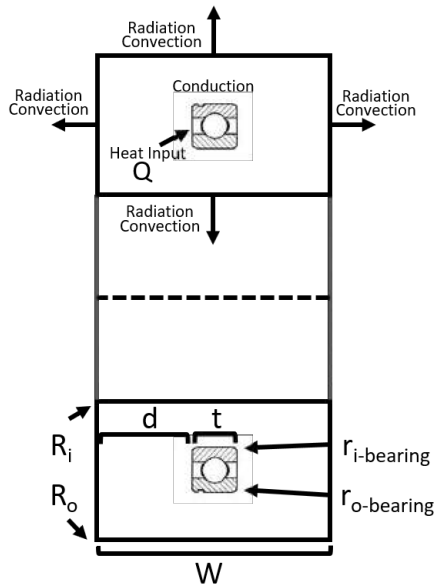


Table 5.1: Input variables in nodal density example

Variable	Description	Value	Unit
$R_o$	Outer Radius	1	m
$R_i$	Inner Radius	0.4	m
$W$	Width	1	m
$r_o$	Bearing Outer Radius	0.8	m
$r_i$	Bearing Inner Radius	0.6	m
$t$	Bearing Thickness	0.2	m
$d$	Bearing Axial Distance	0.4	m
$Q$	Input Bearing Power	100	W
$k$	Thermal Conductivity	36	W/(m K)
$\epsilon$	Emissivity	0.79	-
$T_a$	Ambient Temperature	20	C°

Figure 5.15: Geometry used in nodal density example

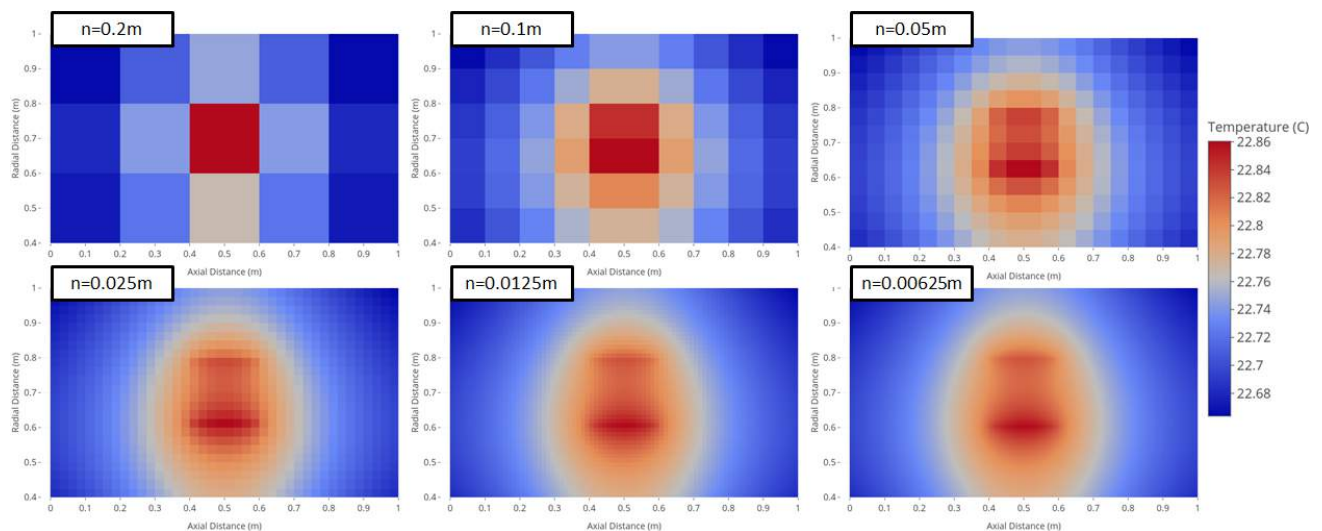


Figure 5.16: The effect of node size on the resulting heat-map, the node size started with 0.2m and is halved for each following heat-map

Looking at figure 5.15 it can be seen that all three modes of heat transfer are present. Conduction is the main form of heat transfer within the cylinder, conducting heat from the bearings to the external walls. Natural convection and radiation are used to transfer heat out to the external environment. This is done in both radial and axial direction. This geometry was then modeled with the thermodynamic program using six different nodal widths. The resulting steady-state heat-map with the different nodal spacing is shown in figure 5.16. The

computational times vary with each nodal spacing, a plot showing the effect of nodal width on computational time for this specific geometry is given in figure 5.17.

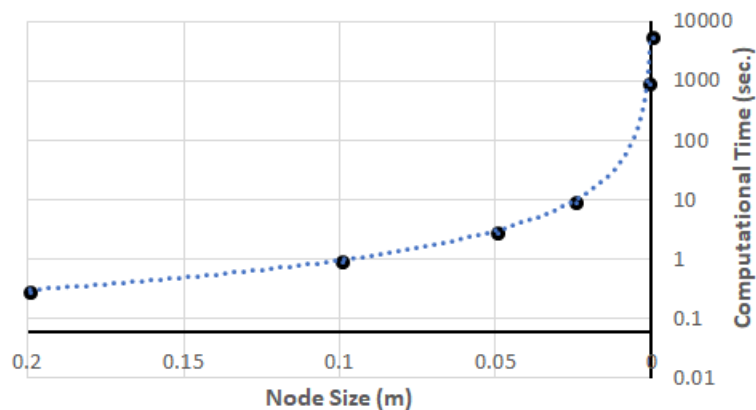


Figure 5.17: Computational time as a function of node size (Logarithmic Scale), the most optimum node size is 0.025m as it provides enough detail with a computational time of 10 sec.

Six different nodal spacing are indicated in figure 5.15. It starts with 0.2m on the top left and decreases to 0.00625m on the bottom right. Each change in the nodal spacing is half of the previous nodal spacing. Looking at the figure multiple conclusions can be drawn. The first is that more nodes result in a more detailed heat-map. This is evident by the difference in quality between the first and last figure. In the first figure the bearing is modeled by a single node and gives off a constant heat-flux. The smaller the nodes become, the more detailed the heat dissipation of the bearing becomes. The figures on the lower level clearly illustrate the heat generation at the bearing contact points, this is the location where the bearing makes contact with the surrounding structure. Despite this, the overall change in heat throughout the structure is relatively the same for all six cases, with a maximum temperature of 22.86°C and a minimum of 22.68°C. What can also be concluded, is that the heat dissipation is different when looking in the outward radial direction compared to the inward direction. The structure seems to be cooler on the outer wall as compared to the inner wall. This has to do with the geometry of the modeled object. Since the geometry is a cylinder, more surface area is available on the exterior wall compared to the interior, allowing for a greater surface area per node which increases convection and radiation.

For a given geometry there will be a trade-off between the nodal spacing and the computational time, as shown in figure 5.17. Computational time starts to greatly increase once the nodal spacing becomes less than 0.025 m. An optimum can be found between the two, looking at figure 5.16. An accurate enough image quality is when the heat inputs between the top and bottom of the bearing can be distinguished from each other. In this example it would be a nodal spacing of 0.0025m, resulting in a total of 960 nodes. Using this analysis it can be concluded that in order to generate an acceptable heat-map the node surface area should be at least 1000 times smaller than the cross-section surface area of the modeled geometry.



# 6

## Verification and Validation

In this chapter the thermal model used to calculate the steady-state temperature is verified and validated. The verification process is discussed first, followed by the validation of the model. In the verification procedure, multiple geometries were used to compare the results of the program with a third party software (ANSYS). During validation, a smaller version of the drive similar to the one used in the wind turbine, was run at multiple operating conditions. The steady-state temperature of that drive was then measured and compared with the calculated results of the model. Once the verification and validation process was complete the thermal model was used to predict the temperature of the the DOT drive during operation.

There are three main parts of the program that were verified and validated; (1) The heat power generated by the bearings and flex-rollers, (2) the simultaneous solving of the non-linear equations and (3) the final steady-state temperature. The heat power calculated by the program is discussed in section 6.2.4, where it was compared with the test results. The simultaneous solving of the non-linear equations is discussed in section 6.1.1, where a two dimensional model was verified. Lastly, the resulting steady-state temperature that the thermodynamic program calculates was verified and validated with multiple geometries throughout sections 6.1 and 6.2.

### 6.1. Verification

Multiple verification steps were conducted to verify the thermal model. First, the numerical solver used to solve the set of non-linear simultaneous equations was verified, this is done in section 6.1.1. Then in section 6.1.2, the steady-state temperature that the program calculates was verified with two simplified geometries. This was done by comparing the results attained from the thermal model with the results of a third party software (ANSYS). The first geometry does not contain flex-rollers while the second one does. Once both geometries were verified, the model could be validated by comparing the steady-state temperature the model calculates to the those measured during the validation test.

#### 6.1.1. Simultaneous Equation Solver Verification

Prior to using the thermal model with different geometries, the simultaneous equation solver had to be verified. This was done by comparing the results of the code to an independent calculation. If both approaches had the same result, the simultaneous non-linear equation solver should be verified. In order to accomplish this a simplified cross-section was used, as shown in figure 6.1. The figure is a cylinder composed out of two sections. The illustration on the left shows a three dimensional view of the geometry while the picture on the right shows a cut-out of the cylinder through its axis of symmetry in axial direction. Each section was described by a node, located at the axial and radial center of that given section, with a nodal spacing ( $n$ ) away from one another. These nodes, like in the final thermodynamic model, represented the heat propagation in radial and axial direction. It was assumed that the heat was distributed equally along the circumference therefore the tangential heat dissipation was not required.

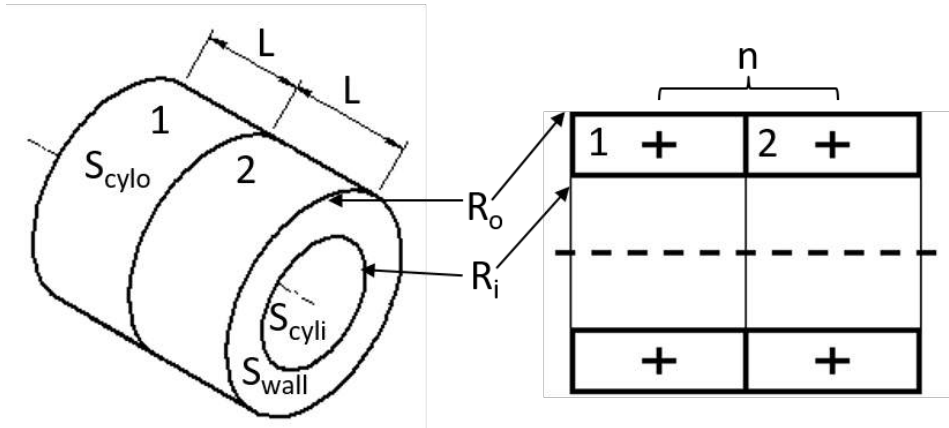


Figure 6.1: 3D illustration (left) and 2D cut-out (right) of geometry used in solver verification, it is cylinder modeled by two nodes

Each section in figure 6.1 was described as a function of the inner ( $R_i$ ) and outer radius ( $R_o$ ) and its length ( $L$ ). In figure 6.1 the sections are indicated with the number 1 and 2. To simplify the calculation the temperature was assumed constant within each section. Having large nodal sections compared to the overall geometry of the system made for a rough heat dissipation model. This was done with this model to remain within two dimensions so the simultaneous equation solver can be verified. The moment the number nodes increase the resolution and accuracy of the model increases greatly, as shown in section 5.3.2. As explained in that section, there will be a trade-off between computational time and resolution, the most optimum results can be obtained by using a nodal surface area that is a 1000 times smaller than the cross-sectional cut-out area. In the following sections the nodal density will be much greater. The resulting nodal network for the situation shown in figure 6.1 along with all input variables are given in figure 6.2 and table 6.3. These input variables are those that the model required in order to calculate the final steady-state temperature of the system. The result generated by the model was then compared to those attained by independent calculations made in this section to verify the solver.

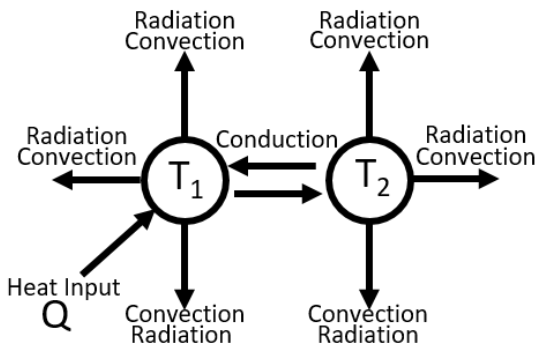


Table 6.1: Input variables in solver verification program

Variable	Description	Value	Unit
$R_o$	Outer Radius	1	m
$R_i$	Inner Radius	0.8	m
$L$	Length of Section	0.4	m
$n$	Nodal Spacing	0.4	m
$Q$	Input Power	100	W
$k$	Thermal Conductivity	36	W/(m K)
$\epsilon$	Emissivity	0.79	-
$T_a$	Ambient Temperature	20	C°

Figure 6.2: Illustration of the nodes in solver verification and their thermal interaction

Figure 6.2 illustrates the system shown in figure 6.1 as a nodal network. As shown, there are two nodes which transfer heat to each other using conduction, one node ( $T_1$ ) has a heat input ( $Q$ ) and the other ( $T_2$ ) does not. These two nodes describing sections 1 and 2 are both in contact with ambient air, therefore they use convection and radiation to transfer heat to the external environment. The heat is dissipated in an axial and both radial directions. The cylinder was assumed to be made out of steel. This gave the variables for thermal conductivity and emissivity shown in table 6.3. Using the previously mentioned information the heat transfer relations were written for each node. To aid with the calculations the simplified relations to determine the convective film coefficient, shown in equations 4.30 and 4.31 were used. The complete heat transfer relations are shown in equations 6.1 and 6.2 for nodes 1 and 2 respectively. These relations coincide with the nodal network illustration shown in figure 6.2. The theory used to determine these relations is explained in section

4.2. The last remaining variables that needed to be calculated are the two surface areas ( $S_{wall}$ ) and ( $S_{cyl}$ ), the relations used to calculate them are shown in equations 6.3 and 6.4.

$$0 = \underbrace{\frac{kS_{wall}}{n}(T_2 - T_1)}_{\text{Conduction, Axial}} + \underbrace{S_{wall} \left( 1.42 \left( \frac{T_1 - T_a}{R_o - R_i} \right)^{1/4} \right)}_{\text{Convection, Axial}} (T_a - T_1) + \underbrace{(S_{cyl_o}) \left( 1.32 \left( \frac{T_1 - T_a}{R_o} \right)^{1/4} \right)}_{\text{Convection, Outer Radial}} (T_a - T_1) + \underbrace{(S_{cyl_i}) \left( 1.32 \left( \frac{T_1 - T_a}{R_i} \right)^{1/4} \right)}_{\text{Convection, Inner Radial}} (T_a - T_1) + \underbrace{5.73\epsilon(S_{wall} + S_{cyl_o} + S_{cyl_i}) \left[ \left( \frac{T_a}{100} \right)^4 - \left( \frac{T_1}{100} \right)^4 \right]}_{\text{Radiation, Axial and Radial}} + Q \quad (6.1)$$

$$0 = \underbrace{\frac{kS_{wall}}{n}(T_1 - T_2)}_{\text{Conduction, Axial}} + \underbrace{S_{wall} \left( 1.42 \left( \frac{T_2 - T_a}{R_o - R_i} \right)^{1/4} \right)}_{\text{Convection, Axial}} (T_a - T_2) + \underbrace{(S_{cyl_o}) \left( 1.32 \left( \frac{T_2 - T_a}{R_o} \right)^{1/4} \right)}_{\text{Convection, Outer Radial}} (T_a - T_2) + \underbrace{(S_{cyl_i}) \left( 1.32 \left( \frac{T_2 - T_a}{R_i} \right)^{1/4} \right)}_{\text{Convection, Inner Radial}} (T_a - T_2) + \underbrace{5.73\epsilon(S_{wall} + S_{cyl_o} + S_{cyl_i}) \left[ \left( \frac{T_a}{100} \right)^4 - \left( \frac{T_2}{100} \right)^4 \right]}_{\text{Radiation, Axial and Radial}} \quad (6.2)$$

$$S_{wall} = \pi(R_o^2 - R_i^2) \quad (6.3)$$

$$S_{cyl} = 2\pi RL \quad (6.4)$$

The heat relations shown in equations 6.1 and 6.2 could now be solved simultaneously to determine the steady-state temperature at nodes 1 and 2. Relations 6.1 and 6.2 were restructured to show the convective and radiative heat dissipation as functions. Then, both equations were rewritten to have a single temperature variable on the left-hand-side. This process is shown in equations 6.5 through 6.8.

$$0 = \underbrace{\frac{kS_{wall}}{n}(T_1 - T_2)}_{\text{Conduction, Axial}} + Cov(T_1, T_a, R_i, R_o, L) + Rad(T_1, T_a, R_i, R_o, L) + Q \quad (6.5)$$

$$0 = \underbrace{\frac{kS_{wall}}{n}(T_2 - T_1)}_{\text{Conduction, Axial}} + Cov(T_2, T_a, R_i, R_o, L) + Rad(T_2, T_a, R_i, R_o, L) \quad (6.6)$$

$$T_2 = T_1 - \frac{n}{kS_{wall}} (Cov(T_1, T_a, R_i, R_o, L) + Rad(T_1, T_a, R_i, R_o, L) + Q) \quad (6.7)$$

$$T_1 = T_2 - \frac{n}{kS_{wall}} (Cov(T_2, T_a, R_i, R_o, L) + Rad(T_2, T_a, R_i, R_o, L)) \quad (6.8)$$

The resulting functions shown in equation 6.7 and 6.8 were used to verify the optimization method in the thermal model. This was done by plotting both functions and indicating where the lines intersect. At the intersection point the temperature of both are the same, resulting in the two non-linear simultaneous equations shown to be solved. This intersection point should then correlate with the result of the model. The resulting plot is shown in figure 6.3.

In figure 6.3 it can be seen that the intersection of the two lines described by functions 6.7 and 6.8 intersect each other at the location the model predicted. This resulted in a final steady-state temperature of 24.76°C for section 1 and 24.30°C for section two. To further verify the model three situations were run and the results were compared with each other. These situations are given below:

1. Heat input of 100 W on node 1 and 0 W on node 2
2. Heat input of 0 W on node 1 and 100 W on node 2

### 3. Heat input of 0 W on node 1 and 0 W on node 2

The results for these three situations are shown in table 6.2. The situations number on the left of the table corresponds with those described above.

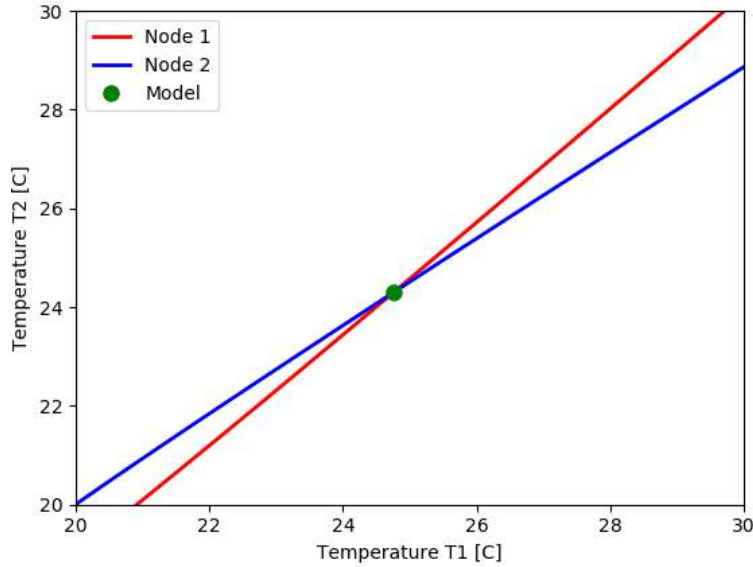


Figure 6.3: The change in temperature T2 as a function of T1 for nodes 1 and 2, the place where the two lines intersect matches the temperature calculated by the model

Table 6.2: The heat of the nodes used in solver verification under different input situations

Situation	Heat Input 1 [W]	Heat Input 2 [W]	Temperature 1 [°C]	Temperature 2 [°C]
1	100	0	24.76	24.30
2	0	100	24.30	24.76
3	0	0	20	20

Table 6.2 shows that the output temperatures changes depending on the situation. Looking at the results, it is clear that the simultaneous equation solver is verified. This is because situation 1 and 2 have mirrored output temperatures, this correlates with the input as the power going in the system remained constant, it was just applied at opposite points. Situation 3 also shows that if no power is put into the system the temperature of both nodes is the ambient temperature, which correlates with what is expected to happen.

### 6.1.2. Simple Geometry Verification

In this phase of the verification the steady-state temperature calculated by the thermodynamic model was compared the results calculated by a third party software. The engineering simulation software that was chosen is the thermodynamics package within ANSYS. Two simple geometries were verified to show relation between the results of both softwares. The first geometry, was a simple cylinder with one bearing, acting as a heat source in the center. The second geometry was also a cylinder but with additional rollers acting like flex-rollers on the inside of that larger geometry. The boundary conditions were the same for both models: The input heat power and location; the convection locations and convective film coefficient; and the types of materials and their thermal properties

#### Without Flex-Rollers

The first geometry that was verified is a simple cylinder with a single bearing acting like a heat source. The geometry used in this verification was identical to that shown in figure 5.15, all the geometric measurements and input variables are shown in table 5.1. These values were used as inputs in the created thermal model and in ANSYS. The result of both of these programs are shown in figure 6.4 and 6.5 respectively.

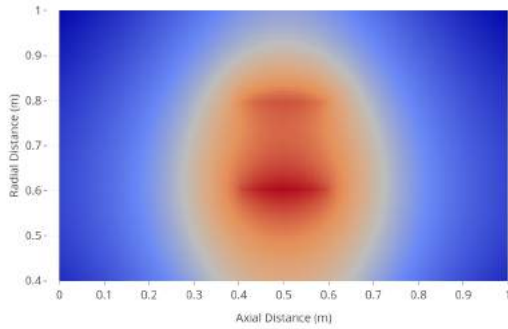


Figure 6.4: Heat-map generated by the thermal model

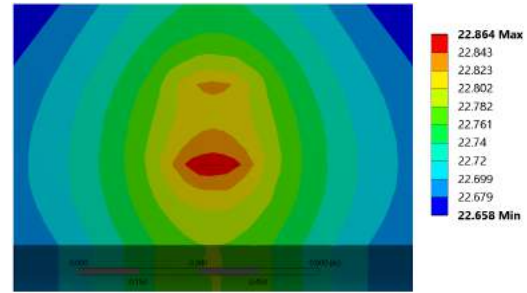


Figure 6.5: Heat-map generated by ANSYS

The two figures show that similar internal temperatures are achieved. They both show that the final steady-state temperature of the system is around 22.75 °C. Additionally, the heat distribution of both systems look similar. Both models show two heat points, those are the contact points of the bearing with the remaining structure. The hottest point, which is the bottom contact point of the bearing with the outer structure, is also identical for both models. They also show that the heat becomes less far away from those contact points. The effect of heat dissipation in a cylinder can also be seen in both models, as the top surface is colder compared to the bottom. The temperature distribution is nearly identical for both figures with a maximum of 22.86 °C and a minimum of 22.65 °C. The main difference between these two models is that the temperature gradient is smoother for the one generated by the thermal model. This difference has to do with the node size, the nodes of the thermal model were much smaller compared to the mesh used in ANSYS. Overall, this result indicates that the model was verified for simple cylindrical geometries, the next step was to make it more complex by adding flex-rollers to the verification process.

### With Flex-Rollers

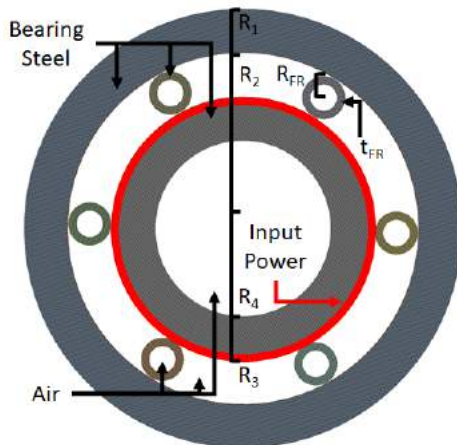


Figure 6.6: Illustration of geometry

Table 6.3: Input variables in roller verification

Variable	Description	Value	Unit
$R_1$	Outer Annulus Outer Radius	0.5	m
$R_2$	Outer Annulus Inner Radius	0.4	m
$R_3$	Inner Annulus Outer Radius	0.3	m
$R_4$	Inner Annulus Inner Radius	0.2	m
$R_{FR}$	Flex-Roller Radius	0.05	m
$t_{FR}$	Flex-Roller Thickness	0.01	m
$L$	Length of Annuli	0.3	m
$L_{FR}$	Length of Flex-Roller	0.2	m
$Q$	Input Power	200	W
$k$	Thermal Conductivity Steel	46	W/(m K)
$\epsilon$	Emissivity	0.79	-
$T_a$	Ambient Temperature	21	C°

The second geometry that was modeled for verification is one that contained flex-rollers similar to the drive used in the wind turbine. An illustration of the geometry is shown in figure 6.6, all the relevant variables for that geometry are shown in table 6.3. The geometry consists of two cylinders with a given length, with one enclosed inside the other. There is a gap in between the two cylinders, in this spacing additional smaller rollers were placed to act like flex-rollers. The material of all the cylinders (structure and rollers) is AISI 52100 bearing steel and the spacing between the rollers is air at ambient conditions. To visualize the heat propagation better throughout the model only one side of the roller contact point was generating heat. This contact point is also visualized in figure 6.6. The boundary conditions between the thermodynamic model and ANSYS were identical to each other.

In the ANSYS model the flex-rollers were stationary, therefore the air flow was not moving in circumferential direction. The thermodynamic model took this into consideration, by setting the velocity of the flow almost equal to zero. A rotational velocity of zero was not possible because the thermal model divides by the flow velocity to determine the Reynolds number of the flow as shown in equation 4.36, the Reynolds number is then used to calculate the convective heat transfer coefficient. The results of the ANSYS model from three different view points is shown in figures 6.7 , 6.8 and 6.10.

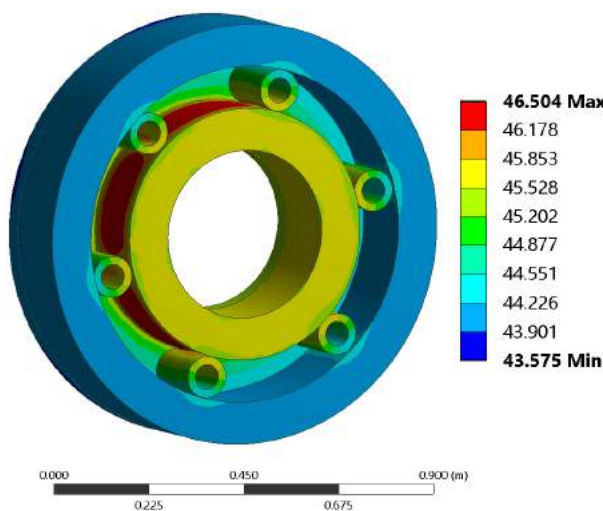


Figure 6.7: Temperature distribution 3D

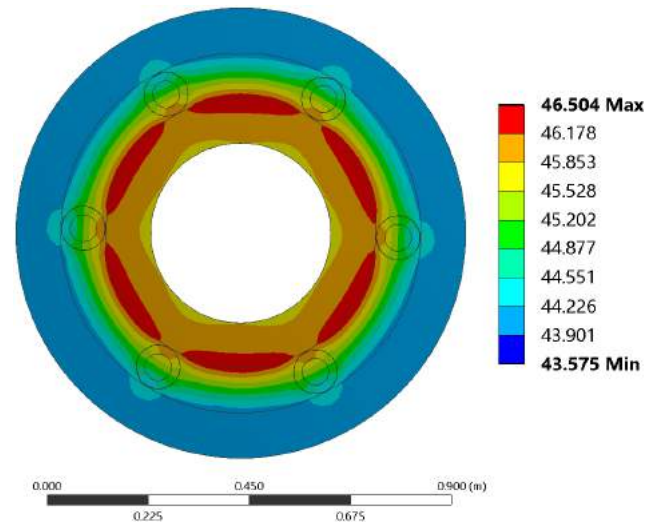


Figure 6.8: Temperature distribution 2D cut-out

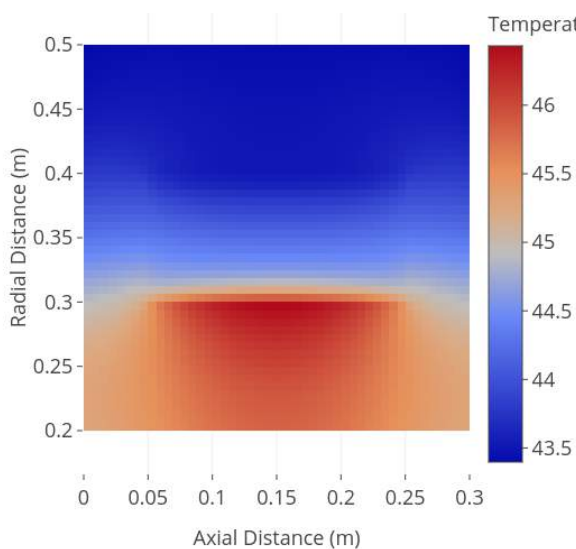


Figure 6.9: Temperature distribution thermal model

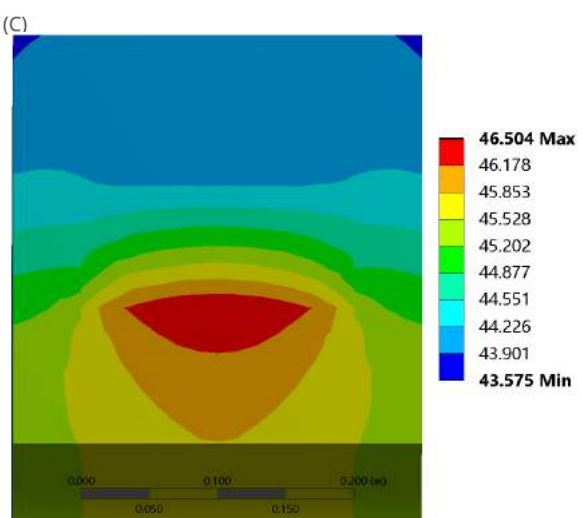


Figure 6.10: Temperature distribution ansys

The first two figures generated by ANSYS are a three dimensional view of the system, shown in figure 6.7, and a two dimensional cut-out, shown in figure 6.8. When looking at these two figures some conclusions were drawn about incorporating flex-rollers in the thermal model. The highest temperature in this system is 46.50°C and the lowest is 43.57°C. The location of the highest temperature is half-way between the flex-rollers around the outer circumference of the inner cylinder. At that location, the heat is generated and there is a boundary between air and steel. The heat dissipation through air is less compared to steel, resulting in a higher temperature at that location. Looking at that same edge and moving in circumferential direction towards the contact point of the inner cylinder with one of the flex-rollers, it can be seen that the temperature decreases. This is because the heat that is generated is propagated better through the steel flex-rollers as compared to air, dissi-

pating more heat from that contact point. This increased heat dissipation can also be seen by looking at the outer cylinder, where there are higher temperatures on the contact points with the flex-rollers. In the thermal model, during standard simulations, it was assumed that the flex-rollers are moving meaning that those peaks in temperatures will diminish and there will be a more constant temperature along the circumference. However, in this verification procedure the flow velocity in the flex-roller section is minimal, therefore the resulting temperature distribution should be less constant. The results of the thermal model can be compared with ANSYS by looking at figures 6.9 and 6.10.

The two figures show that both models result in similar internal temperatures. They both indicate that the steady-state temperatures ranges between 46.50°C and 43.57°C. Additionally, the heat distribution determined by both models look similar. The location of maximum and minimum temperature is at the same point in both models. The maximum temperature is at the middle contact point of the rollers with the bottom cylinder and the minimum temperatures are on the top left and right corners of the cross-section. The main difference, as with the previous geometry, is the smoothness of the temperature gradient between both models. This difference has to do with the different node size and shape between the models. Overall, it can be seen that the model can be verified for simple cylindrical geometries including flex-rollers, the next step is to validate the thermal model with an actual drive.

## 6.2. Validation

This section discusses the validation of the thermodynamic model. To validate the thermodynamic model a test was conducted on a smaller version of the transmission used in the DOT turbine. The steady-state temperature and power of this drive at multiple input speeds was measured and compared with the model. The test set-up will be discussed first, shown in section 6.2.1, followed by the testing procedure, explained in section 6.2.2. After that overview, the results of the test will be given in section 6.2.3. This validation section will conclude with a comparison between the model and the test results. Two parts of the model will be validated. These are the generated heat power of the system and the resulting steady-state temperature, these are discussed in sections 6.2.4 and 6.2.5 respectively.

### 6.2.1. The Test Set-Up

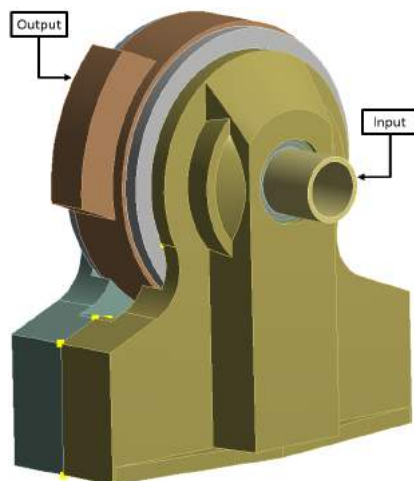


Figure 6.11: Transmission used for validation, input is through the center and output is around the exterior

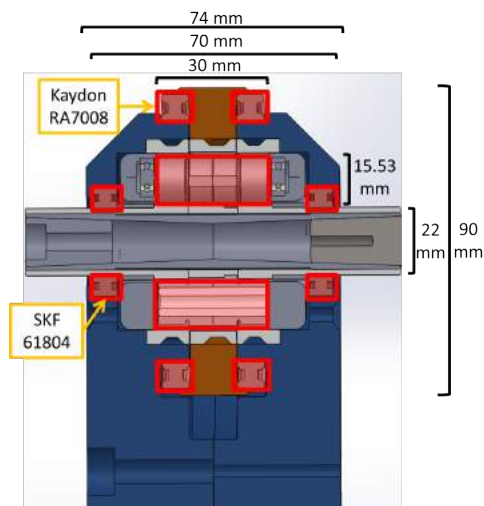


Figure 6.12: Dimensions of validation transmission with bearing locations

The validation tests was conducted on the drive shown in figure 6.11. The dimensions of this transmission is shown in figure 6.12 and the design requirements are shown in table 6.4. This gearbox has the same working principle as the one used in the DOT system. However in this validation test, the gearbox ran in reverse. The input was connected at the center of the drive and the output was at the outer annulus. Despite this, the relations used to model the thermal properties of both drives are the same. There is just a change in velocity

profile as the validation transmission is a speed reducer while the DOT drive is a speed increaser. The input and output locations are shown in figure 6.13 and the velocity profile is shown in figure 6.14.

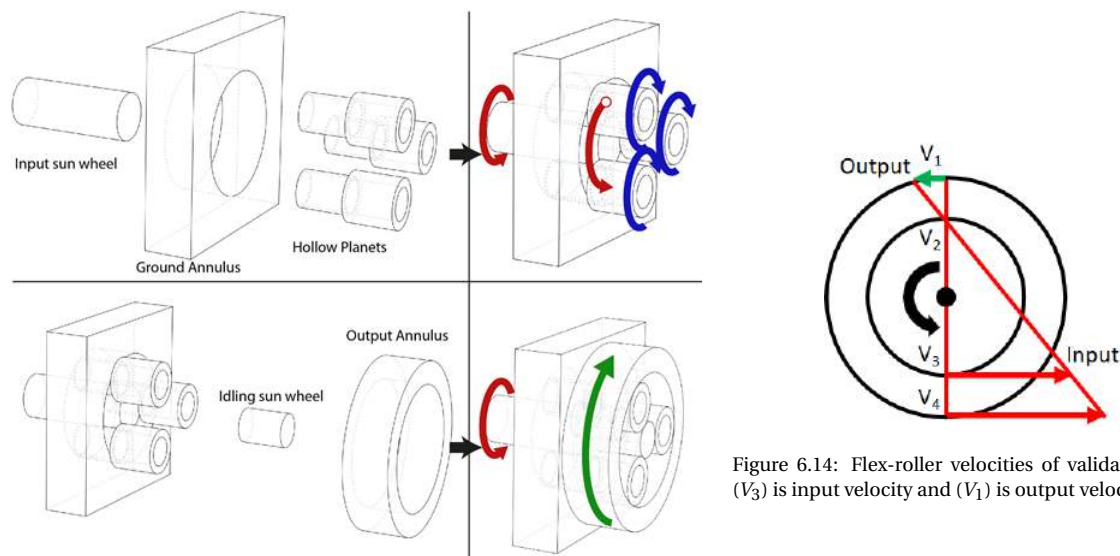


Figure 6.13: Working principle of validation drive, it is a speed reducer

Figure 6.14: Flex-roller velocities of validation drive, ( $V_3$ ) is input velocity and ( $V_1$ ) is output velocity

Figures 6.13 and 6.14 illustrate that velocity ( $V_3$ ) is the input velocity and ( $V_1$ ) is the output velocity. The validation drive is composed out of three annuli (two ground and one output), an input sun wheel and an idling wheel. The flex-rollers are also mirrored in this transmission, like the DOT drive. There were two types of bearings used in the design, the dimensions of these bearings are indicated in table 6.15. This drive is significantly smaller compared to the DOT system, allowing it to be tested in a controlled environment, where the boundary conditions were monitored.

Table 6.4: Design requirements

Requirement	Value	Unit
Input Torque	70	Nm
Gear Ratio	150:1	-
Flex-Roller Number	7	-
Design Friction Coefficient	0.15	-
Lubrication		
Viscosity 40°C	110	cSt
Viscosity 100°C	11	cSt

Figure 6.15: Bearing type and dimensions

Bearing	Dimension	Value
Kaydon RA7008	Outer Diameter	86 mm
	Inner Diameter	70 mm
	Thickness	8 mm
	Radial Force	50N
SKF 61804	Outer Diameter	32 mm
	Inner Diameter	20 mm
	Thickness	7 mm
	Radial Force	25N

The drive used for validation was placed in the test bench shown in figure 6.16. In this test-bench, an electric motor, located on the right in figure 6.16, powers the system allowing the input shaft to spin. The drive, connected at the other end of the input shaft, was allowed to rotate freely. The sensors located on the input shaft in between the motor and gearbox measured the torque and rotational velocity of the shaft. The values received from those sensors were used to calculate the power of the gearbox. These three components (motor, sensors and drive) in the test-bench were connected to a fixed base. This base kept all the components, except the input shaft and output annulus from rotating. The sensors were connected to a computer where an operating software (Simulink) was used to control the inputs and store the data.

Thermocouples, (as shown on the left of figure 6.16) were attached at multiple locations on the gearbox. These thermocouples allowed the tracking of heat throughout the transmission. Additionally, it gave an accurate picture of where the most heat was generated. The data received from these experiments was validated against the data generated from the model to determine if the model predicts the heat generation and

steady-state temperature properly. The thermocouples, as shown in figure 6.17, were placed at four locations to measure the internal and the external heat of the system. The internal thermocouples were placed within the ground annulus close to the location where the flex-roller makes contact with it. This was assumed to be one of the location of maximum heat. The ground annulus was chosen because it was not rotating during operation, allowing for easy placement of the thermocouples. The external thermocouples are placed on the exterior housing. This was to measure the heat propagation throughout the system. There were two sets of two thermocouples, placed on each side of the drive to determine if there was a difference in temperature between the opposite sides. Each thermocouple was assigned a number, the numbering can be seen in figure 6.17. The requirements for those thermocouples are shown below:

**Thermocouple Requirements:**

- Minimum length 10mm
- Maximum diameter 5mm (as small as possible is preferred)
- Operating temperature range 0-200 °C
- Sealed

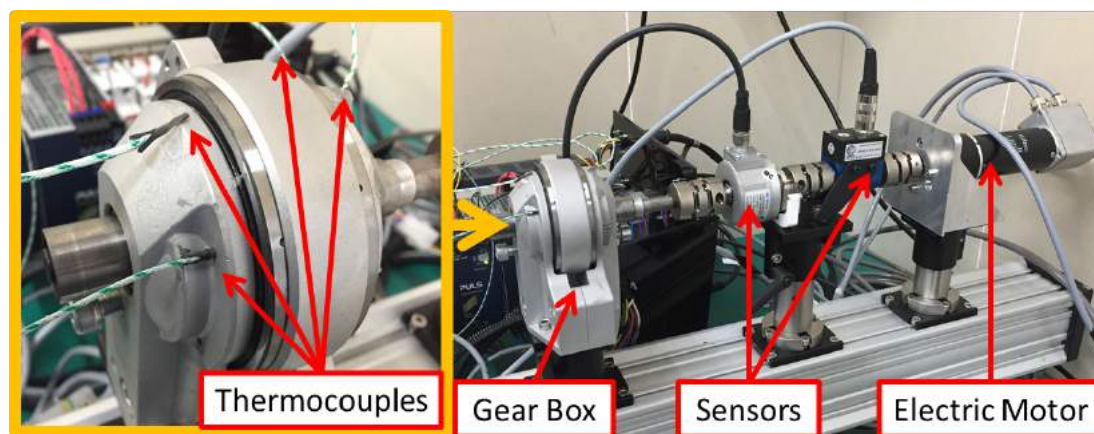


Figure 6.16: Validation test-bench, showing the thermocouples, gear box, sensors and electric motor

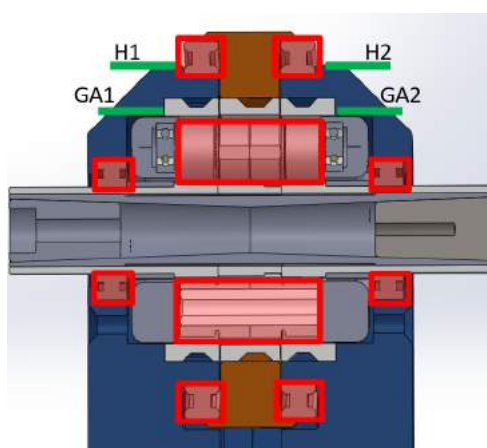


Figure 6.17: The thermocouple numbering

Table 6.5: Thermocouple location description

Number	Location	Reasoning
GA1	Left Ground Annulus	Heat generated by the Flex-Roller
GA2	Right Ground Annulus	Heat generated by the Flex-Roller
H1	Left External Housing	Heat dissipated throughout the system
H2	Right External Housing	Heat dissipated throughout the system

This test set-up was used to validate the model. Using this test-setup multiple test were conducted at different input rotational velocities to gather data. An overview of the procedures for those validation tests are given in section 6.2.2.

### 6.2.2. The Test Procedure

The test procedure for validation are described in this section. Three main test were conducted on the validation drive. These three tests were; (1) determining the maximum rotational velocity and temperature of the system , (2) measuring the steady-state temperature of the system without thermal insulation and (3) measuring the steady-state temperature of the system with thermal insulation.

The first test that was conducted was to determine the maximum achievable temperature and rotational velocity of the system as well as give the operating range. This was done by gradually increasing the input rotational velocity of the system and fixing it for a minimum of 30 minutes. This allowed the temperature to gradually increase. The input rotational velocity started at 500 rpm (52.4 rad/s) and was increased in steps of 100 rpm (10.5 rad/s). The rotational velocity was increased in those steps until the performance of the system, measured by the sensors, was not consistent. The maximum acceptable rotational velocity that was measured in this test was used as the upper bound of the following steady-state temperature tests.

The steady-state temperature of the system with no thermal insulation was measured second. This was done by setting the input rotational velocity at a constant value for multiple speeds, allowing the heat generated by the drive to stabilize towards steady-state condition. Three rotational velocity input conditions were used, these were 500 rpm (52.4 rad/s), 700 rpm (73.3 rad/s) and 900 rpm (94.25 rad/s). Each rotational velocity was fixed for a minimum of 60 minutes or until the drive achieved steady-state thermal condition. Additionally, the input torque and rotational velocity of the input shaft was measured continuously throughout the testing procedure, this was used to calculate the instantaneous power of the system.

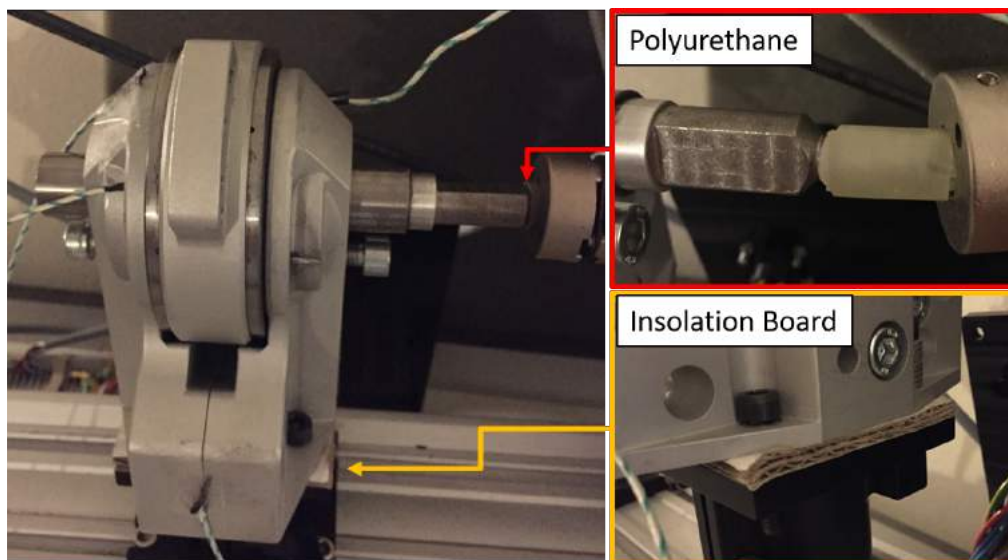


Figure 6.18: An overview of the modification to the test set-up

The final test was to determine the steady-state temperature of the system with thermal insulation. The thermal insulation used during this test can be seen in figure 6.18. On the input shaft of the drive, a polyurethane ring was used within the clamping structure that connects the drive's input shaft to the electric motor. This polyurethane has a conductive thermal coefficient 0.03 [ $W/(mK)$ ] compared to 46 [ $W/(mK)$ ] for the steel used. An insulating board was also used underneath the drive to reduce the conductive heat transfer to the test-bench base. The board had a lower conductive heat transfer coefficient compared to steel with a value of 0.3 [ $W/(mK)$ ]. These two modifications lowered the conductive heat transfer to the external environment via the input shaft and clamping structure. The same procedure was then conducted as the first test, by fixing the input rotational velocity at a constant value for multiple speeds, allowing the heat generated by the drive to stabilize towards steady-state condition. The rotational velocity inputs that were used are 400 rpm (41.9 rad/s) and 600 rpm (62.8 rad/s). The instantaneous rotational velocity and torque was also measured for this test in order to determine the power of the system. Using the three test procedure explained above, the data shown in section 6.2.3 was gathered. An explanation of that data will be given in that section.

### 6.2.3. The Results

The three tests explained in section 6.2.2 were conducted in order to validate the thermodynamic model. The first test was to determine the maximum operating temperature of the drive, the second was to determine the steady state temperature at multiple rotational speeds without thermal insulation and the third was to determine the steady steady-state temperature of the drive with thermal insulation. All three tests were conducted at an ambient temperature of 21°C and in an environment with minimal external convective air flow. The results for the first test are shown in figure 6.19, for the second test in figures 6.20 and 6.21, and for the third test in figures 6.22 and 6.23. The first test was conducted to determine the operating range of the transmission, using that range the input velocities for the second and third were determined.

#### Test 1: Maximum operating rotational velocity and temperature

The results of the first test are shown in figure 6.19. The test was conducted to see what the maximum rotational velocity of the drive will be. Using this velocity, the range of acceptable input speeds was determined. The plot indicates the change in measured variables as a function of time. The measured variables are the input velocity measured by the first sensor on the input shaft (in rad/s), the temperatures measured by the thermocouples (in °C) and the input torque measured by the second sensor on the input shaft (in cNm). An initial input rotational velocity was set at 500 rpm (52.4 rad/s) in the controller software on the computer, this speed was then increased in five steps of 100 rpm (10.5 rad/s). There is a slight difference between the input rotational speeds and the measured speeds shown in the plot. The difference comes from the accuracy of the electric motor powering the shaft using the input commands of the computer. The velocities on the plot in figure 6.19 were measured by a sensor, giving the actual rotational velocity, therefore these values will be taken during the validation comparison.

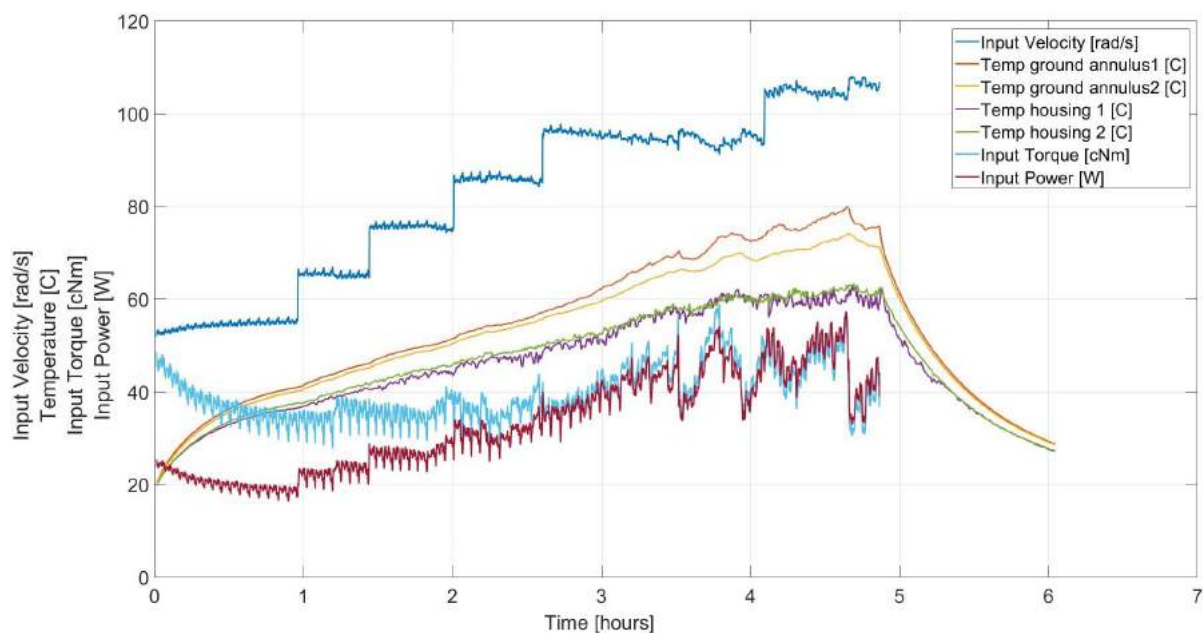


Figure 6.19: Maximum operating rotational velocity and temperature of the validation transmission, done to determine operating range, maximum achievable rotational velocity is 98  $rad/s$

Increasing in the velocity in multiple steps allowed the drive to heat up gradually until the maximum possible temperature was reached. This gradual rise made it possible to determine the maximum rotational speed with greater precision. It can be seen that the maximum plausible rotational velocity is 98  $rad/s$ , a rotational speed above that value resulted in inconsistent measurements. This inconsistency in the performance is contributed to there being additional slip in the system, caused by the normal force of the flex-rollers not being high enough to withstand the higher rotational velocities. The value of 98  $rad/s$  was then used as the upper bound velocity in the steady-state temperature tests.

## Test 2: Steady-state temperature without thermal insulation

The plot shown in figure 6.20 illustrates the change in temperature as a function of time based on the input rotational speed. The test is conducted for a period of six hours, in which a given constant input rotational speed was applied for a minimum time of one hour. Between each successive input rotational velocities a cooling period of a minimum of 30 minutes was applied. The input rotational speed is shown by the blue line. As can be seen there are three steps in the input rotational speed, these relate with the inputs described in section 6.2.2. Due to the change of friction in the drive between start-up and operational condition, the input rotational velocity increases slightly at the beginning and stabilizes at the end of the operation. This stabilization is further aided by the controller system used to operate the electric motor which is adjusting to that change in friction. Based on the input velocity a clear relation can be made with the steady-state temperature of the gearing system.

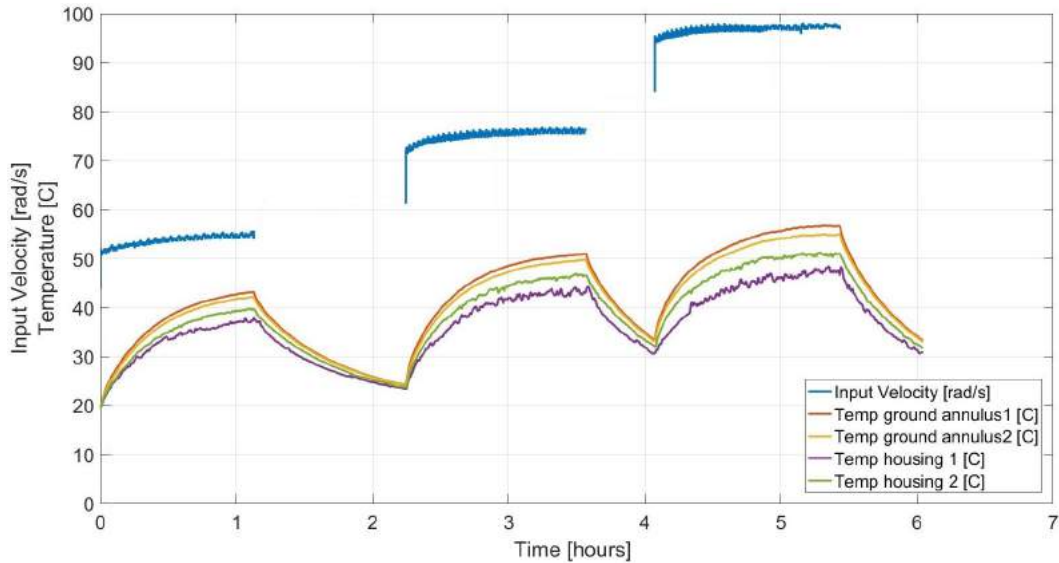


Figure 6.20: Steady-state temperature at three rotational velocities without thermal insulation, ground annulus temperatures are: 44°C at 55 rad/s, 52°C at 76 rad/s and 58°C at 98 rad/s

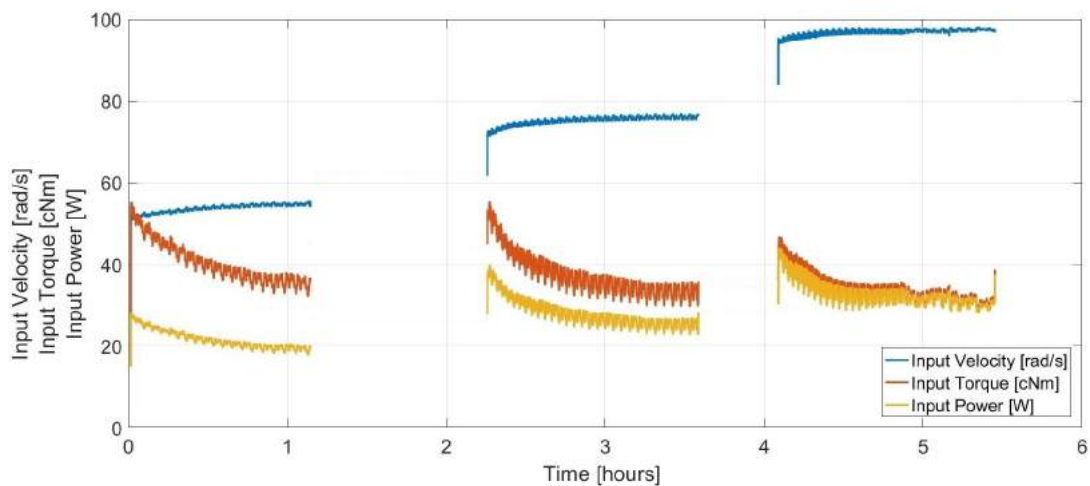


Figure 6.21: Torque and power at three rotational velocities without thermal insulation, power values are: 18.8 W at 55 rad/s, 24.9 W at 76 rad/s and 32.1 W at 98 rad/s

The first conclusion that can be made is that an increase in input rotational velocity results in a increased steady-state temperature, with the input velocities of 55, 76 and 98 rad/s resulting in the steady state temperatures of 44°C, 52°C and 58°C respectively. The measured rotational velocities vary slightly from the input

velocities given in section 6.2.2. This difference comes from the accuracy of the input electric motor with respect to controlling system's input. Looking at the temperature rise under a fixed rotational velocity at the start of the test, the gradient of the temperature lines are large. This gradient then decreases in an exponential manner until it reaches an asymptote, this asymptote is taken as the steady-state temperature. Looking at the individual thermocouples it can be seen that those positioned inside of the drive have a higher temperature than those on the outside. This is because it is closer to the major heat source, the flex-rollers. It can also be seen that the external thermocouple temperature readings are less stable than that of the interior ones, this is due to the external environment properties. Once the velocity of the input has been set to zero the drive's temperature cools down to ambient temperature. It starts with a sharp gradient at first and then the gradient moves towards zero the closer the temperature reaches ambient temperature.

The plot in figure 6.21 shows the torque, rotational speed and power as a function of time. The input torque and rotational velocities were measured using the sensor shown in figure 6.16. The input power of the system was then calculated by multiplying these two variables. When looking at figure 6.21 it can be seen that the input power increases as the rotational velocity increases. This increase has largely to do with the increase in rotational velocity as the input torque relatively remains the same. At a given rotational velocity it is noticeable that the initial input torque is high, however this torque decreases as the drive continues to run. This change in input torque is due to the friction changes in the system during start-up and operation. The power values used in the model validation process are those at the end of a measurement cycle for each input speed. These values are 18.8, 24.9 and 32.1 W. The output is running free, therefore it is assumed that all the power being put into the system is converted into heat.

### Test 3: Steady-state temperature with thermal insulation

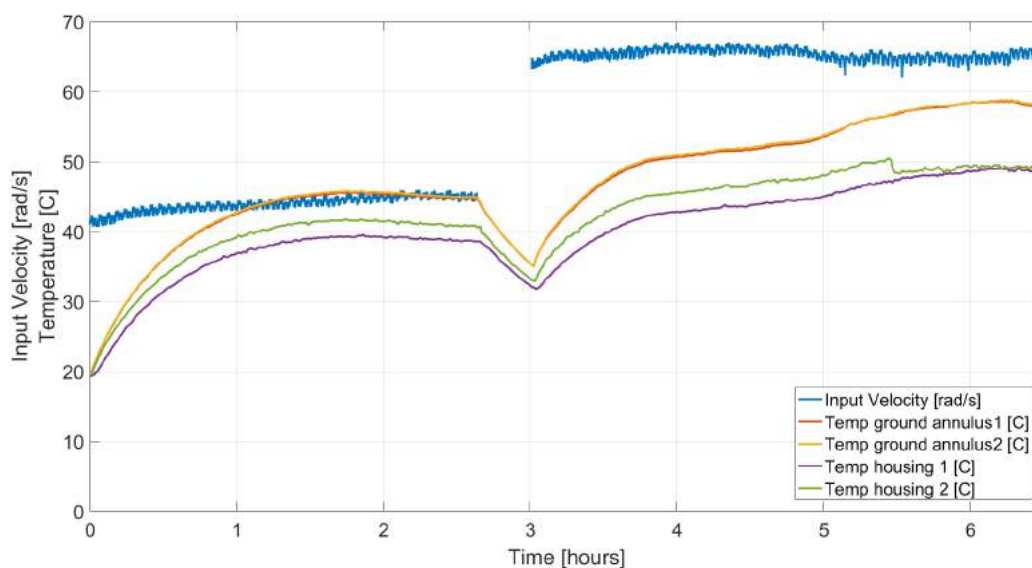


Figure 6.22: Steady-state temperature at two rotational velocities with thermal insulation, ground annulus temperatures are: 45°C at 45 rad/s, 53°C at 65 rad/s

The plot shown in figure 6.22 illustrates the change in temperature as a function of time based on the input rotational speed, for the thermal insulated test set-up. The test is conducted for a period of six hours, in which a given constant input rotational speed was applied for a minimum time of two and a half hours. Between each successive input rotational velocities a cooling period of a minimum of 30 minutes was applied, where the drive would be allowed to cool. The input rotational speed is shown by the blue line, there are two steps in the input rotational speed, given in radians per second. The slight change in rotational speed over time is caused by the same effect explained in test two. Figure 6.22 shows that two steady-state temperatures were reached. These temperatures were measured at a rotational speed of 45 and 65 rad/s. The first steady-state temperature value for the ground annulus, shown by the first asymptote, is 45°C. The drive reaches this temperature after around two hours of operation. The second steady-state temperature was more difficult to determine,

because after around five hours of operation the drive started to fail. Drive failure occurred because the carrier used to align the flex-rollers within the system started to crack, resulting in miss-aligned flex-rollers, increasing friction and increasing temperature. The failure point is visualized in figure 6.22 by the sudden bump in temperature. Taking this into consideration, the steady-state temperature at an input rotational speed of 65 radians per second is determined using the asymptote before drive failure. This resulted in a temperature of 53°C. When comparing the temperatures in this test to that of test two shown in figure 6.21, it can be seen that the same steady-state temperature can be reached with a lower input rotational speed.

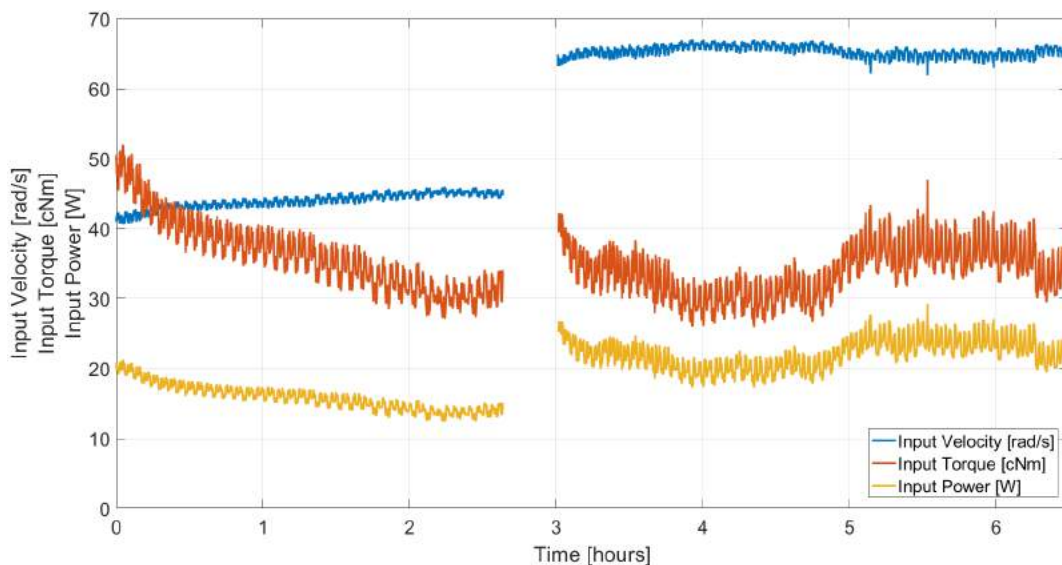


Figure 6.23: Torque and power at two rotational velocities with thermal insulation, power values are: 14.7 W at 45 rad/s, 21.5 W at 65 rad/s

The plot shown in figure 6.23 shows the torque, rotational speed and power in the third test. Like the previous tests the input power increases as the rotational velocity increases. The drive failure can also be seen in this plot at around five hours of operational time. During this point the torque required to operate the drive increases, meaning that more power is required to achieve the same rotational speeds. The two power values used in the model validation will take the power values before that point, these are 14.7 and 21.5 W.

#### 6.2.4. Heat Power Validation

The heat power generated by the drive that the thermodynamic model calculates needs to be validated with the results shown in section 6.2.3. In order for the model to calculate the heat power some initial conditions and constants needed to be implemented. Figure 6.12 indicates that there are two sets of two bearings (four bearings in total) in addition to the seven flex-rollers. The heat generated by these components all need to be calculated. The method on how to calculate the heat generated by one of the bearings is shown in section 4.1.4. The other three bearings are calculated using the same steps shown in that section. The heat power generated by the bearings were calculated for each rotational speed measured in the test. The resulting heat power of the bearings for each rotational velocity is shown in table 6.6. The lubrication viscosity used in the model for each input rotational velocity is also indicated. These values were determined using a quadratic relationship between the two viscosity values given in table 6.4 and the final steady-state temperature of the system measured during the test at the different speeds. The model in combination with the test results shown in figures 6.21 and 6.23 indicates that the total heat power generated by the bearings is small compared to the flex-rollers, with less than 2% of the heat coming from the bearings.

The flex-rollers are largely responsible for the heat in the system. To calculate the heat power in the flex-roller section the steps in section 4.1.3 were followed. The transmission ran dry, therefore the relations to determine the different components of the friction moment ( $M_1$ ) and ( $M_v$ ) cannot be used. This is because the rolling elements (flex-roller) makes direct contact with the race-way (annulus) and does not have a lubrication film in between these two elements, not meeting one of the requirements in order to use the relations. Therefore only equations 4.1 and 4.2 can be used. All variables are known except the rolling coefficient of fric-

tion in the flex-roller section ( $\mu_{FR}$ ). In order to determine that variable one of the test result points was used. The relation to calculate the rolling coefficient of friction in the flex-roller section ( $\mu_{FR}$ ) is shown in equation 6.10, this relation combines equation 4.1 and 4.2. To determine ( $\mu_{FR}$ ), the radial force that the flex-roller exerts on the annulus ( $F_t$ ) was determined first, this was done by using equation 4.11 and the design requirements given in table 6.4, the calculation is shown in relation 6.9.

Table 6.6: The thermal model's input lubrication viscosity and calculated total heat power of the bearings within the validation drive per input rotational velocity

	45 [rad/s]	55 [rad/s]	65 [rad/s]	76 [rad/s]	98 [rad/s]
Viscosity [cSt]	82	86	56	59	48
Power [W]	0.16	0.23	0.24	0.30	0.5

$$F_t = \frac{M}{ZR_{in}\mu} = \frac{70}{7(0.011)0.15} = 6060.6N \quad (6.9)$$

$$\mu_{FR} = \frac{\kappa_Q(Q_{tot} - Q_b)}{1.047 * 10^{-4} n F_t d / 2} = \frac{0.329(14.7 - 0.18)}{1.047 * 10^{-4} (429.7) 6060.6 (22/2)} = 0.0016 \quad (6.10)$$

The variables are, ( $\kappa_Q$ ) the heat power ratio between the inner and outer section of the flex-roller, ( $Q_{tot}$ ) the total measured input power shown in figure 6.23, ( $Q_b$ ) the power of the bearings shown in table 6.6, ( $n$ ) the input rotational velocity in rpm, ( $F_t$ ) the normal force per flex-roller calculated in equation 6.9 and ( $d$ ) the bore diameter of the flex-roller section in mm, shown in figure 6.12. Relation 6.10 was used to calculate the rolling friction coefficient at 45 rad/s (429.7 rpm), figure 6.23 shows that the total measured power was 14.7 W. Using those input variables the resulting rolling friction coefficient of the flex-roller is 0.0016. This values falls in between the rolling friction coefficient of a average lubricated caged cylindrical roller bearing (0.0013) and a full-complement roller bearing (0.002).[16] These two different bearing types are illustrated in figure 6.24.

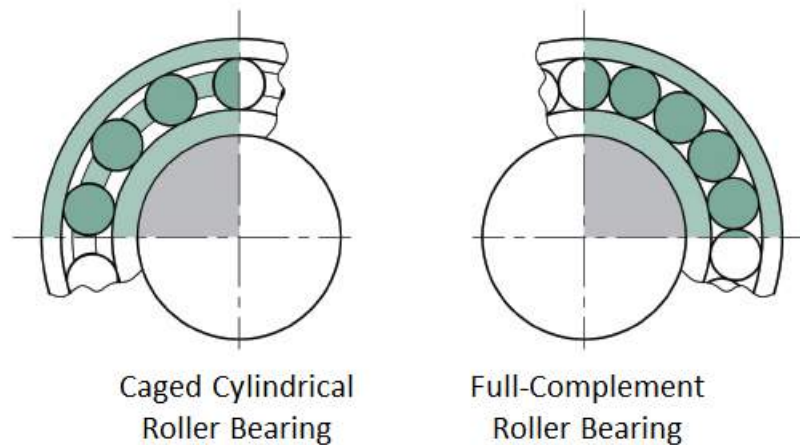


Figure 6.24: Illustration of a caged cylindrical roller bearing (left) and a full-complement roller bearing (right)[56]

Caged cylindrical roller bearings use a cage (also know as a carrier) to equally space the bearing's rollers around the circumference. This cage is made out of a low dynamic friction coefficient material and forms around the rollers to keep them a fixed distance from each other. During operation there is frictional contact between the cage and the rollers as the two components slip over each other. However, the amount of friction is greatly reduced once lubrication is used. Full-complement bearings do not use a cage but rather fill all the available space around the circumference with additional rollers. This means that during operation the rollers continuously slip over each other, increasing the friction compared to standard caged bearings. Additionally, at the slip location the rollers are rotating in opposite directions increasing the friction further.

The rolling friction coefficient ( $\mu_{FR}$ ) is dependent on the amount and type of guiding features, the amount and interaction of the flex-rollers and the overall geometry of the rolling surface. The rolling and sliding friction moments, explained in section 4.1.1, are responsible for that value in the unlubricated validation transmission. The drive uses a custom cage meant for the flex-rollers, an illustration of the cage is shown in figure 6.25. The cage forms around the flex-rollers and uses a shaft that goes through the center of it. This shaft is then coupled with smaller bearings which makes contact with the inner wall of the flex-rollers, keeping the flex-rollers straight while they move around the drive. The bearings rotate with the flex-rollers, resulting in minimum friction on the contact surface between the cage bearings and the inside of the flex-rollers.

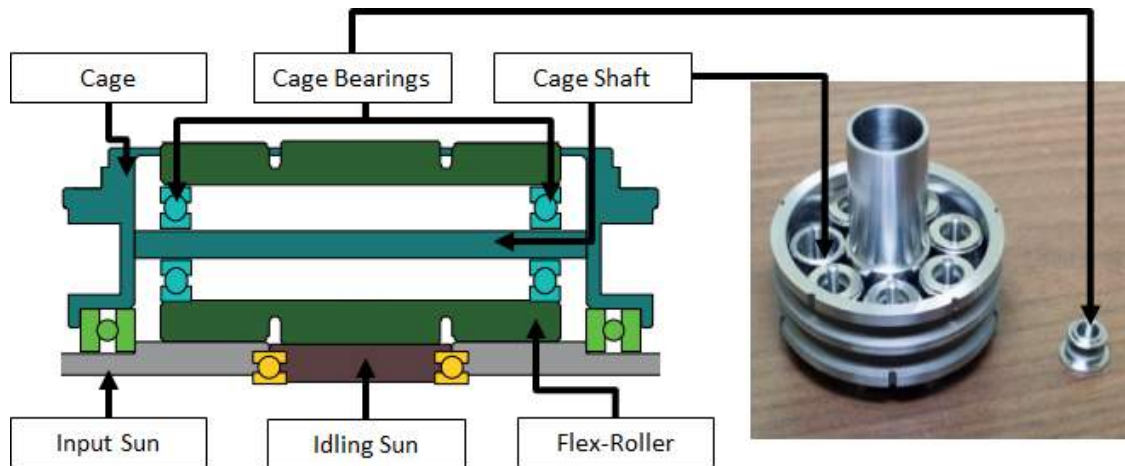


Figure 6.25: Illustration of cage in validation transmission with location of components

Comparing the transmission to standard bearings it was deduced that the drive acts more like a caged cylindrical roller bearing as compared to a full-complement bearing. This is because the flex-rollers do not make contact with each other, reducing the overall friction. However, the friction coefficient of the validation transmission, calculated using the test results, has a larger rolling friction coefficient than standard caged cylindrical roller bearings. This difference comes from the system being unlubricated, which amplifies the heat generated by the effects explained in section 4.1.1, due to an increase in local dynamic friction coefficient of the materials that are in contact with each other. Once lubricated, the frictional properties in the flex-roller section of the validation transmission should resemble that of a heavy series caged cylindrical roller bearing.

To validate the model the value of ( $\mu_{FR}$ ) calculated in equation 6.10 was used as input to determine the generated heat power for all the tested input rotational velocities. The thermal model's calculated heat power was then compared with the measured input power gathered during the test procedure described in section 6.2.3. The results are indicated in table 6.7 and are plotted in figure 6.26. The plot also illustrates the heat power of the system if the flex-rollers had the same friction coefficient as full-complement or caged cylindrical roller bearings.

Table 6.7 indicates that the results of the model closely match that of the measured values. Four out of the five measurement points have less than a 1% difference between the two values. The biggest difference between the modeled and the measured power is for a rotational velocity of 55 rad/s where the difference is 4%. This difference could come from the transmission not being worked-in fully as it was the first point that was measured. It can also be seen that the measured power falls in between the bounds set by the friction coefficient of the two bearings illustrated in figure 6.24. Using the results of this analysis it can be concluded that a friction coefficient of 0.0016 can be used to model the heat power of the unlubricated transmission. In order to determine if that ( $\mu_{FR}$ ) value can be used as the general value for all the transmissions based on this novel concept, more tests will need to be conducted. If this friction coefficient changes the final steady-state temperature will be altered. The effects of this are explained further in section 6.2.6. To analyze the full-scale model used in the DOT wind-turbine for the unlubricated condition, the ( $\mu_{FR}$ ) value which best describes this validation drive was used, which is 0.0016.

Table 6.7: Comparing heat power values calculated by the thermal model with the measured values

Input Rotational Velocity [rad/s]	Measured Power [W]	Calculated Power [W]
45	14.7	14.7
55	18.8	18.1
65	21.5	21.4
76	24.9	25.0
98	32.1	32.3

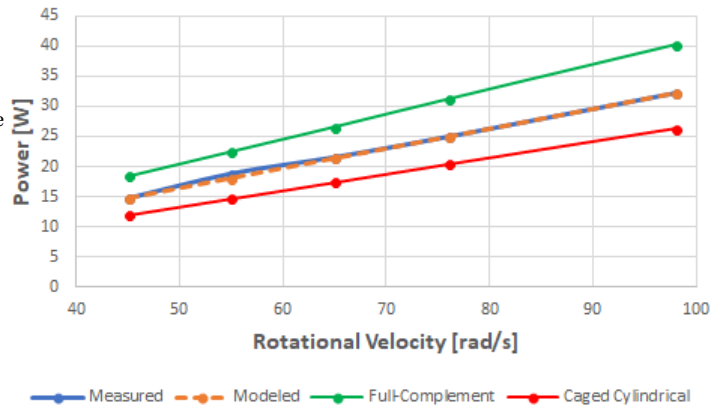


Figure 6.26: Plot indicating power as a function of rotational velocity, comparing calculated power by the thermal model with measured power, maximum difference 4% at 55 rad/s

If lubrication is used in the system, the torques ( $M_1$ ) and ( $M_v$ ) explained in section 4.1.2 can be calculated. These two torques are dependent on the factors ( $f_1$ ) and ( $f_o$ ) respectively. Since it was deduced that the flex-roller section resembles a heavy series cylindrical roller bearing an ( $f_1$ ) value ranging from 0.0002 to 0.0004 can be used to calculate the torque due to an applied load factor ( $M_1$ ), as indicated in figure A.4 of the appendix. The factor ( $f_o$ ) used to calculate the viscous friction torque ( $M_v$ ) has a range of possible values, as it is depended on the type of lubrication used. A chart showing this factor is given in figure A.1 of the appendix. In the model of the DOT system, multiple lubricants were analyzed therefore different factor were taken into consideration. To determine the combination of possible factors the same approach was made as for ( $f_1$ ).

### 6.2.5. Steady-State Temperature Validation

The next validation procedure was to determine if the steady-state temperatures measured at the points shown in figure 6.17, in the tests relates with that of the thermal model. The multiple input rotational speeds measured during the tests (these are 45, 55, 65, 76 and 98 rad/s) were inserted in the model to see if the resulting temperatures that the model calculated related with that of the tests. As explained in section 6.2.4 a flex-roller section friction coefficient ( $\mu_{FR}$ ) of 0.0016 was used to calculate the heat power. The geometry used as input in the thermal model is shown in figure 6.27.

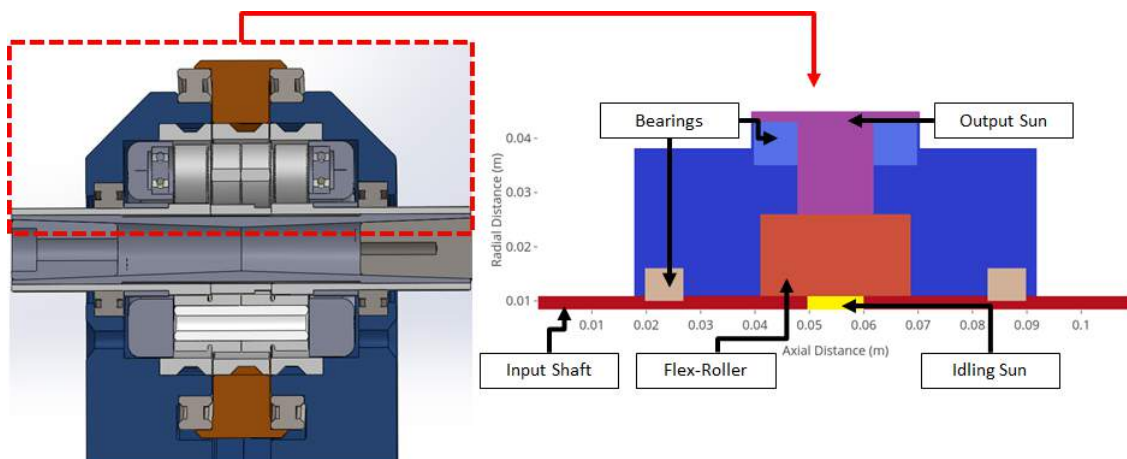


Figure 6.27: Input geometry used in thermodynamic model for validation transmission, showing all components

The figure shows that the model has the same general form as the transmission used for validation. The locations and dimensions of all main components are the same between the two. The only difference in geometry between the model and the actual drive is on the top corners of the model. The thermodynamic model can only create shapes with straight edges, resulting in the sloped housing not being modeled. This change in geometry should have a minimal impact on the final steady-state temperature of the drive, as it is just a slight

variation in external surface area. All the main components that contribute to heat generation and dissipation are also indicated in figure 6.27. Using this geometry as input, the thermodynamic model calculated the steady-state temperatures for the five input rotational velocities indicated in section 6.2.3. The resulting heat-map for an input velocity of 45 rad/s is shown in figure 6.28.

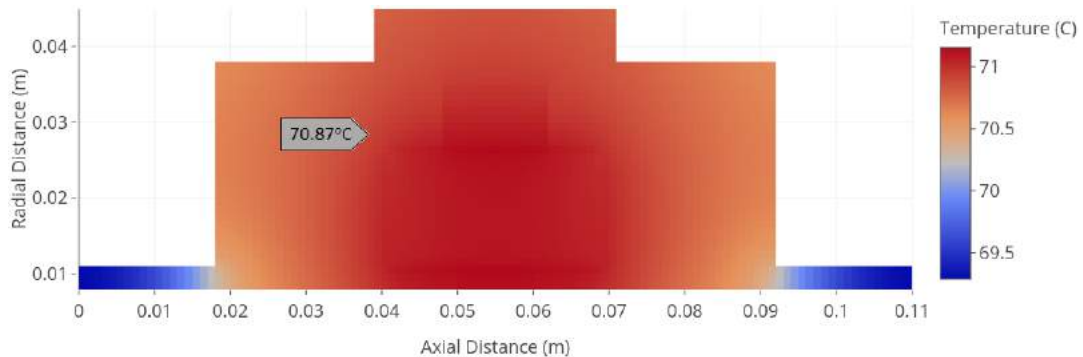


Figure 6.28: Modeled steady-state temperature of validation transmission at input speed of 45 rad/s, calculated ground annulus temperature is 70.87°C

The heat-map in figure 6.28 shows that the steady-state temperature within the drive should vary between 68°C and 71.5°C. The coldest location is on the input shaft the furthest away from the drive and the hottest location is the contact point of the flex-roller with the remaining structure. The figure also shows that the temperature of the output and idling wheels are slightly higher as compared to the rest of the system. This is because the contact velocity of the flex-roller at that point is slightly higher than at the other locations, as shown by the difference in the velocities ( $V_1$ ,  $V_2$ ,  $V_3$  and  $V_4$ ) in figure 4.8. This faster velocity results in more rolling friction, increasing the heat power. Since the output annulus is only in contact with the remaining structure through the bearings, there is an air gap in-between it and the other annuli. That results in less of its additional heat being dissipated, increasing its steady-state temperature compared to the other rings.

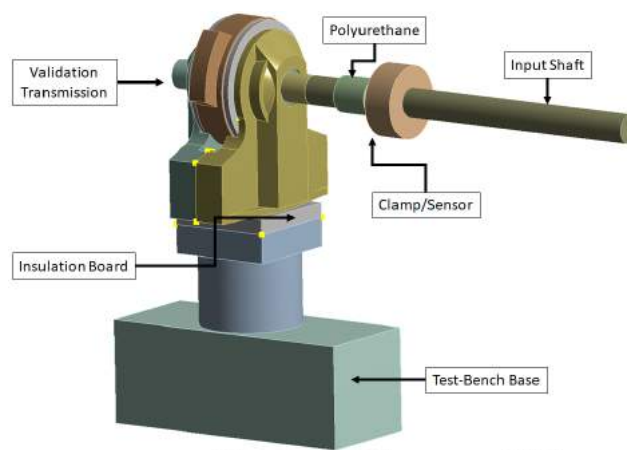


Figure 6.29: Illustration of test-bench simulation used in ANSYS, indicating all components that were modeled

There is a clear difference when comparing the steady-state temperatures calculated in the thermodynamic model to those measured in the validation test. The tests measured a ground annulus temperature of 45°C at an input speed of 45 rad/s, while the model calculated a value of 70.87°C, that is a difference of 25.87°C. This difference is because the model assumes only convective heat transfer and radiation with the external environment, while in the test-bench, conduction through the base must also be taken into consideration. That additional conduction increases the overall heat transfer greatly. To show this effect an ANSYS simulation was made, with the drive attached to the test-bench base, an illustration of the set-up is visualized in figure 6.29.

The dimensions of the test-bench simulation were meant to match that of the actual test shown in figure 6.16. A steel shaft with a clamping mechanism and a cylindrical structure similar to one of the sensors, was attached to the input of the drive. Additionally, an aluminum/plastic stand that the drive was fixed to with a section of the test-bench base was added. The two thermal insulation materials, shown in figure 6.18 were also included to accurately model the two steady-state temperature tests (test three in section 6.2.3). The ANSYS simulation was then run in combination with the thermal model to determine if the same temperatures measured in the validation tests could be determined. The input power of the flex-rollers and the bearings at a given rotational velocity was calculated by the thermal model and inserted on the correct surfaces in the ANSYS simulation. Using those values the steady-state temperature of the complete system in the test-bench was determined. The resulting steady-state temperatures for an input speed of 45 rad/s with thermal insulation and an input speed of 55 rad/s with no thermal insulation are shown in figures 6.30 and 6.31 respectively.

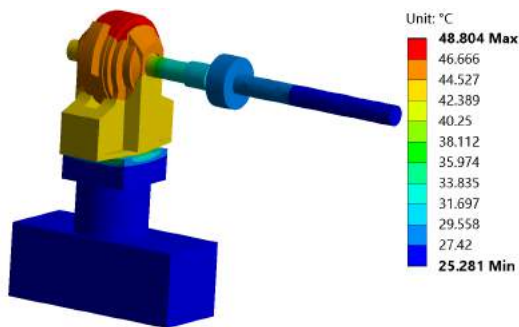


Figure 6.30: Steady-state temperature at 45 rad/s with thermal insulation, average ground annulus temperature 46.6

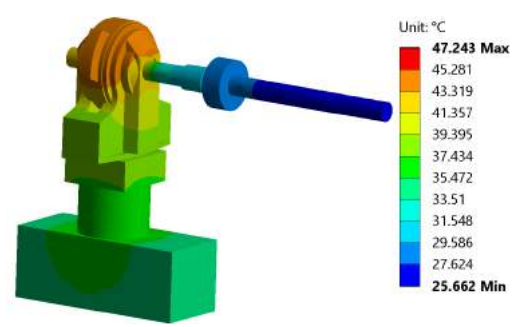


Figure 6.31: Steady-state temperature at 55 rad/s without thermal insulation, average ground annulus temperature 45.2

Looking at both of the figures its visible that adding additional thermal insulation affects the final steady-state temperature greatly. Both simulations result in approximately the same temperatures, however the input speed of figure 6.30 is 10 rad/s less. Adding thermal insulation, as shown in figure 6.30, causes less heat to be transferred by conduction to the base of the test-bench, increasing the temperature of the tested transmission. These results are also validated with the temperatures of the ground annulus measured in the tests shown in section 6.2.3. In those results, the final steady-state temperature of the ground annulus for the two test were 45°C and 44°C at an input speeds of 45 and 55 rad/s. The ANSYS simulations gives a value of 46.6°C and 45.2°C, a maximum difference of 3.5%. However, the temperatures measured on the housing of the drive do not match that of the ANSYS simulation. The validation tests measured a housing temperature for the two input rotation speeds of 40°C and 38°C compared to simulation's 44.5°C and 43.3°C. The difference in these values came from the coupling of the sensors onto the housing during the test procedure. The sensors were placed on the housing and were not completely covered by the housing's material. Resulting in them partially measuring the external air around the housing, visualized by the fluctuation in temperature in figures 6.20 and 6.22. Since this difference in the housing temperature comes from the fluctuation of the external flow during the test procedure, it not an accurate representation of the temperatures in the housing. Therefore, only the ground annulus temperature was used further in the validation the model.

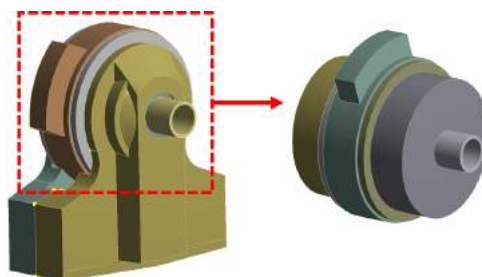


Figure 6.32: Modified validation transmission housing used in the ANSYS simulation

Despite the attempt to reduce conduction to the test-bench by using thermal insulation, not all the conductive heat transfer could be removed, resulting in the large difference between the thermodynamic model at the validation tests. To correctly validate the thermodynamic model the conductive heat transfer to the environment needed to be largely removed. An additional ANSYS simulation was used in combination with the validation test results to compare the thermal model's calculated temperatures with the measured values. In this simulation a modified version of the validation transmission, shown in figure 6.32, was used.

This modified version of the drive removed the additional housings and attachments, not taking into consideration in the thermodynamic model. Therefore, only convective heat transfer and radiation could be used to model heat dissipation to the environment. The different heat powers at the five rotational speeds, shown in section 6.2.4, calculated by the thermal model were inserted in this modified transmission and in the test-bench simulation shown in figure 6.29. The resulting steady-state temperatures from both of these simulations were then compared with the thermal model and the validation test results. The results of this analysis are shown on the plot in figure 6.33.

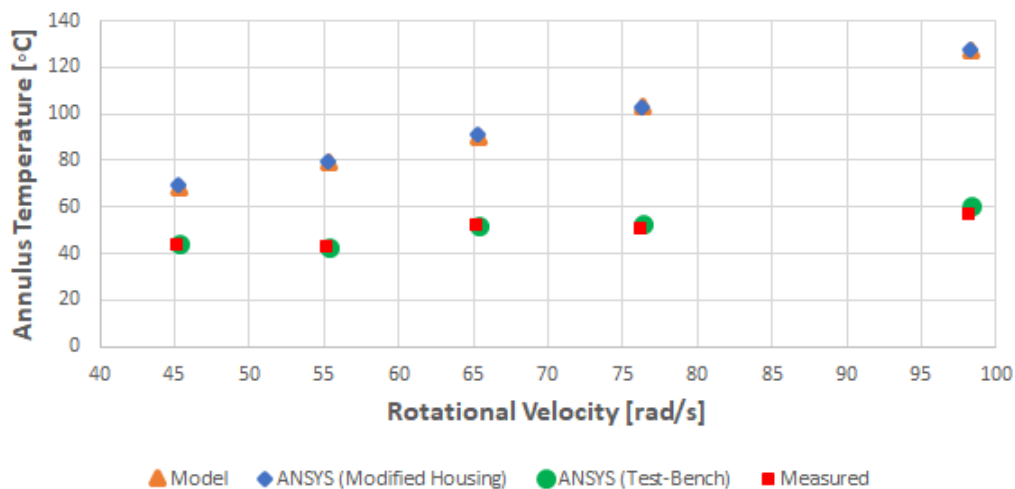


Figure 6.33: Steady-state temperature as a function of input rotational velocity for validation transmission, comparing the thermal model to the ANSYS simulation of the modified housing and the measured points to the ANSYS simulation of the test bench

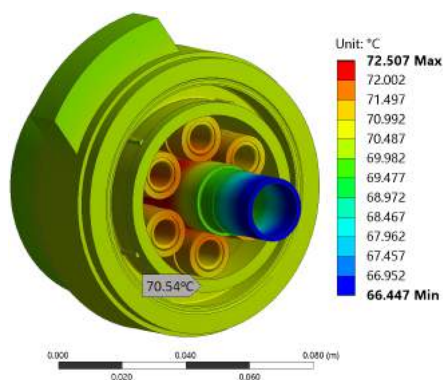


Figure 6.34: The 3D results from the ANSYS simulation of the validation transmission at a rotational speed of 45 rad/s

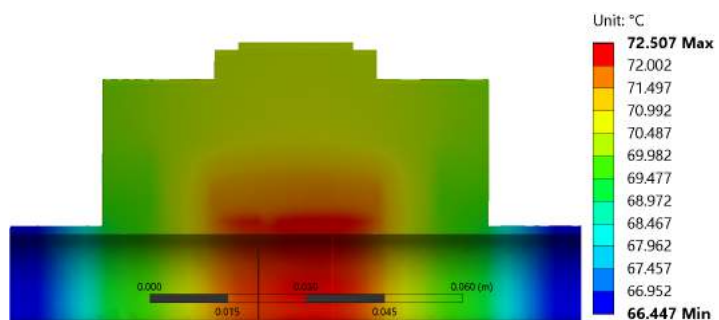


Figure 6.35: The 2D section plane results from the ANSYS simulation of the validation transmission at a rotational speed of 45 rad/s

The plot in figure 6.33 shows five input rotational speeds, each speed has four data points. The first point is the steady-state temperature of the ground annulus calculated by the thermal model, the second is the temperature calculated by the modified ANSYS model (figure 6.32), the third temperature was determined by the ANSYS simulation of the test-bench (figure 6.29) and the fourth was the temperature measured during the validation test. Firstly, this plot indicates that the thermodynamic model relates with the ANSYS simulation of the modified transmission, shown in figure 6.32. The measured temperature of the ground annulus for both

models are similar to each other. At an input velocity of 45 rad/s, the thermodynamic model calculated a temperature on the ground annulus of 70.87°C and the ANSYS analysis resulted in a temperature of 70.54°C, both locations are shown on figures 6.28 and 6.34. This close resemblance in ground annulus temperature between the two modeling methods for the multiple input speeds is shown in the plot in figure 6.33. The temperature values calculated by the "Model" are never more than 1% different than those determined with the "ANSYS (Modified Housing)" simulation. The biggest difference between these two modeling methods is the temperature spread, for an input speed of 45 rad/s the thermodynamic model varies from 68°C to 71.5°C while ANSYS is from 66.4°C to 72.5°C. This is because the model takes the motion of the flex-rollers into consideration within the modeling process, as explained in section 5.1.2. Therefore the convective heat transfer in the flex-roller section in the thermodynamic model is higher than compared to ANSYS. The increase in convective heat transfer within the flex-roller section result in a more uniform temperature gradient as heat dissipation within the structure is increased.

When comparing the ANSYS simulation for the test-bench with the test results of the validation transmission it can also be seen that they relate with each other. At lower input velocities the final steady-state temperature of the ground annulus in both cases differ from each other by just 3.5%. However, at higher input velocities the temperatures start to deviate from each other. At an input rotational velocity of 98 rad/s the "ANSYS (Test-Bench)" calculates a temperature of 63.2°C while the validation tests measure a temperature of 58°C. This difference could be due to the fact that the simulation test-bench does not completely match the actual test-bench. The simulation test-bench created for ANSYS shown in figure 6.29 is only part of the complete set-up, resulting in less surface area to dissipate heat compared to the actual situation. This effect becomes greater the warmer the drive becomes.

In conclusion, the final steady-state temperature is largely dependent on the boundary conditions of the system. The model assumes only convection and radiation to the external environment, therefore it was difficult to validate with a test, without first removing all forms of conduction to the external environment. Using ANSYS simulations in combination with the validation test results it was possible to validate the model. The thermodynamic model gave the highest possible steady-state temperature that the validation transmission could have for a given operational speed. To further validate this model, an additional test would need to be conducted which fully removes all conduction to the external environment. Despite this, the validation results in this section were sufficient enough to be able to predict the final steady-state temperature of the DOT transmission under the condition that only convection and radiation are used to transfer heat to the external environment.

### 6.2.6. Sensitivity Analysis

A sensitivity analysis was conducted to determine how a change in input variables affect the final steady-state temperature of the thermodynamic model. Three main input variables used to model the validation drive in section 6.2.5 were altered slightly to determine its effect on the final steady-state temperature of the ground annulus. The three main input variables that were altered are the ambient temperature ( $T_a$ ), the friction coefficient in the flex-roller section ( $\mu_{FR}$ ) and the thermal conductivity coefficient ( $k$ ) of the drive material. These variables were chosen because they are the main inputs in the thermal model that have the highest possibility change slightly. All the boundary conditions and dimensions are the same as the model shown in section 6.2.5. Each variable used in the sensitivity analysis was individually altered in four steps of equal spacing, while all other variables remained constant. The resulting change in steady-state temperature was plotted as a function of that variable. The plot showing the change in steady-state temperature as a function of ambient temperature is shown in figure 6.36.

The plot in figure 6.36 shows that there is a positive linear relation between the ambient temperature and the steady-state temperature. The gradient of the line is given in the linear equation on the top right of the figure. This result verifies that an increase in ambient temperature results in an increase in final-steady state temperature. There is a linear relation because the change in convective heat transfer coefficient and radiation film coefficient, shown in section 4.2.3, is minimal at the small increments in ambient temperature. Making the difference in the nodal and ambient temperature shown in equation 4.22 the dominant contributor. This difference increases linearly as the ambient temperature increases. The change in percentage is shown in figure 6.39. The plot showing the change in steady-state temperature as a function of the friction coefficient in the flex-roller section is shown in figure 6.37.

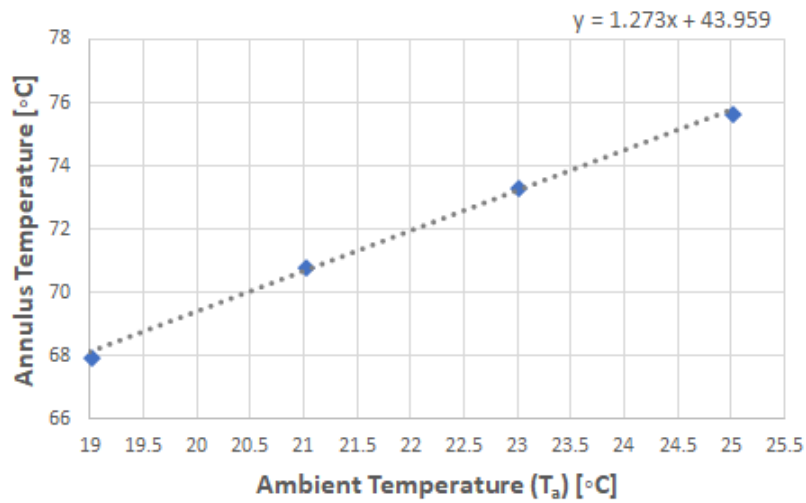


Figure 6.36: Ambient temperature sensitivity analysis

The plot in figure 6.37 also shows that there is a positive linear relation between the friction coefficient in the flex-roller section ( $\mu_{FR}$ ) and the steady-state temperature. The gradient of the line is given in the linear equation on the top right of the figure. This plot illustrates the effect of changing the coefficient ( $\mu_{FR}$ ) discussed in section 6.2.4 on the final steady-state temperature of the system. It was discussed in that section that the value of ( $\mu_{FR}$ ) could change depending on lubrication or contamination. Using the validation test results, it was concluded that a coefficient of 0.0016 could best be used to describe the unlubricated transmission system. Altering this value has an effect on the heat power calculated by the model, which directly affects the steady-state temperature. In the plot shown in figure 6.37 the value for ( $\mu_{FR}$ ) was altered between 0.0013 to 0.00175, resulting in a total temperature difference of 14°C. There is a linear relation because the total friction moment ( $M$ ), shown in equation 4.2 increases linearly with a change in ( $\mu_{FR}$ ), resulting in a linear increase in heat power. The change in steady-state temperature as a function of ( $\mu_{FR}$ ) in percentage is shown in figure 6.39. The final plot showing the change in steady-state temperature of the ground annulus as a function of the conduction coefficient is shown in figure 6.38.

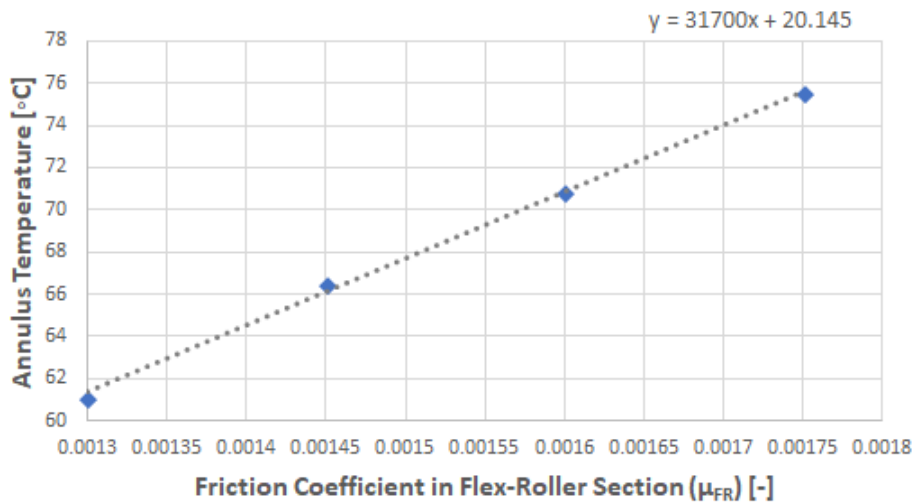


Figure 6.37: Torque due to applied load factor sensitivity analysis

The plot in figure 6.38 indicates a negative linear relation between the conduction coefficient ( $k$ ) of the drive and the steady-state temperature of the ground annulus. The gradient of the line is given in the linear equation on the top right of the figure. The conductive coefficient of the material was changed in steps of

5 W/m K between 41 W/m K and 56 W/m K. This resulted in a change in ground annulus temperature from 71.1°C to 70.0°C. This result relates with what is supposed to happen, since an increase in conductive coefficient will result in more heat dissipation throughout the drive, relieving the heat build-up in the ground annulus. Changing the conductive coefficient only results in a slight change in temperature. This is because the ground annulus is located close to the heat source. The negative slope is also linear because the results of the conduction equations used to calculate the heat transfer, shown in equations 4.20 and 4.21 change linearly with an alteration in conduction coefficient. The change in steady-state temperature as a function of ( $k$ ) in percentage is shown in figure 6.39

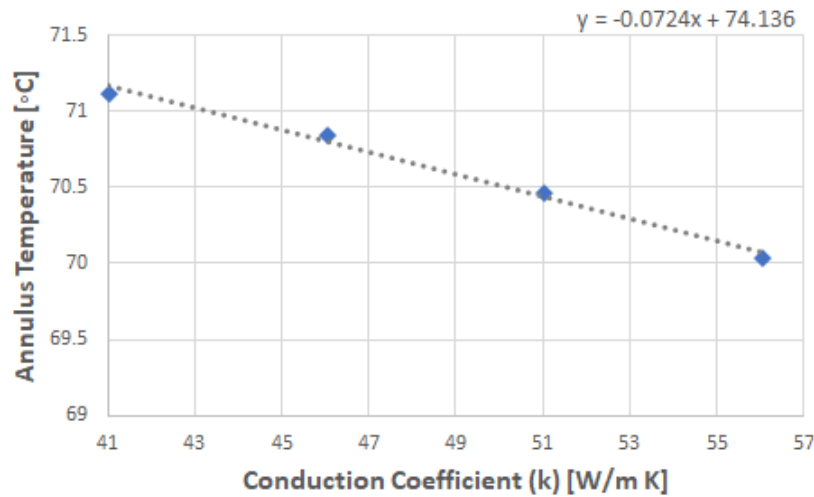


Figure 6.38: Conduction coefficient sensitivity analysis

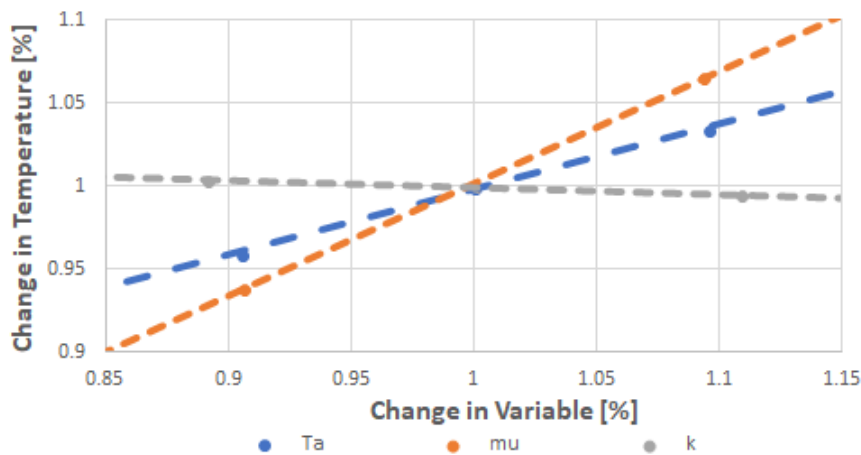


Figure 6.39: Change in temperature as a function of change in input variable

Figure 6.37 illustrates the effect, in percentage, of each of the previously described variables on the final steady-state temperature of the ground annulus. The x-axis indicates a change in one of the three variables, ( $T_a$ ), ( $\mu_{FR}$ ) or ( $k$ ) and the y-axis shows the change in steady-state temperature on the ground annulus. Using this plot the three variables can be compared to each other. The variable which has the greatest effect on the steady-state temperature is ( $\mu_{FR}$ ), where a 10% change result in a 6% change in steady-state temperature. The variable with the second greatest effect is the ambient temperature ( $T_a$ ), a 10% change in ambient temperature results in a 4% change in steady-state temperature. The variable with the least effect is the conduction coefficient which only results in a 1% change in temperature as it is changed by 10%. The variable that required the most precision is ( $\mu_{FR}$ ) however all three variables cause a change in steady-state temperature less than the change in that input variable, which is beneficial for the model. This means that if an input variable changes by 10% the change in steady-state temperature will always be less than 10%, resulting in a more stable model.



## Full Scale Prediction

The thermodynamic model has now been verified and validated with a smaller transmission. Using those results the steady-state temperature of the DOT wind turbine can be predicted for its operating condition. This chapter is split into two sections focusing on different topics. The first section, (7.1) provides all the design requirements, dimensions and assumptions of the DOT transmission. The second section, (7.2) provides the results of the thermodynamic model, including an analysis of those results.

### 7.1. Requirements, Dimensions and Assumptions

Figure 7.1 provides the geometry of the DOT transmission with all the required input dimensions. The heat generating points of the system are the six bearings and the flex-rollers. The transmission uses two separate types of bearings, the type and dimension of each bearing can be found in table 7.1. The steady-state temperature at maximum operating velocity is determined, the drive needs to operate at a maximum of 28 input revolutions per minute. To meet the top-level torque requirement of 280 kNm, two transmission systems are used, dividing the total torque by two.[8] Therefore a single drive has 140 kNm of torque. The transmission comes in direct contact with ambient air at 21°C. This means that there will be pure convective and radiation heat transfer to the environment. No additional cooling is assumed in the transmission. All other input variables and dimensions are given in table 7.2.

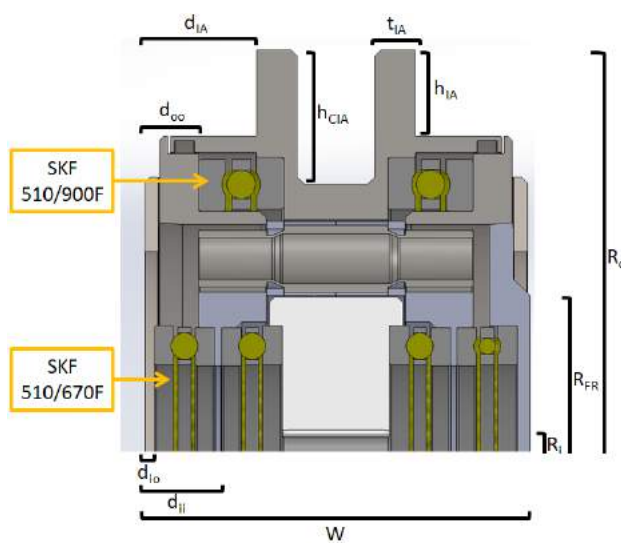


Table 7.1: The dimensions and constant of the bearings used in the DOT transmission

Bearing	Dimension	Value
SKF 510/900F	Outer Diameter	980 mm
	Inner Diameter	900 mm
	Thickness	63 mm
	Static Load Rating ( $C_s$ )	4900 kN
	Minimum Load Factor ( $A$ )	120
SKF 510/670F	Outer Diameter	670 mm
	Inner Diameter	730 mm
	Thickness	45 mm
	Static Load Rating ( $C_s$ )	2400 kN
	Minimum Load Factor ( $A$ )	30

Figure 7.1: The dimensions in DOT transmission indicating all the input geometry features for the model and the bearing types

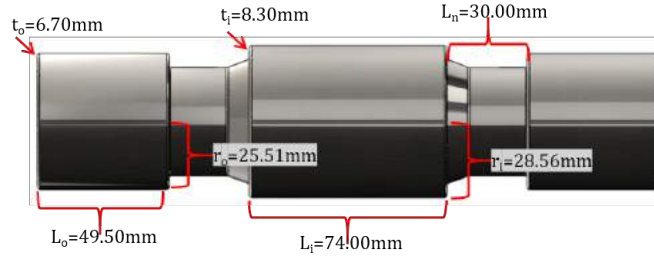


Figure 7.2: The dimensions of the flex-roller used in the DOT transmission

Table 7.2: Dimensions and other input variables of the DOT transmission thermal model [8]

Variable	Description	Value	Unit
$rpm$	Input Rotational Velocity	28	1/min
$Tor$	Input Torque	140	kNm
$GR$	Gear Ratio	1:20	-
$Z$	Flex-Roller Number	36	-
$R_o$	Outer Radius	570.0	mm
$R_i$	Inner Radius	275.5	mm
$R_{FR}$	Flex-Roller Contact Radius	389.6	mm
$W$	Transmission Axial Width	295.0	mm
$d_{ii}$	Inner Inside Bearing Axial Distance	55.0	mm
$d_{io}$	Inner Outside Bearing Axial Distance	5.0	mm
$d_{oo}$	Outer Outside Bearing Axial Distance	30.0	mm
$d_{IA}$	Input Annulus Coupling Axial Distance	79.0	mm
$t_{IA}$	Input Annulus Coupling Thickness	4.0	mm
$h_{IA}$	Input Annulus Coupling Height	64.5	mm
$h_{CIA}$	Input Annulus Coupling Depth	100.0	mm
$k$	Thermal Conductivity Steel	46	W/(m K)
$\epsilon$	Emissivity	0.79	-
$T_a$	Ambient Temperature	21	°C
$v_g$	Kinematic Viscosity Grease [52]	10,5	cSt
$v_g$	Kinematic Viscosity Oil [53]	7.2	cSt

The six thrusts bearings (two 510/900F and four 510/670F) in the transmission were assumed to operate on the most favorable thermodynamic condition, meaning that the minimum required axial load ( $F_{amin}$ ) is applied to them. Equation 7.1 was used to determine the load for the two types of bearings given in table 7.1.[16]

$$F_{amin} = 1.25C_s/1000 \quad (7.1)$$

In which ( $C_s$ ) is the static load rating of the bearing. The minimum load was then calculated for the bearings using there operating condition. Table 7.3 indicates the rotational velocity and axial force of each thrust bearing. The rotational velocity was determined by the model using the steps explained in section 4.1.3 and the force was calculated using equation 7.1.

Table 7.3: Rotational Velocity and Load of Bearings in DOT Transmission

Variable	Outer Bearing	Inner Outside Bearing	Inner Inside Bearing
Velocity (rpm)	28.0	533.4	36.3
Force (kN)	6.1	3.0	3.0

Table 7.3 shows that the outer bearing has the lowest rotational velocity but the highest axial force. This bearing has the lowest rotational velocity, because it couples the housing to the input annulus (velocity difference shown between  $V_1$  and  $V_2$  in figure 4.7). However, it is the largest bearing used in the transmission,

resulting in a high ( $C_s$ ), increasing ( $F_{amin}$ ). The other two bearings are the same type of bearing, making ( $F_{amin}$ ) the same. Despite this, one bearing operates at a larger rotational velocity compared to the other. This is because one bearing is used to couple the ground annulus to the idling annulus (large velocity difference shown between  $V_2$  and  $V_3$  in figure 4.7) and the other the idling annulus to the output annulus (small velocity difference shown between  $V_3$  and  $V_4$  in figure 4.7). The difference in velocity has a large effect on the amount of heat each bearing generates. The next unknowns are the rolling friction coefficient of the flex-roller section (if the transmission is run unlubricated) and the torque due to applied load ( $f_l$ ) and lubrication ( $f_o$ ) factors (once the transmission is lubricated).

Looking at the unlubricated case, it was assumed that the DOT transmission has the same flex-roller rolling friction coefficient ( $\mu_{FR}$ ) as the validation drive. This is because the working principle of both transmissions are identical and the cage in the DOT transmission resembles that of the validation drive. Therefore, the value calculated in equation 6.10 was taken, giving a ( $\mu_{FR}$ ) of 0.0016.

To determine ( $f_l$ ) and ( $f_o$ ) for the lubricated case, the tables in figure A.4 and A.1 of the appendix was used. The flex-roller section, as explained in section 4.1.3, resembles that of caged cylindrical bearings. This means that the value for ( $f_l$ ) can vary between 0.0002 (for light series bearings) to 0.0004 (for heavy series bearings). In order to determine the correct value for ( $f_l$ ) a roller bearing with similar geometric properties as the flex-roller section was found. The code of this bearing is N28/710, meaning that the series number is 28.[55] Using the method explained in section 4.1.2 and figure A.4 the resulting ( $f_l$ ) factor used in the model is 0.0029. The bearing lubrication factor ( $f_o$ ) is then determined depending on what lubricant is used in the lubricated case. Looking at the type of lubricants, multiple scenarios were assumed, resulting in a different ( $f_o$ ) factors. The steady-state temperature for four lubricant types were evaluated. These four lubrication scenarios are, not lubricated, greased, oil mist and oil bath. The lubrication factor ( $f_o$ ) for the scenarios are given by the table in figure A.1. The table shows that a range of ( $f_o$ ) values can be used for a given lubrication. Since the flex-roller section resembles 'cylindrical roller bearings with cage' the grease, oil mist and oil bath values were taken from that row in the table shown in figure A.1. The full range of ( $f_o$ ) for the four lubrication types were analyzed, the results can be found in section 7.2.

## 7.2. Prediction Results

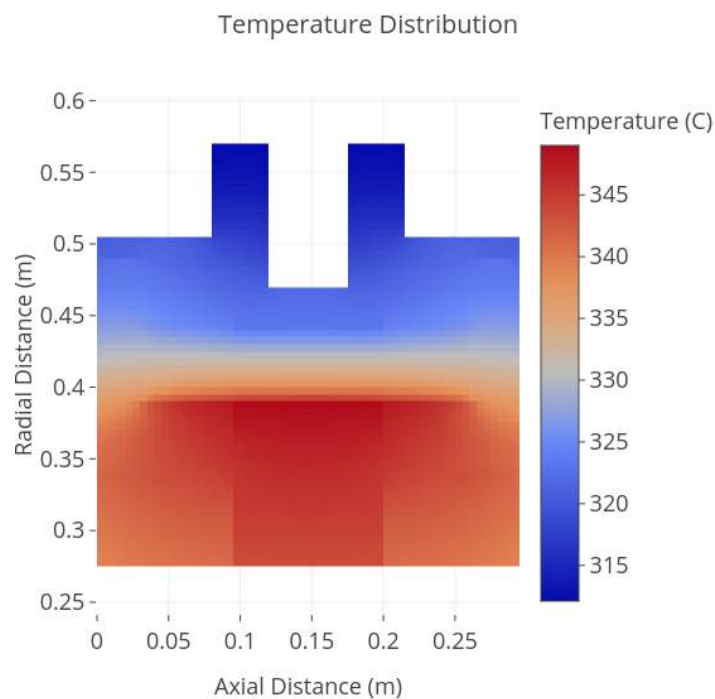


Figure 7.3: Heat-map of the DOT transmission using minimum grease condition, maximum temperature is 349°C measured at flex-roller/output annulus contact location

The inputs given in table 7.2 were inserted in the thermal model to predict the final steady-state temperature of the DOT system. The resulting steady-state heat-map for the DOT transmissions is shown in figure 7.3. In this heat-map the minimum amount of lubrication in the system is assumed. This means that the bearings and the flex-rollers are greased. The kinematic viscosity of the grease was taken to be 10.5 cSt and the minimum ( $f_o$ ) factor for the greased situation was used to calculate the lubrication friction moment ( $M_v$ ), which is 0.6. The temperature in this heat-map is then compared with the steady-state temperatures of the unlubricated case and the two other lubrication cases stated in section 7.1.

The heat-map shows that an average steady-state temperature of around 330°C is reached in the transmission. This temperature is the highest temperature that the transmission can achieve under the given operating condition. If the transmission is used in a wind-turbine, conductive heat transfer to the external environment will be present, reducing the overall temperature greatly. This change in temperatures was explained with the validation drive and is shown on the plot in figure 6.33. The highest temperature in the transmission is 349°C. This is located on the inner contact point of the flex-roller. This location has the highest temperature because the contact rotational velocity at that location is the highest, section 6.2.5 further explains this. The minimum temperature of 312°C, is on the top of the input annulus coupling. The lowest temperature is at this location because it is the furthest away from the heat generating points and has highest external nodal surface area. The high surface area has to do with the cylindrical shape of the drive, with more surface area being present on the external side of the cylinder as compared to the internal side, this is further explained in section 5.3.2. The final steady-state temperature largely depends on the type and amount of lubrication used in the transmission. Table 7.4 lists the final steady-state temperature of the system using the four lubrication cases described in section 7.1 and the plot in figure 7.4 gives an overview of the heat power going into the system depending on the different lubricants.

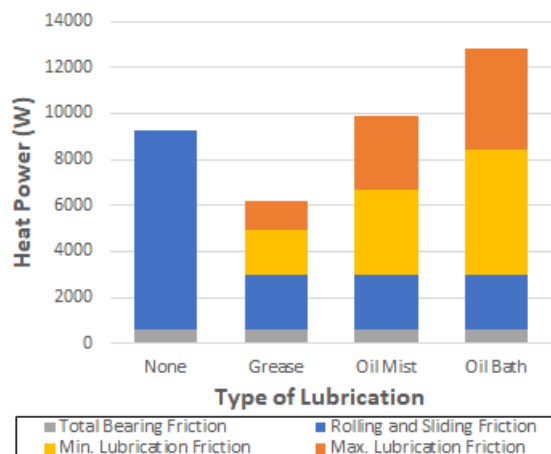


Table 7.4: Maximum steady-state temperature and thermal efficiency of the transmission for the different lubricants, the range is determined using minimum and maximum lubrication friction

Lubricant	Temperature [°C]	Efficiency [%]
None	442	2.3
Grease	349-382	1.2-1.5
Oil Mist	394-457	1.6-2.4
Oil Bath	430-504	2.1-3.1

Figure 7.4: Total heat power going into the transmission based on the different lubricants, minimum and maximum lubrication friction is determined based on the range of ( $f_0$ )

Three conclusions can be drawn from the plot in figure 7.4 and table 7.4. Firstly, figure 7.4 shows that there is a drop in rolling and sliding friction once lubrication is added to the system. This drop occurs because the effects that cause rolling and sliding friction (explained in section 4.1.1) are reduced once the local static and dynamic friction coefficient decreases. The main areas where the heat generated by friction is reduced are the interaction between the roller and the guiding features and the slip along the contact area shown in figure 4.1. The same normal force is present for the unlubricated as the lubricated cases, however, the local dynamic and static friction coefficients are decreased once a lubricant is added. This reduces the overall rolling and sliding friction in the system, lowering the heat generated from those factors. Adding lubrication does result in additional heat being generated by lubrication friction, the effects of this are discussed in the second conclusion.

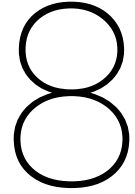
The second conclusion is drawn by analyzing the three lubrication cases (greased, oil mist and oil bath). The plot in figure 7.4 shows that lubrication friction increases between the three cases. The type and amount of lubrication used could alter the total thermal efficiency of the transmission between 1.2% and 3.1%. Each lubricant has a range of lubrication friction that it generates, provided in the orange section of the plot in fig-

ure 7.4. This range is given because the flex-roller cavity (the empty space that the flex-rollers move in), does not exactly match that of a specific cylindrical roller bearing, making it difficult to determine the exact ( $f_o$ ) factor. Additionally, the amount and type of guiding features and the amount of lubrication used also effect the total lubrication friction. Using a range incorporates the majority of those uncertainties. The difference in the amount of lubrication friction each condition generates can be explained by looking at the equation for viscous friction torque (shown in equation 4.8). This equation is a function of two fixed variables, the pitch diameter ( $d_m$ ) and rotational speed ( $n$ ), and two variables that are altered depending on the lubrication, the lubrication factor ( $f_o$ ) and the kinematic viscosity ( $\nu_o$ ). The flex-rollers are assumed to be three separate rollers bearings (as explained in section 4.1.3), each with a relatively large ( $d_m$ ) for a bearing and a rotational velocity above 500 rpm. Those relatively large fixed variables make it that just a slight increase in ( $f_o$ ) or ( $\nu_o$ ) has a large impact on the final lubrication heat power generated. When switching from grease to oil the factor ( $f_o$ ) increases while the kinematic viscosity ( $\nu_o$ ) decreases. The relative increase in ( $f_o$ ) is larger than the decrease in ( $\nu_o$ ), resulting in an increase in temperature. The factor ( $f_o$ ) increases because more of the flex-roller section's cavity is filled with lubricant, increasing churning. This additional churning increases the fluid's internal friction, resulting in more heat being generated. That is why low kinematic viscosity oils should be used in bearings to counter-act the increased churning.

The third conclusion can be made by comparing the heat power of the oil mist and oil bath case with the unlubricated case. Figure 7.4 indicates that a part of the range of the oil mist and oil bath case generates more heat than the unlubricated case. This occurs because the heat generated by lubrication friction becomes larger than the reduction in rolling and sliding friction caused by the decrease in static and dynamic friction coefficient. This is referred to as over-lubrication and is explained further in section 4.1.1. Closed systems should avoid using oil baths that completely fill the cavity of the rolling surface. Generally speaking, 30-50% (depending on lubrication viscosity) of the surrounding space of the housing should be filled.[16] If the system is not closed and allows for fluid circulation outside of the transmission, using oil can be beneficial as it can transport heat out of the system. This could be done by implementing a pump to actively circulate the lubricant out of the system, cooling it, then inserting it back. There is a trade-off in this system between the additional lubrication friction generated caused by increased churning and the beneficial effect of active cooling. Since the thermal model does not take active lubricant cooling into consideration, adding more lubricant than the minimum required amount will result in more heat.

Overall, using this model the steady-state temperature of the DOT system can be predicted. The temperature that the model generates is the maximum heat that the transmission will experience, as conduction to the external environment is not taken into consideration. The next step would be validate the model with a full-scale transmission test to determine its accuracy. It was not possible to conduct this validation procedure in the time available for this thesis and it will need to be validated in the next analysis. However, it can be determined using the model that a lubricant with a low kinematic viscosity must be used in order to reduce the amount of heat the system generates. Additionally, oil baths in the DOT system should be avoided, unless active lubricant cooling is used, as they result in the highest ( $f_o$ ) factor (as shown in figure A.1 of the appendix). At the maximum operating point (input rotational velocity of 28 rpm), active cooling would most likely need to be implemented to decrease the heat in the system. The total amount of additional cooling required can be determined once the conductive boundary conditions of the system are known. The model includes an option to artificially add material on the boundary of the transmission, taking conduction to the external environment into consideration. However the geometry and temperature at multiple locations around the test-bench need to be measured for a single speed. Those values could then be used as inputs in the model to predict the steady-state temperatures on the remaining velocity points.





# Evaluation, Conclusion and Future Work

This chapter evaluates the knowledge acquired during the creation of the thermal model, the general results of the thermal model and the research questions. This evaluation will help provide a conclusion, summarizing all the main results given in this thesis. Based on the conclusion future research topics are suggested to further develop the thermal model. The evaluation and conclusion can be found in section 8.1 and the future work topics in section 8.2.

## 8.1. Evaluation and Conclusion

The goal of this research was to create a general thermal model for the novel transmission used in the DOT wind turbine. The purpose of this thermal model was to determine the thermal properties of the drive at the beginning of a design process. Using preliminary geometry and performance criteria an initial thermal analysis of the transmission could be made. The thermal model was created using the research objective and questions shown in chapter 3. The research objective was to develop a thermal model for the novel transmission used in the DOT wind turbine and validate it with a scaled prototype. In this thesis the research objective was met as a thermal model was created and was validated with a scaled version of the transmission's working principle. Each research question shown in chapter 3 contributed to the creation of this model and are analyzed in this section to see if the questions were answered.

The first research question regarded the heat generation of the transmission. It was concluded that the transmission had 17 components which could be divided into multiple categories. The parts are shown in figure 2.10 and the categories are shown in table 2.1. In the transmission, the bearings and flex-rollers are the heat generating components. The heat generated by these components can be calculated using the empirical relations shown in section 4.1. That section indicated that three forms of friction are responsible for heat generation in rolling elements; rolling, sliding and lubrication friction. Since multiple factors contribute to the heat generation of a rolling elements inside of track, empirical relations were used to calculate the heat power by determining the total friction moment in the system. If a lubrication film is present in between the flex-roller and the raceway, the rolling and sliding friction moment are calculated using equation 4.4 and the lubrication friction moment is calculated using equation 4.8. If a lubrication film is not present, equation 4.2 is used. This does however require the rolling friction coefficient ( $\mu_B$ ) to be determined using a test. These three equations are a function of the size, geometric features and operating conditions. The heat generation of the bearings could be calculated directly using those relations. However some assumptions had to be made for the flex-rollers. The flex-rollers run on three separate tracks with different rotational speeds, therefore it was assumed that the flex-rollers could be seen as three separate roller bearings. Using this assumption, the empirical equations in section 4.1.2 could also be used for the flex-rollers. These relations and assumptions allowed the heat power in the system to be modeled correctly, answering the first research question.

The second research question focused on the heat dissipation in the system. All three forms of heat transfer are present in the transmission and were taken into consideration in the thermal model. The relations are shown in section 4.2. Externally, convection and radiation are dominant. It was assumed that the transmission can be seen as a cylinder, therefore natural convection coefficient equations for cylinders were used to model

the external heat dissipation. Radiation was also modeled taking the pseudofilm coefficient of a cylinder. Internally, conduction and convection are dominant. Conduction was modeled in the housing and the annuli and convection was modeled between the main rotating components. The model assumed a homogeneous temperature around the circumference, hence, only the radial and axial heat transfer were modeled. Assumptions had to be made in the flex-roller section to take the change in material around the circumference and the movement of the flex-rollers during operation into consideration. The flex-roller section was assumed to be constructed out of multiple 'nodal channels', as seen in section 5.1.2. The 'nodal channel' wall thickness and flow velocity in the channel changes in radial direction. The channel flow velocity also depends on the speed the flex-rollers move around the circumference of the drive, which also depends on the input rotational speed. This was then modeled using conduction and forced convection relations in parallel and in series. These heat dissipation relations made it possible to model the conduction convection and radiation in the system answering the second research question.

The solving method of the transmission was identified through the third research question. The temperature was assumed to be homogeneous around the circumference, therefore only radial and axial heat transfer was taken into consideration. A nodal network was used to calculate the steady-state temperature of the transmission at a given point in its cross-section. A single node transferred heat in two radial and axial directions. If the node was located on the exterior of the drive it would have convection and radiation heat transfer with the ambient temperature, an example of this is shown in equation 5.1. A node located on a heat generating location would have the heat power as input. These nodes resulted in a system of non-linear equations that needed to be solved simultaneously in order to determine the steady-state temperature. The Powell hybrid method was used to solve this system, because it is a robust solving method. There is a trade-off in the thermal model between the computational time and the resolution. To have the most optimum result a node surface area that is 1000 times smaller than the cross-sectional surface area was used. Using a nodal network to model the heat propagation and determining how the system of non-linear equations was solved simultaneously, answers the third research question.

The fourth research question focused on the verification and the validation of the thermal model. The simultaneous solver of the thermal model was verified first as shown in section 6.1.1. The results of the thermal model were compared with the results of solving the equation analytically for a two dimensional problem. The thermal model was then verified further using ANSYS, as shown in section 6.1.2. Two geometries were used as inputs in ANSYS and in the thermal model. The steady-state temperature of both simulations were then calculated using the same boundary conditions. The first geometry did not use flex-rollers while the second one did. The results of both models related with each other, with both simulations having the same temperature spread. Validation was then conducted in section 6.2, by comparing the heat power and the steady-state temperature of a smaller version of the transmission with the results of the thermal model. The validation drive was run without lubrication at multiple input rotational speeds until the temperature in the transmission reached steady-state condition, at which the temperature and input power were measured. Section 6.2.4 explains that the heat power of the transmission can be modeled with a flex-roller section rotational friction coefficient ( $\mu_{FR}$ ) of 0.0016. The rolling friction coefficient is higher than standard lubricated cylindrical roller bearings even though both systems are comparable. This difference comes from the flex-roller section being unlubricated, which amplifies the local dynamic and static friction coefficients increasing the rolling friction coefficient. When lubrication is used, the rolling friction coefficient in the flex-roller section should decrease. The heat power calculated by the model using the determined ( $\mu_{FR}$ ) was then validated for multiple measurement points. This was done by comparing the thermal model's calculated power for a given input velocity with the measured power during the validation test. There was a maximum 4% difference between the two values, validating the heat power component of the software. Using those heat power values the steady-state temperature computed by the thermal model was compared with the measured values, this is shown in section 6.2.5. The temperature that the thermal model predicted was over 50% higher than the values measured in the test. This difference occurred because the conduction going through the test-bench was not taken into consideration in the thermal model. Using ANSYS, a simulation of the validation transmission without and with the test-bench was run with the resulting heat power at multiple input speeds. The calculated steady-state temperatures were then compared with the modeled and measured values. The thermal model related to the ANSYS results of the validation transmission without test-bench, and the measured temperatures related with the results of the ANSYS simulation with test-bench. This proved that conduction through the test-bench was the main reason behind the difference in temperature. Throughout this verification and validation procedure

the fourth research question was answered.

The thermal model was finally used to predict the steady-state temperature of the DOT transmission. Since the boundary clamping conditions are unknown it was assumed that only convection and radiation heat transfer are present to the external environment. The temperature was modeled at maximum operating condition for multiple lubrication cases, the results are shown in section 7.2. The temperature given by the thermal model is the maximum temperature for a given condition since conduction through the wind turbine's structure is not taken into consideration. The lubrication used in the transmission is largely responsible for the amount of heat-power generated. The thermal model can then be used to determine the best form of lubrication for the DOT transmission. When more is known about the geometry of the transmission's clamping structure the thermal model can be modified to predict the final steady-state temperature with greater accuracy.

Overall, the output of this thesis provided a solid understanding of the thermodynamic principles governing this novel transmission. These principles can be used in the future to predict the maximum steady-state temperature a transmission will experience under given operating conditions. The thermal model would allow heat properties of the transmission to be taken into consideration in the conceptual design phase, removing the need to reiterate the design further its life-cycle. An overview of the where the thermal model would be used in the design process compared to a traditional heat analysis is shown in figure 8.1.

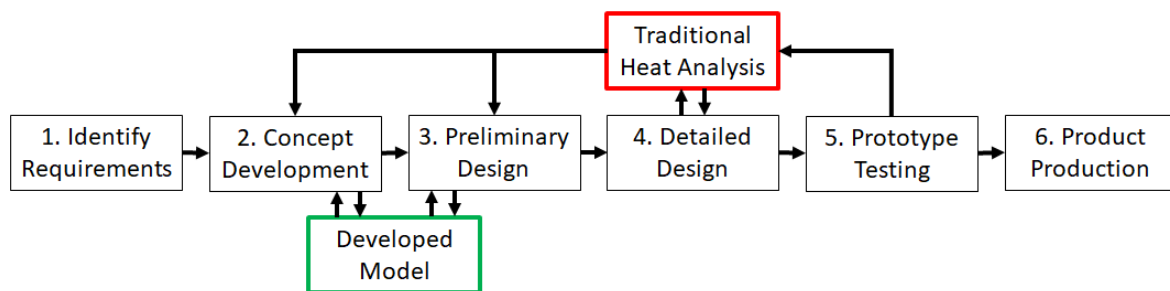


Figure 8.1: Flow-chart comparing traditional heat analysis to the thermal model in a standard design process

Figure 8.1 makes clear that the thermal model can be used during the concept and preliminary design phases, which is earlier in the design process in comparison to a traditional heat analysis. For this novel transmissions it was only possible to conduct a thermal analysis during the detailed design or prototype phase. This was because the transmission needed to be designed in more detail first before it can be used in common third-party software for heat analysis. If unfavorable heat properties were discovered during the traditional analysis the design process will have to be re-iterated. The use of the thermal model, developed in this thesis, will remove this iteration process. Additionally, the thermal model can calculate the steady-state temperature of the transmission in a fraction of the time compared to traditional methods. This allows for numerous iterations to be conducted in the same time as a single iteration using a traditional heat analysis. This is the first thermal model made for this type of transmission, therefore for expansion, a number of topics are identified for future work, these are given in section 8.2.

## 8.2. Outlook and Future Work

The results of this thesis, can be used to identify future studies that investigate and improve specific parts of the thermal model. This section provides an explanation of important future studies. The three future studies which will be discussed are, a validation analysis of the full-scale model, a detailed analysis of fluid behavior in the transmission and adapting the model for unsteady-state condition.

1. The first future study to be conducted is to validate the model with the transmission used in the wind turbine. The boundary conditions gathered during this study could then be implemented in the thermal model to have a more accurate prediction of the final steady-state temperature. The transmission needs to run at multiple input speeds for a given amount of time until steady-state condition is reached. Those results can then be compared with the results of the thermal model. If additional forms of cooling are applied to the transmission, those forms will have to be implemented in the thermal model. Once the thermal model is validated for large scale transmissions it could be used as a general thermal model for a larger amount of applications.
2. The second future study to be conducted is to further analyze the effect of lubrication on the transmission. It was concluded that at high rotational speeds and for bearings with large radii the lubrication friction torque becomes the dominant factor in heat power. A more detailed analysis would have to be conducted to see if lubrication does in fact play such a large role. Computational fluid dynamics would need to be used to determine the behavior of the flow within the flex-roller section. The results of this analysis then have to be compared with the values calculated by the empirical relations. Additional test would also need to be conducted using different forms of fluid in the transmission to determine how it affects the measured steady-state temperature.
3. The third future study to be conducted is to adapt the model for unsteady-state conditions. This would allow the model to predict the temperature of the drive as a function of time. In order to do this the main thermodynamic relations would have to be altered in order for it to be a function of time. The numerical solver would also have to use a transient numerical solving method. Having unsteady-state condition would allow the model to predict the thermal properties of the drive throughout its complete operating cycle. This model could then be verified using the validation results found in this thesis. Although the solving method would take longer to solve, it would result in a greater understanding of the thermal properties of the transmission.

# II

## Annotation Entrepreneurship



# 9

## Introduction Annotation Entrepreneurship

A vast majority of products in modern life rely on gearboxes. Some of these technologies include cars, power plants, jet engines, wind turbines, telescopes and solar panels. Gearbox allow those technologies to operate as efficient and precise as possible. A gearbox in its basic form is an old technology, however, innovations to this technology throughout the centuries have allowed it to greatly improve the performance of all applications using it.

The first gearbox was invented by Archimedes, with which he proposed that he could move the earth if he was given a lever long enough. Thereafter the gearbox was used in almost every technology that required rotation and movement. With each generation improving it in increments, allowing it to be applied to more industries. Two fundamental incremental breakthroughs in this technology are the "herringbone" and the "strain wave" gears. The "herringbone" gear allowed André Citroën to power the industrial revolution across Europe and the "strain wave" gear developed in 1950's allowed for precises gearbox movement, turning it into the backbone in the space race and modern robotics. These breakthroughs increased the performance of existing applications while also opening new possibilities. The Archimedes drive used in the DOT wind turbine can be seen as another of these incremental improvements. This why the market potential of this technology is analyzed and discussed in this part of the thesis.

The analysis of the Archimedes drive will investigate multiple aspects of this technology. Firstly, an overview of the technology is given and it is explained why it can be seen as a breakthrough in transmission technology. Secondly, an in-depth market analysis is given to determine it's potential. The chosen focus market are wind turbines, robotics and electric vehicles. Finally, a strategic critical path is shown, where the technology is now and which steps need to be taken to ensure maximum market potential.



# 10

## Innovation Explanation

In this chapter the current state of transmission or drive technology is explained. This explanation is used to identify current problems with similar exciting technologies. Once those topics have been discussed the real market needs can be identified. Finally the value proposition of the Archimedes Drive is given.

### 10.1. Current Technologies

The transmission market as a whole is conservative, a large majority of the technology used today rely on well understood and ancient principles. However, there has been a push to design and use better gearbox technologies due to the increased performance requirements in all mechatronic systems. The desired performance increase can vary by either increasing precision, efficient or torque density. The technologies today which require these transmissions are pushing on the bounds of what established systems can offer. Meaning that in order to make further progress a new drive technology needs to be implemented.



Figure 10.1: Chain transmission [57]

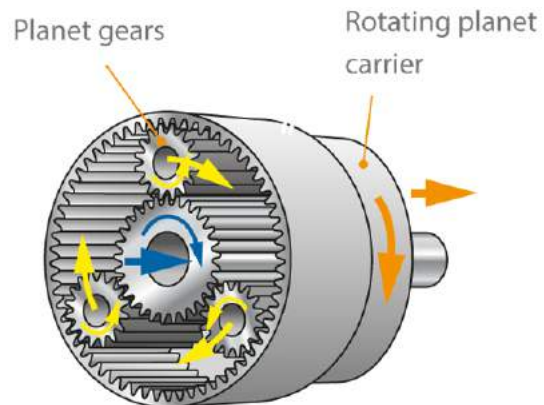


Figure 10.2: Gear transmission [58]

Transmissions can be arranged in two categories; belt/chain transmissions and gears. These two categories are illustrated in figures 10.1 and 10.2 respectively. Transmissions can be used to reduce (Speed Reducer) or increase (Speed Increaser) the speed of the input, this in turn increases or decreases the output torque respectively. It is preferable to use a belt/chain system when a large distance needs to be covered by the transmission. They are light and require less integration of complex parts. Additionally, they are simple because, as shown in figure 10.1, they only require the use of two separate diameter wheels with a chain/belt connecting the two. The difference in diameter between these two wheels alters the gear ratio of the system. On the other hand if, the transmission needs to be compact a geared system is preferred. Figure 10.2 shows that this system uses an input sun which rotates the planet gears around the annulus. These planet gears are then connected to the rotating planet carrier, which becomes the output of the system. The geared system compared to the belt/chain system is more complex due to the interaction of all the rotating components and the meshing of the gear

teeth.

In geared transmissions there are three dominant types on the market, each of them occupying a different market segment and all three relying on gear teeth to transmit torque. These three technologies are strain wave gears (known as Harmonic Drives), cycloidal drives and planetary drives. Strain wave gears have a high torque density, meaning that they can handle high amounts of torque in a small package and are very precise. However, they are expensive due to their complex design. Additionally, their design causes them to have an inherently low efficiency. Strain wave gears can be seen mostly in high-end applications. If costs become a major design factor, but the favorable characteristics of the strain wave gears are desired, Cycloidal drives can be used. Their performance is comparable to that of strain wave technology without achieving as high of a value in torque density or precision. This decrease in performance makes them less complex, reducing the cost of the complete system. Planetary drives position themselves on the opposite side of the market. They are a relatively simple technology, making them highly efficient and inexpensive. Despite their high efficiency and low cost, they have a low torque density and low maximum gear ratio. An overview of these three systems can be seen in figure 10.4. The three drive systems are relatively mature technologies and no major improvements have been made in this field in recent history.

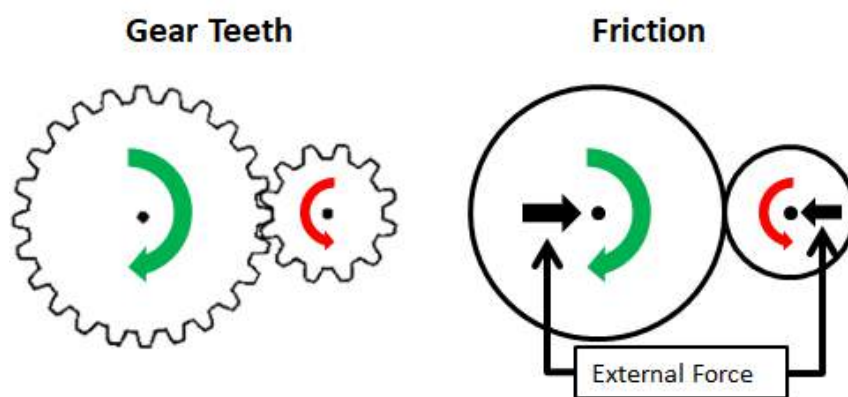


Figure 10.3: Comparing gear teeth to friction transmission

A less common form of transmission is a friction drive. Friction drives rely on friction rather than gear teeth to transmit the torque. An illustration comparing gear toothed systems with friction rollers is shown in figure 10.3. The figure shows that torque can be transferred in the friction based system as long as your force normal to the contact surface is high enough. The friction coefficient of the contact material in the drive can also be increased, resulting in a lower required external force. This technology is the least expensive transmission technology to make. This is because a complex gear teeth system does not need to be manufactured. Additionally, due to there only being rolling contact in this system, it can be seen as a bearing, making it highly efficient. However, it does require an external force to operate, therefore it can only be used in a small amount of applications. That is why this system is rarely used (apart from very specific applications).

## 10.2. The Innovation

The systems discussed in section 10.1 all have drawbacks, making it that not a single concept is viable for a large range of applications. Also, some design requirements cannot be met with what is currently available on the drive market. It is not possible for an application to have a gearbox with high torque density and efficiency which means a trade-off has to be made between the two. The Archimedes drive removes the need for that trade-off by combining the working principles of the technologies explained in section 10.1.

It is a unique speed reducer technology because it combines the high torque densities and precision seen in strain wave gears with the high efficiency and low cost of friction rollers. A complete technical overview of the technology named 'compound planetary friction drive' and its working principle can be found in section 2.3. Using the working principle, this transmission is able to reach a much higher gear ratio than standard planetary drives, drastically increasing the torque density while maintaining the efficiency of those systems. Since friction rollers are used, the manufacturing difficulties caused by producing the gear teeth are removed,

allowing the drive to be very efficient in power transmission and relatively inexpensive to produce compared to the competition. Figure 10.4 presents an overview the Archimedes drive compared to its competitors.

	Strain wave gear	Cycloidal drive	Planetary drive	Archimedes Drive
<b>Gear ratio (per stage)</b>	320:1	119:1	10:1	10,000:1
<b>Efficiency</b>	~80%	~93%	~97%	~95%
<b>Back-driveable</b>	Yes	No	Yes (up to 4-5 stages)	Yes
<b>Backlash</b>	Very Low	Considerable	Low	None
<b>Manufacturing</b>	Very Complex	Complex	Simple	Simple
<b>Design process</b>	Very Complex	Moderate	Simple	Simple
<b>Scalable</b>	Difficult	Very Difficult	Simple	Simple
<b>Lubrication</b>	Yes	Yes	Yes	No (optional for low-torque applications)
<b>Summary</b>	Relatively high torque capacity and gear ratio in a single stage, but the price and efficiency are major downsides	'Pretty good' general solution: definitely not as good as a strain wave gear, but more affordable	Cheap and efficient, but way too bulky and heavy for high-performance applications	The highest single stage torque capacity and gear ratio available, while being inexpensive and efficient

Figure 10.4: Comparing the different drive technologies

All the claims of the Archimedes drive are shown below:

- **High Power:** 10x compared to current systems
- **High Torque:** 3-4x compared to current systems
- **High Efficiency:** 95% achievable
- **Tailored Gear Ratios:** Gear ratios between 100:1 to 10,000:1
- **Low Weight:** 50% compared to current systems
- **Small Size:** Sub-centimeter drive diameter
- **No Backlash:** Zero backlash resulting in higher precision

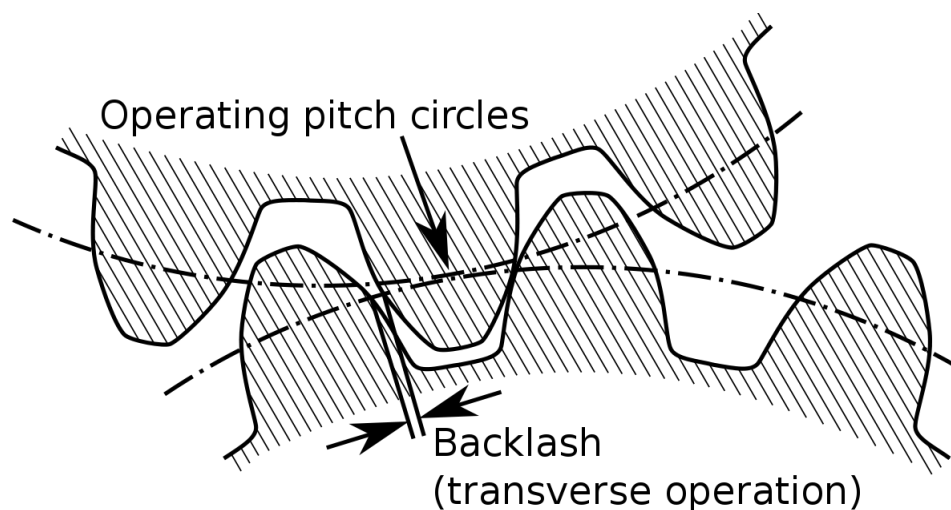


Figure 10.5: Backlash illustration [59]

Most of these advantages and their positive effect on the applications are self-explanatory. However, one advantage in particular sets this technology apart from what is currently on the market, which is zero backlash. Backlash, as shown in figure 10.5, is the spacing in between the gear teeth once they make contact with each other. If a drive has backlash it negatively effects the precision of the application using it, which is why it must be reduced as much as possible. For example, if the pointing of a telescope needs be an arc-second precise, any slight variation in that value, as a consequence of backlash in the system's transmission, would results in the telescope not exactly pinpointing the target object. A geared system will always have backlash because a perfect tooth mesh is impossible, meaning that the spacing shown in figure 10.5 will always be present. What makes the Archimedes drive unique, is that it does not use gear teeth. The roller always make contact and no spacing is present completely removing backlash. This unique advantage (along with the other benefits shown in figure 10.4) allows the Archimedes drive to increase technical performance and reduced total cost of ownership with no sacrifice in the life cycle. The need in today's market for such a technology is apparent and can be summed up with the following quote:

*"Robots, while exciting and useful, are difficult to design, tend to be heavy, complex, and expensive. The 'speed reducer problem' has plagued robot development for over 50 years, and has honestly been a major impediment to mass-market deployment of robots. New, low-cost, high-performance speed reducer technologies are desperately needed to make light-industry and consumer-grade robots a reality – speed reducers are, definitely, the enabling technology for these applications." - Bruce Schena[33]*

The Archimedes drive could make a significant contribution in upgrading current technology and open possibilities for new markets. An example of the technology's potential is that it can significantly improve the performance of expensive robots used by large industrial companies. It can also enable smaller companies to automate their factories with lightweight collaborative robots that can work alongside people. Also, due to the simpler manufacturing process compared to geared speed reducers, miniaturized versions of the drive can be made, allowing less space and weight to be taken up by the transmission. This would allow for better internal component layout in electric vehicles. As shown, there are many possible applications for this technology. A more detailed explanation of each market is given in chapter 11.

## Market Analysis

The Archimedes drive can be used in many industrial applications such as wind turbines, robotics, machine tools, prosthetics, electric vehicles and aircraft. The total potential market size of the Archimedes drive in all possible applications is estimated at \$ 70 billion. [32]. There are however some key markets where the need is higher compared to others. An overview of a few key markets with their main needs is shown in figure 11.1.

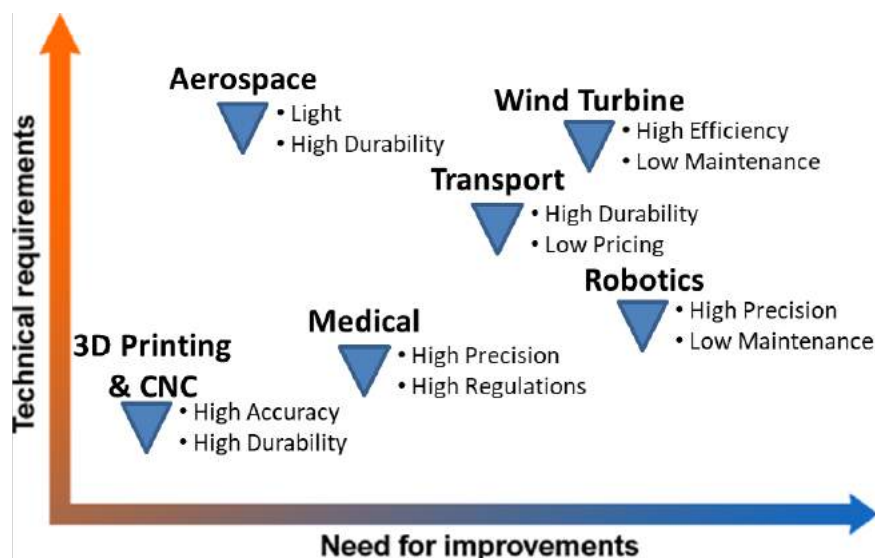


Figure 11.1: Overview and positioning of market

As can be seen in figure 11.1 there are numerous markets with varying main requirements for their transmission system. In this figure the industries are compared to each other by plotting their need for improvement in drive technology against the technical requirement the drive needs to reach before entering that specific market. The plot indicates that robotics, wind turbine and transport markets have the biggest need for a new gearbox technology. This is largely due to the growing demand for precise, efficient and cost effective drive technology. Although their requirements vary, an important corresponding requirement is the total lifetime and the operating environment of the drive. There are variety of operating conditions within robotics, however a majority of robots operate in well controlled environments. This reduces the overall technical requirements of the drive. Wind turbine have to operate maintenance free in high oxidation environment, which puts great stress on the design and requirements of the drive. The transport market can be seen as the middle point between these two markets. They have tougher operating environments compared to robotics but less compared to wind turbines. These three industries will be the main focus of the market analysis. The wind turbine market will be analyzed first, then the robotics market, followed by the transportation market.

## 11.1. Wind Turbines

In this section an analysis of the wind turbine market is conducted. A general overview of the market is given in section 11.1.1. With the overview, section 11.1.2 analyzes the potential competitors of the Archimedes drive. Finally, this section is concluded with the value proposition of the Archimedes drive in the wind turbine market.

### 11.1.1. Market Background and Size

The wind turbine market could benefit greatly from the use of the Archimedes drive. The total size of the wind turbine industry in 2015 was \$ 176.2 billion and will become \$ 250 billion by 2020.[34] As can be seen on figure 11.2, the cumulative capacity is 636.9 GW and by 2020 it is predicted to be 792.1 GW.[34] This industry is expected to grow each year at a constant rate.



Figure 11.2: Market forecast of wind turbine industry [35]

### Top 15 wind turbine suppliers in annual global market 2015

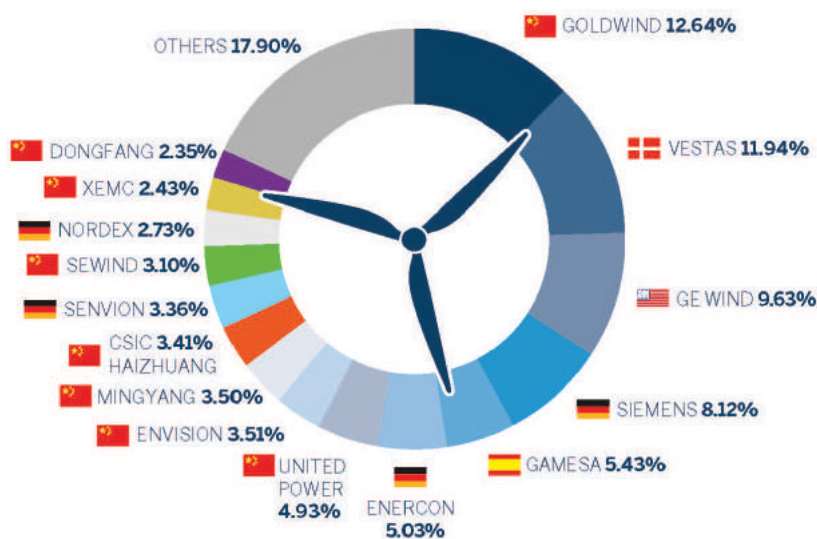


Figure 11.3: Wind supplier global market [36]

Wind turbines are divided into two categories based on location and two categories based on internal layout. The two location dependent categories are onshore (81% of total) and offshore (19% of total) wind turbines.[37] The two internal layout dependent categories are geared and direct drive turbines. Looking at all wind turbines, 74% are equipped with gearboxes and 26% are direct drive.[38] The pie chart in Figure 11.3 shows the market shares in 2015 of the main wind turbine suppliers. As the chart shows, the wind turbine market consists of numerous companies without one having more than 15% market share. The three largest companies are Goldwind (China), Vestas (Denmark) and GE (USA) each with 12.64%, 11.94% and 9.63% market share respectively. The two dominant countries in the global market are China (with more than 36% market share) and Germany (with more than 19%) with Siemens being the largest contributor (with a market share of 8.12%). It is expected that China will become an even bigger player in the future. There is heavy competition in this industry with competitors trying to gain a technological advantage over each other.

The capital expenditure of onshore wind turbines is about \$ 49/MWh, of which 71% is related to the turbine itself and the rest is related to the installation, infrastructure, contingency and management.[39] For offshore wind turbines, the capital expenditure is \$129/MWh and 33% is related to the turbine.[39] The baseline for operating expenditure is assumed to be \$15/MWh for onshore and \$ 37/MWh for offshore.[39] The large difference in costs between the two segments comes from the higher maintenance costs and costs of construction for offshore turbines. However, on average the wind blows 40% more often for offshore turbines. This results in higher initial investments, but also higher returns for offshore wind farms. A cost and weight breakdown per component of a wind turbine is seen in figure 11.1.

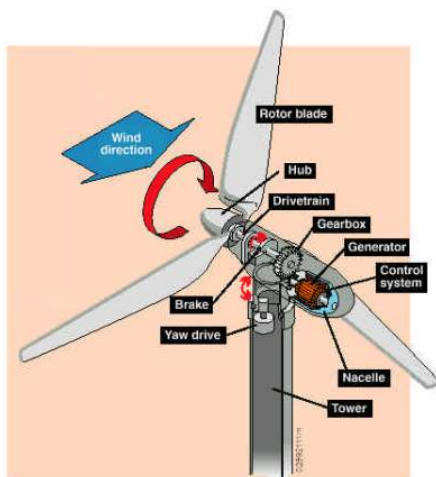


Table 11.1: Wind turbine component weight and cost[42]

Component	Weight (% of Total)	Cost (% of Total)
Rotor	10-14	20-30
Gearbox/Drivetrain	5-15	10-15
Generator System	2-6	5-15
Nacelle/Other	25-40	25
Components on Tower	35-50	75-90
Tower	620	10-25

Figure 11.4: Component layout of geared wind turbine[42]

Table 11.1 shows the cost and weight breakdown of the components shown in figure 11.4. As can be seen the heaviest and most expensive component of the wind turbine (not including the tower) is the rotor with it being 10-14% of the weight and 20-30% of the cost. The gearbox/transmission comes in second with it being 5-15% of the weight and 10-15% of the cost. Meaning that with a gearbox being approximately 13% of the cost of a complete wind turbine the resulting market size is around \$6 billion.[40] Wind turbines use a speed increasing gearbox with a ratio of 15 to 20 depending on the size and operating condition it is used in.

### 11.1.2. Competitors

The wind turbine gearbox market will grow further the coming years. It is expected to reach a size of \$7 billion by 2020. Of the \$7 billion the gearbox market for onshore wind turbines will have a market size of \$5.3 billion and offshore \$1.7 billion. The market share distribution of the wind turbine gearbox market is shown in figure 11.5.

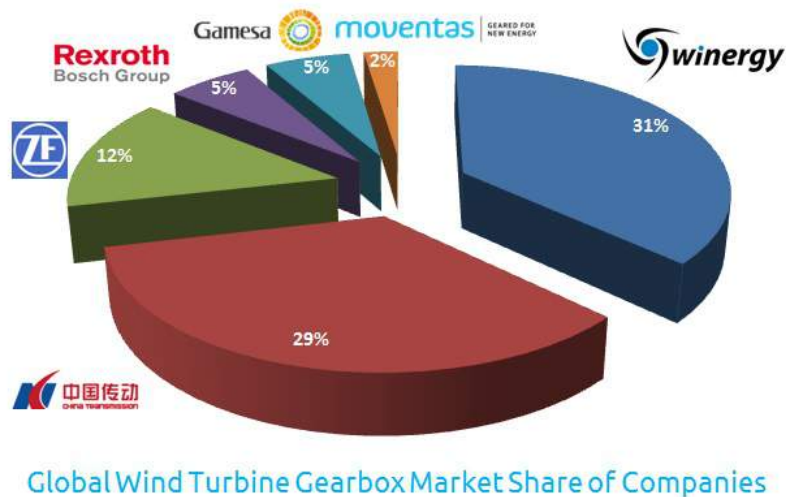


Figure 11.5: Wind turbine gearbox supplier market share [43]

The chart in figure 11.5 shows that 60% of the market is dominated by two suppliers. These two suppliers are Winergy (Germany) with 31% market share and China High Speed Transmission Equipment (China) with 29 % market share. Winergy was bought by Siemens in 2005, who are themselves a wind turbine supplier with a market share of 8.12% as shown in figure 11.3. The purchase of Winergy by Siemens was frowned upon by the other wind turbine manufacturers because most of them became reliant on gearboxes which are supplied by a subsidiary of a direct competitor. China High Speed Transmission Equipment have been increasing market share the last couple of years due to the increased demand of the wind turbines in China. ZF and Rexroth Bosch each with a market share of 12% and 5% respectively, supply transmission systems to various other industries and are trying to increase their market share in wind. They have been linked with GE. Gamesa with a market share of 5% is also a wind turbine producer. They make the transmission systems for their own products. The wind turbine gear supplier market is dominated by big players, which makes it difficult to enter as a new comer and compete with these companies, especially since most of them have special arrangements with established wind turbine producers. To succeed in this market a niche market strategy or a licensing structure would be preferable.

### 11.1.3. Value Proposition

The Archimedes drive offers advantages which will improve wind turbines performance. Three advantages will be highlighted that create the highest value for customers in this market: low weight and size, low wear and high efficiency.

The main problem with wind turbines, especially offshore turbines, is the weight and size of the system. For a 3 MW turbines, the combined weight of the nacelle and the blades is approximately 100 tons. In an offshore turbine this weight needs to be elevated at an average of 100m above the water, which drastically increases the installation and maintenance costs.[41] It has been found that for every kilogram of weight saved, the maintenance costs are reduced by a factor of three. The gearbox is approximately 10% of the total weight of the wind turbine. For a 3 MW offshore turbine, that would result in a weight of approximately 20 tons.[42] Using the Archimedes Drive, would reduce this weight by more than half, saving over 10 tons from the complete system. This weight reduction will create a snowball effect on the complete design, which further decreases the weight of the final product.

The transmission is one of the subsystems in the turbine which require most maintenance. Most damage is caused by particles contaminating the gear teeth. These particles get stuck in between the contact surface of the torque transferring gear teeth, resulting in a high localized stress, damaging the transmission.[5] Additionally, misalignment also increases the wear of the system over time. Although these problems have been improved over the years, they are still present and are a result of using gear teeth. The Archimedes drive will

decrease wear because there will not be a localized contact point on a single set of gear teeth, but continuous rolling contact. If a particle gets stuck in between the planet and the annulus, the spring like behavior of the drive will form around the contamination, distributing the load more equally and decreasing wear. This will have a positive effect on the life expectancy of the drive further reducing the maintenance costs.

High efficiency is also of great importance to wind turbines. Wind turbines are chosen based on the amount of power they generate, having a low efficient transmission results in less power being generated from the same wind conditions. Once more, the efficiency of current systems is limited by the performance of the gear tooth mesh. A poor mesh would result in unnecessary slipping over the gear teeth, increasing the friction, therefore decreasing the efficiency. The transmissions in wind turbines are designed with teeth that are shaped to reduce this slipping, trying to move closer to the efficiency of a bearing. The Archimedes drive only uses rolling contact to transfer torque, therefore it acts more like a bearing. This rolling contact will remove the slipping friction of the gear teeth, increasing the efficiency. Additionally, current wind turbine transmissions achieve the desired gear ratio in multiple steps. The higher the amount of steps the lower the efficiency. The Archimedes drive can achieve the desired gear ratio in a single step further increasing the efficiency. Overall, these three value propositions make it possible for the Archimedes drive to create great value for a wind turbine producer, differentiating itself from the competition.

## 11.2. Robotics

This section provides an analysis of the Robotics market. Since Robotics is a very broad Industry this analysis will focus mainly on the industrial robotics market, where the need for the technology is the greatest. First, a general overview of the market is given in section 11.1.1. With this overview an analysis of the competition is made in section 11.1.2. Finally this section is concluded with the value proposition of the Archimedes drive in the robotics market.

### 11.2.1. Market Background and Size

Industrial robotics is one of the key markets within robotics. These robots are used for manufacturing in automated processes. This is a large market with exceptional growth opportunities for Drive Technologies. The total size of this market in 2016 was over \$40 billion. Figure 11.6 shows the worldwide supply of industrial robots. As can be seen in the figure, the growth of the robotics supply increased 16% in 2015 and was expected to increase to 18% for 2017 with an average annual growth rate of 15% per year until 2020. The demand for industrial robots has accelerated during the past years and is expected to grow further due to the ongoing trend toward automation. Innovative technical improvements in this industry allows for automation to be applied towards new manufacturing processes each year. An additional driver of this growth is the growing popularity of 'Industry 4.0', by linking the physical factories with virtual reality. In 'Industry 4.0' robots will continue to automate dangerous and difficult jobs, taking it over from humans. Another growing trend is collaborative robots, these robots work alongside humans on the manufacturing floor.

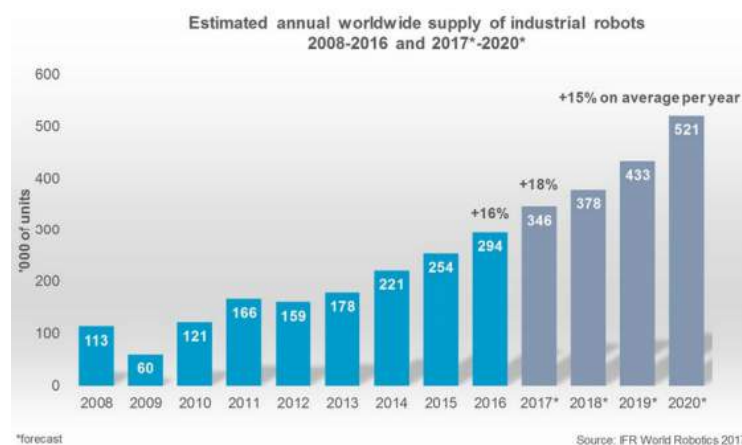


Figure 11.6: The growth in industrial robots market [44]

The industry which buys the most industrial robots is the automotive industry, followed by the electrical and electronics industry. The automotive industry had a share of 35% in 2016 with sales increasing by 12% from 2015. The main driving force however, are the electrical and electronics industry, which in 2016 had a market share of 31% and an increase in sales of 41% from 2015. The rising demand for new mass produced electronic products resulting in the need to automate production is the driving factor behind the large growth in demand in this Industry. Almost three quarters (74%) of all global industrial robot sales go to five countries. These countries are China (87,000 units), the Republic of Korea (41,400 units), Japan (38,600 units), the United States (31,400 units), and Germany (19,945 units). The largest is China with a market share of 30% in 2016, this is caused by the increased demand in vehicles and electronics for the growing middle class.[44]

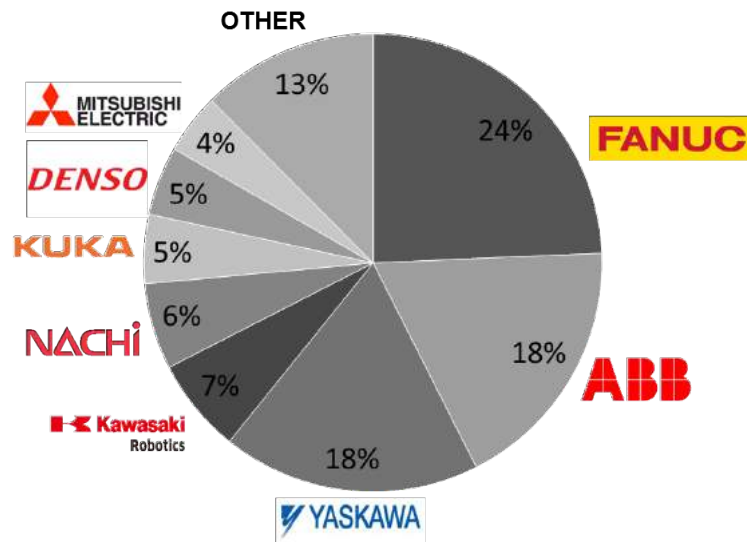


Figure 11.7: Market share of industrial robot manufactures [45]

The major companies supplying industrial robots are shown on the pie chart in figure 11.7. The chart shows that the industrial robotics market is a concentrated market. The three largest companies are FANUC, ABB and Yaskawa and they take up roughly 60% of the installed base of industrial robots worldwide. Additionally, it is interesting to note that almost all of the large companies in the industrial robotics market are Japanese. Only ABB and KUKA are based in European. Although KUKA originally a German robotics company was acquired for a reported sum of \$5 billion in 2016, by the Midea Group, a Chinese manufacturer of home appliances.[46]

An emerging and very interesting segment of the industrial robotics market is that of collaborative robots (cobots). These robots are also called ‘cobots’, as shown in figure 11.8. These robots are lightweight and compact industrial robots that can be deployed for multiple applications and can safely work alongside humans. This market, which had an estimated current size of \$110 million in 2015, has a forecasted CAGR of more than 60% per year between 2016 and 2022. It is estimated that the total market size of cobots will reach \$3.3 billion by 2022. Currently, they are mostly used in the automotive industry, but cobots are also on the rise in industries such as metal and machining, furniture and equipment, and food and beverages. [47]

The strong growth in this market segment is a result of the adoption of cobots by small- and medium sized enterprises (SMEs). Collaborative robots have a lower price than traditional industrial robots, which makes them affordable for smaller companies. Furthermore, the need for high precision in manufacturing and increasing focus of OEMs and consumers on safety of operations, is also expected to increase growth of collaborative robots. Cobots are smaller and lighter than traditional robots and often apply advanced technologies, such as collision detection and torque sensing. This makes them able to perform very precise tasks and safe to assist people working in a production factory.



Figure 11.8: Collaborative robots [60]

The drives used in robotics are mainly used to reduce the speed of the input shaft, increasing torque. That is why within the robotics industry, drives can be referred to as "speed reducers". Speed reducers are one of the three core parts of industrial robots, the other two are servomotors and control devices. The speed reducer accounts for around 36% of the robot's total cost. Looking at the market size for robotic hardware in 2016 (which is \$12.9 billion), the estimated total market value of speed reducers in industrial robots is approximately \$4.6 billion. Robots are used for many different manufacturing procedures, meaning that the overall speed reducing gear ratio can vary from 50 to 500. The higher the ratio the more accurately the robot can move although the electric engine supply the input velocity will need to rotate faster for the same given movement.

### 11.2.2. Competitors

The global demand for speed reducer components was estimated at 1.36 million units in 2017 and this value is expected to double to 2.72 million units in 2025. The rapid growth can be contributed to the sharp rise in demand in industrial robots, explained in section 11.2.1. As stated previously, the market in China is developing rapidly, both in the demand for robotic speed reducers and as with regards to players producing these drives. China was previously heavily dependent on foreign companies to supply speed reducers, importing 75% of them. However, by the end of 2016 more Chinese companies had the potential to develop their own speed reducer technology, resulting in a fast growing domestic market. Despite this, the robotics speed reducer market is still dominated by non-Chinese companies. An overview of the market share for the drive market in industrial robotics can be found in figure 11.9.

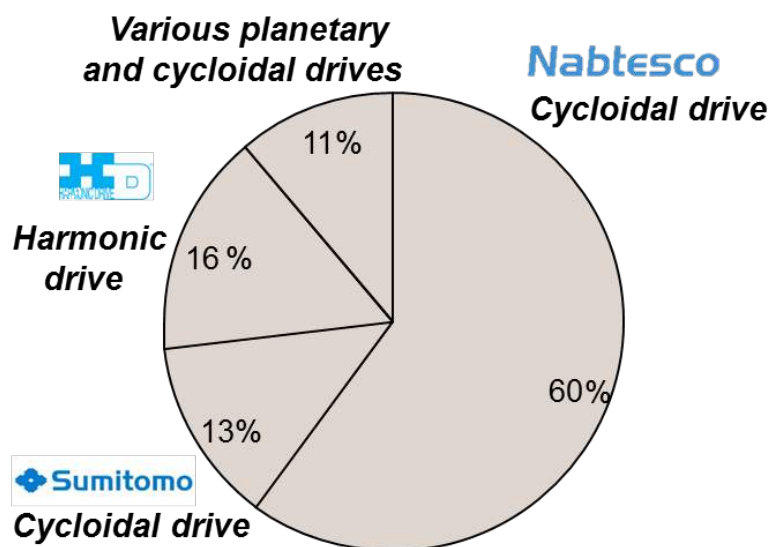


Figure 11.9: Market share of drive manufactures [45]

The pie chart in figure 11.9 shows that there are three dominating companies in the industrial robot speed reducer market. Combined they amount to a total market size of just under 90%. The largest company is Nabtesco which mainly produces cycloidal drives, with a market share of 60%. Harmonic Drive, a strain wave gear producer, comes in second place with a market size of 16%. The last of the three, Sumitomo, also a cycloidal drive supplier, has a market share of 13%. The remaining 11% is covered by numerous small planetary and cycloidal drive manufacturers. Nabtesco, Harmonic drive and Sumitomo are all based in Japan, while the companies that make up the other 11% are situated all over the world. The largest three also all rely on relatively old core technology, meaning that they all use core patents which are no longer protected. This incentivizes the newly formed Chinese speed reducer manufactures to mass produce lower quality versions of the products supplied by the big three.

From the big three, Nabtesco focuses primarily on the production and distribution of speed reducers and motion control with revenues of \$1.7 billion per year. Harmonic Drive, primarily focuses on the production and distribution of their strain wave speed reducers technology with a revenue of \$250 million per year. Lastly, Sumitomo Drive Technologies, part of Sumitomo Heavy Industry which is owned by the Sumitomo Group (Mazda, NEC, Mitsui), has a revenues of more than \$800 million per year. Due to a lack of new breakthrough technologies, these top three have controlled the industrial robotics market for numerous years. As a new comer to this market it would be difficult to compete with the economies of scale from the large manufactures, unless a patent can be used to protect the technology. If a patent is present, a preferable course of action would be to focus on specific sector with high growth potential in industrial robotics, for example, collaborative robots. Once focused, the knowledge and capital attained in this market segment can be used to further expand into other industrial robot applications.

### 11.2.3. Value Proposition

There are many advantages to the Archimedes Drive which will improve industrial robots. Three of the most important improvements are discussed, provided with reasons on how they add value to the customer. The advantages to be discussed are a higher torque density, zero backlash and no need for lubrication. Each of them improve the performance of robots, providing a competitive advantage for robot manufacturer.

The first important advantage is higher torque density. This directly adds value for the customer. Determining exactly how it adds value depends on the needs of the end-user of the robot. This end-user could be an automotive company that welds vehicles using large robotic arms, or it could be an electronics company that uses collaborative robots to assist workers in the assembly of electronic devices. The increased torque density that the Archimedes drive provides to robotic applications offers value to the user of the robot in two different ways; a reduction in cycle time and a reduction in the overall weight of the robot. A cycle time is the amount of time needed for a robot to complete a task. Being a higher torque density speed reducer, the Archimedes drive can reduce the cycle time for a given robot by 40%. This is possible because if a more powerful drive with the same size as a previously used drive is installed in the robot, it will result in a higher production output for a given time than before. This means that companies using the robots with the new drive system will have more production at a lower cost. The higher torque density can also decrease the weight of the robot by 10%. This is simply because more torque can be supplied by a smaller package, making the drive smaller and lighter than before. This then directly correlates with a more compact and lighter robot. Making the robot more compact would allow it to operate on a smaller scale and to do tasks that it was previously not able to do. For example, the assembly of very small computer chips by collaborative robots. Additionally, a lighter robot would result in less mass moving around decreasing the momentum of the system, making it safer for people to work alongside it.

As stated in section 10.2 zero backlash is a unique advantage that the Archimedes drive offers which also directly translates to customer value. As explained previously, since the Archimedes drive does not have gear teeth, the recoil caused by the minor spaces between the teeth in a regular gear is no longer present. This ensures that robots become more accurate and improve their repeatability. Repeatability is the ability to exactly recreate a specific motion for numerous cycles. This is one of the most important design requirements for collaborative robots because cobots are programmed through a human hand guiding it, which they will remember and will need to repeat for multiple cycles. Accuracy is also improved drastically with zero backlash. This will help greatly in assembly procedures like robotic welding or painting, resulting in a straighter movement of the robot arm, reducing the margin for error in production. This then translates directly into

lower cost for the final consumer due to a decrease in error.

The final important advantage is that the Archimedes drive does not need any lubrication to operate. This adds value for the customer in two different ways. Firstly, the risk of oil leakage is completely removed. Current transmissions have to rely on seals to keep the lubricating oil from contaminating the work floor, however the seals are never 100% effective. That is why certain robots use specific lubrication to ensure that if a leakage occurs it will not damage production. This can be seen in robots handling food, these robots use food grade oil so that in case of a leakage, the food product being handled by the robot can still be eaten. Using this oil however, comes with increased cost and lower performance of the robot. Another example is if a robot needs to operate in a clean room. If there is any leakage, the clean room will be contaminated and the product being manufactured must be discarded. Not requiring lubrication would greatly relieve this concern. The second value addition is that when there is no need for lubrication this will result in less maintenance requirements, decreasing the overall maintenance costs and downtime of the robot.

Overall, these three advantages allow the Archimedes drive to create value for the robotic industry.

### 11.3. Electric Vehicles

In this section an analysis of the transportation market is performed. The transportation market is however a very large. This analysis will focus on an application which has the highest demand for the Archimedes drive, namely electric vehicles (EV). A general overview of the market is given in section 11.3.1. With this overview an analysis of the competition can be made in section 11.3.2. Finally, this section is concluded with the value proposition of the Archimedes drive in the EV market.

#### 11.3.1. Market Background and Size

The EV market is growing each year and can be seen as a key industry for the Archimedes drive. The EV market, also known as plug-in electric, is divided into two sections; battery electric vehicles (BEVs) and plug-in hybrids (PHEVs). BEVs are all-electric vehicles that only run on batteries which are charged at stations and PHEVs combine internal combustion engines with electric battery power to run the vehicle (PHEVs). Both systems require the use of gears to transfer torque from the electrical engine to the wheels of the car. The global sales of light-duty plug-in vehicles can be seen in figure 11.10 and the top selling brands for Europe can be seen in figure 11.11.

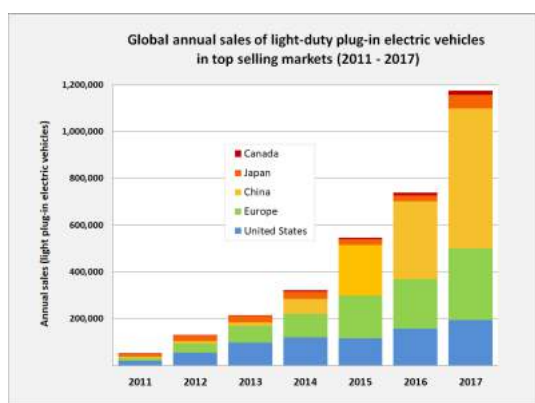


Figure 11.10: Annual sales EV industry [48]

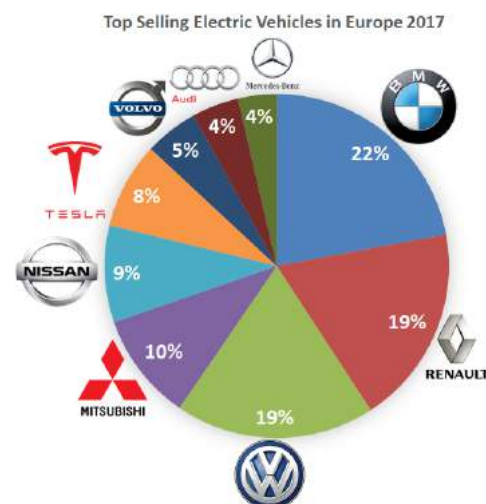


Figure 11.11: Top Selling EV in Europe by brand [61]

The plot in figure 11.10 shows that the EV market is growing rapidly. In 2011 less than 50,000 EVs were sold worldwide, this value grew to almost 1,200,000 in 2017.[48] The largest growth took place in China, the sales in China account for around 50% of the total sales in EVs. In this market 96% of EVs sold are domestically produced.[49] The reason for this large increase in Chinese market is because of government incentives. China is trying to overcome their pollution problem by reducing the amount of internal combustion vehicles on the

road. These incentives include purchase subsidies and implementing power stations. The second biggest market is the European market with around 28% of global sales. Government incentives in Europe as well as the consumers desire for a "cleaner world" are the main reasons for this growth. Despite the steep growth, EVs only account for 1.3% of total market share in new car sales for 2017.[50]

The top selling brands in Europe and their market share are given in figure 11.11. As can be seen there are three brands which own over 50% of the EV market. These brands are BMW with 22%, Renault with 19% and Volkswagen with 19%. Each of these brands target a different market segment. BMW targets the high-end market, Volkswagen targets the middle market segment and Renault the economy segment. Renault produces Europe's second best selling electric car the "Renault Zoe", as it sold 92,000 units in 2017. The best selling EV in Europe in 2017 is the "Mitsubishi Outlander P-HEV", as it sold 100,000 units. Audi which has a market share of 4% is also part of the Volkswagen group and is planning to compete directly with BMW. Due to the growing demand in EVs, more companies are starting to introduce their own electric models.

In the transmission market for EVs rapid growth is also expected. In 2015 around 315,340,000 transmission units for EVs were sold, this value is expected to become 2,143,850,000 units by 2020. This is a growth of rate of around 47% per year. [51] The gear systems used in this industry can be divided into two categories, single stage gear and multi-stage gear systems. Single stage gear systems, which had a market share of 98% in 2015, use a gearbox with one gear to alter the speed and torque between the electric engine and the rotation of the wheels. The multi-stage gear system use a numerous amount of gears, and are comparable to those used in standard combustion engines. The reason why EVs heavily rely on the use of single-stage gears is because they have a much larger rotational velocity range compared to standard combustion engines. Combustion engines have a narrow band where the engine operates at maximum efficiency, the multi-stage system allows the vehicle to remain in that narrow band across different speeds. Since electrical engines have a much wider efficiency band multi-stage systems are not required. This bring a multitude of benefits including reduction in transmission weight and complexity. The average maximum rpm of an electric engine is 20,000 rpm requiring a speed reducing gear ratio of 15-20. This value depends on the operation of the vehicle. Multi-stage systems in EVs are becoming more popular as the operating conditions for EVs start to broaden, however single-stage systems will remain dominant into the future.

### 11.3.2. Competitors

The EV transmission market is a relatively new market with large growth potential. Due to this large potential, developed automotive Original Equipment Manufacturers (OEM's) are investing heavily in this market. The top-tier automotive electric transmission OEMs are GKN, Borgwarner, ZF and Anotonov.[51] Each OEM has there own technology and aim at a specific market segment.

GKN has been manufacturing electric axles since 2002. Electric axles are mainly used in hybrid vehicles and are installed on the rear axle of the car, driving the rear wheels with electric power while an internal combustion engine powers the front wheels. They are fully contained units, made out of bearings, shafts, pinions and differential gearing and mostly constructed out of a high-strength and lightweight material. With its experience GKN is currently manufacturing electric transmissions for a wide range of vehicle applications. Their technology can transmit power up to 300 [kW] and produce gear ratios of up to 14. They have also started to develop a dual-stage transmission system to increase the efficiency of EVs.[51] Borgwarner provides contemporary robust transmissions that provide high torque, making it a reliable choice for the customers. They currently focus on increasing the range of EVs by increasing the transmission's efficiency.[51] ZF focuses on driving dynamics and safety by implementing intelligent torque distribution transmissions. This will allow the transmission to support the driver during steering by generating a yaw moment in the desired direction.[51] Antonov provides both multi-speed and single-gear transmission solutions. They are currently supplying a 6-speed automatic transmission which would allow EVs to be used for more applications.[51] In addition to these top suppliers there are numerous other companies which are trying to get a foot hold in this market.

Just like the traditional automotive transmission market there is high competition in this market. However, since it is a relatively new segment of the automotive industry new ideas have the potential to succeed. The auto manufactures are looking for a competitive advantage and are willing to work with newer companies which have an innovative solution. As a new player in the automotive world, a company can differentiate themselves by having a unique selling point with which they are able to attract new customers. However, the

transmission must be robust enough to withstand the strict performance requirements.

### **11.3.3. Value Proposition**

The EV market is growing rapidly, putting more demand on the quality of the transmission. The Archimedes drive excels in certain requirements which would set it apart from what is currently available on this market. These requirements would allow EVs to increase their overall performance or lower their cost, adding value for the customer. The three main improvements that the Archimedes drive has over the competition are decrease size/weight, increased efficiency and lower production cost.

Decreasing the weight/size of the drive is one of the main improvements that the Archimedes drive can add to EVs. Most performance and cost factors are directly related to the weight of the complete system. A lower weight increases the acceleration, braking and turning characteristics of a vehicle because the car has less momentum that needs to be overcome by the engine, brakes or traction systems. The Archimedes drive can offer a total reduction in weight of 50% in the transmission compared to the competition, further improving the previously mentioned characteristics. A growing trend in the electric automotive world is that each wheel is supplied by an independent engine and transmission system. This allows the vehicle to have independent wheel torque vectoring. This does however, make the system heavier because four engines and transmissions are required. A reduction in weight in the transmission by 50% would result in a large overall change in weight once four drives are taken into consideration. The decrease in size is also beneficial for EVs because passenger comfort and safety are becoming more important in today's cars. Electrical engines are smaller compared to internal combustion engines, saving room and allowing more space inside the vehicle for other systems. Currently, the transmission system is the limiting factor in the power-train when it comes to its overall size. If the Archimedes drive is used, space can be saved further leaving more room for other systems.

One of the biggest concerns with EVs is the range. The maximum range of current EV is around 500 km. In order for more of these vehicles to be sold, the range needs to increase. The efficiency is directly related to range; the higher the efficiency, the more of energy (stored in the battery) is used to power the rotation of wheels, meaning that the range can increase. A small increase in efficiency can have a large impact in the range of the vehicle over a long period of time. The Archimedes drive offers that increase in efficiency due to its rolling contact behavior. As explained in section 11.1.3, the efficiency decrease of transmissions used in EVs is caused by the gear tooth mesh. Having a mesh always results in slipping over the gear teeth before contact is made, increasing the friction, therefore decreasing the efficiency. Having rolling contact behavior removes this slipping increasing efficiency. Additionally, (all be it theoretically) the Archimedes drive can offer a two-speed transmission by changing the input between the two sun wheels (Idling and Input Sun). This would allow it to have one higher gear ratio for low speed conditions and one lower ratio for high speed conditions. An electric motor has a wider power operating range compared to internal combustion engines, however their efficiency still drops to 60-70% at low speeds. Having a dual-speed transmission system would allow the engine to operate less in those low ranges, increasing the efficiency over its full range by 15%.

Costs are an important factor in the automotive industry. In order for EVs to be adopted by the mass market their cost must be comparable to that of current internal combustion vehicles. The biggest factor which reduces the cost of a product is economies of scale, the cost of a single unit decreases as the total number of units produced increases. The cost of the Archimedes drive can be sharply reduced once it is produced on a large scale. This is because no complex machining operations are required to make the product. In current transmission system one of the most complex parts is the production and assembly of the gear teeth. These two aspects are relatively less affected by economies of scale because it always requires the use of a complex procedure. The Archimedes drive on the other hand, only uses rotating cylinders, making it simple to produce once the machines are in place and the production procedure is set.

To conclude, these three advantages allow the Archimedes drive to create value for the EV industry.

## **11.4. Market Penetration Strategy**

With the market analysis the market penetration strategy can be determined for the Archimedes drive in the three chosen markets; the wind turbine, robotics and electric vehicle market. Each market requires a different strategy depending on the competition, barrier of entry and market potential.

The wind turbine market requires the largest investment in order to produce the gearbox. A single gearbox, due to its large size and demanding operating environment, is priced around \$10,000-\$100,000. The price variation depends on the final size and power of the wind turbine. When comparing these transmissions to other industries, they require more material to produce and have a more complex manufacturing and assembly procedure. The larger size of the gearbox makes assembly more complicated as special tools are required to hoist, move and fix the drive's components. In smaller and lighter drives for other industries this can be done by a single individual. All these aspects would require a larger initial investment to design and produce a drive for this industry. Looking at the competitors, a large percentage is owned by wind turbine producers or have a special agreement with them, making it difficult to enter as newcomer. Taking all points into account, licensing the technology would be a good course of action. This would allow the Archimedes drive to take advantage of the wind turbine gearbox producer's assembly tools and market connection to penetrate the market without the risks of producing the drives internally. This would lower the profits received from this industry but would allow more energy to focus on another industry with a lower barrier of entry.

The robotics industry is a market the Archimedes drive would be able to penetrate well. In this market, the price of a speed reducer is in between \$100-\$1500. That is significantly lower than the wind turbine industry. The price of the drive depends on the the type of speed reducer required(strain-wave, cycloidal or planetary), the gear ratio and the amount of torque going in the system. These drives are relatively small and require less expensive machinery to assemble, as most movement operations can be done by hand. Since larger volumes are produced compared to wind turbines the benefits of economies of scale are more pronounced. In this market, robotics companies are more willing to work with new technologies as they are too dependent on the big-three manufactures. This makes it easier for a new player to compete in this industry. Additionally, since the Archimedes drive technology is protected by a patent, the competitors do not have the legal right to produce the drive. This greatly lowers the risk of a competitor taking the technology and using their manufacturing process to out-produce and out-compete internally developed drives. These aspects would make it possible for the Archimedes drive to be developed in-house and sold directly to customers within the robotics industry. This would allow for more profit compared to a licensing strategy but would require a higher investment.

The strategy used for EV market can be seen as a mix between the other two industries. The price of a gearbox is positioned in between that of robotics and wind turbines (\$1,500-\$5,000). Currently, electric vehicles mostly use technology comparable to planetary drives with a single gear. The cost and machinery required to produce the transmission is comparable to the larger drives produced for robotics. Looking at the market and the competition, this is a relatively new segment of the automotive industry. This means that customers are more willing to work with new suppliers and are trying to find new innovative transmission solutions. However, there is a growing trend towards using a multi-stage transmission system, which adds more complexity to the design and manufacturing process of the drive. The Archimedes drive, at this stage, is not sufficiently developed to implement a multi-stage system, even though it is theoretically possible. Implementing this would result in further investment in research and development, rather than selling a product that is already available. This is the main reason why the transportation industry should not be the main focus market for the Archimedes drive, but rather seen as a potential market that can be penetrated once the technology is further developed. Once development has progressed enough, the market can for instance be penetrated by becoming an OEM, competing with current market suppliers by selling better performing transmission technology.

With this market analysis it can be concluded that the primary target market for the Archimedes drive is the robotics market. The robotics market makes it possible to enter with a lower barrier of entry, decreasing initial investment. The Archimedes drive would be able to be developed in-house and sold directly to robotics manufacturers. During this process the technology will mature further, allowing for incremental improvements. Revenue generated in this process can be invested in developing a multi-stage version of the drive. Once developed the EV market can be penetrated. In the wind turbine market development partners can be found to whom a license will be sold to. Overall, if these strategies are followed the Archimedes drive has the highest chance for market success.

# 12

## Business Plan

To ensure the market success of the Archimedes drive a business development strategy must be made to determine which direction the product should go. The three markets which were discussed in chapter 11 are analyzed to determine which strategy should be applied to them. The two main strategies that will be discussed are producing the drives and licensing the technology. Production will be discussed in section 12.1 and licensing in section 12.2. Additionally, the intellectual property strategy is discussed, in section 12.3.

### 12.1. Producing the Technology

Producing the drive will result in the largest revenue, however this requires a larger initial investment. The production of a drive includes the design and assembly of the Archimedes drives. This drive will then be directly sold to a customers in a specific industry. Due to the greater performance and lower production costs both the high and low end of the market can be targeted. However, to be profitable in the low end market the production of the Archimedes drive needs to take advantage of economies of scale. Using economies of scale to lower the production cost of the drive requires a large initial investment in manufacturing equipment as expensive manufacturing machines will need to be used, increasing the financial risk if the technology does not sell. Additionally, since this technology is relatively new, some of the technical claims will still need to be proved for a specific industry. This means that if the drive were to be mass produced, there is no sufficiently solid and proven technical foundation to ensure approval by the market. That is why it would be beneficial to start with the design and production of custom made high performance drives, meaning that this technology will penetrate at the high-end of the market.

In this market segment early adopters can be found that are looking for the specific benefits that the Archimedes drive can offer. Using these early adopters a co-development phase can be started where the drives will be built in close cooperation with the customer. In this phase, all of the industry's specific technical requirements will be identified and applied to the Archimedes drive. After those requirements have been met, new customers will be more willing to implement this new technology in their systems, resulting in greater market adoption. Using this growing adoption rate, more investments can be made in the production of the drive, increasing the amounts of individual units produced, resulting in a lowered cost per unit. This would allow the Archimedes drive to gradually increase its market share by increasing the focus within a specific industry due to a lowered product cost. In the beginning phases the production of the individual components within the drive can be outsourced and the assembly can be done in-house. Doing this allows for a reduction in initial costs, as specialized manufacturing equipment is not required, while still retaining the core of the intellectual property in-house. An example of the cost of production for the individual components of the drive in the robotics market can be found in table 12.1.

Table 12.1 shows the costs of all the components as a function of volume. As shown the cost of a single drive at low volumes is around \$780. This is comparable with the current costs of high end drives on the market. The Archimedes drive is relatively simple compared to current available technologies, the costs per unit decrease greatly as the number of units produced increases. The costs could be as low as \$171 per unit with large enough volumes, which is less than 25% of the initial costs. At large volumes the benefits of the drive are

clear as the same performance requirements can be attained as current technologies, but with a fraction of the costs.

Table 12.1: Estimated production costs [62]

<b>Volume (Thousand Units)</b>	<b>0-0.1</b>	<b>0.1-0.5</b>	<b>0.5-5</b>	<b>5-50</b>	<b>50-500</b>	<b>500+</b>
<b>Total Component Costs (\$)</b>	<b>757</b>	<b>654</b>	<b>492</b>	<b>370</b>	<b>260</b>	<b>160</b>
Flexrollers (\$)	231	231	221	150	100	50
Sun Wheels (\$)	58	55	55	45	35	25
Annuli (\$)	68	68	66	55	45	35
Bearings/Screws (\$)	200	150	75	60	40	25
Housing/Carrier (\$)	200	150	75	60	40	25
<b>Assembly/Shipping Costs (\$)</b>	<b>30</b>	<b>15</b>	<b>13</b>	<b>11</b>	<b>11</b>	<b>11</b>
Assembly (\$)	20	10	9	8	8	8
Shipping (\$)	10	5	4	3	3	3
<b>Total Costs (\$)</b>	<b>787</b>	<b>669</b>	<b>505</b>	<b>381</b>	<b>271</b>	<b>171</b>

Taking those costs into account, the Archimedes drive can be sold at the same price as the competitors in the high-end segment of the market. In the high-end market segment of the robotics market, the price of a drive can vary between \$1,000 to \$1,500 per unit. The price depends on the type of application and operating condition the robot will be in. Each robot has approximately 4-6 joints, all using an individual speed reducer, meaning that there is a total of \$4,000 to \$9,000 worth of drives in a single robot. In the robotics transmission market, the Archimedes drive would be competing directly with strain-wave gears.

Making a drive with better performance criteria compared to strain-wave gears allows a premium price of the Archimedes drive. This would allow for slightly higher revenues per robot. Notwithstanding this increase in price, the production cost is less compared strain-wave gears, allowing for a larger profit margin. If the volumes become high enough the profit margins could be up to 70%. This increased margin would allow the Archimedes drive to gradually enter the low-cost segment of the market. Additionally some performance characteristics can be reduced, allowing a further increase in profit margins as high as 90%. This could make drives drastically more affordable, greatly lowering the final costs of robots used in the mass consumer and light-industry markets.

## 12.2. Licensing the Technology

In some markets, like the wind turbine industry it would be more beneficial to license the technology. This would give an additional manner to generate revenue without the need for added investment. It would also allow the possibility to focus on more than one core market. The drive requirements in the wind turbine industry are different from robotics, therefore considerable financial effort will be needed to develop the technology specifically for that market.

In order to make a feasible license agreement an overview of a how much value a new technology adds to the complete system must be determined. Using that value the cost savings or revenue can be determined which can be used to calculate the license payments. An example to determine the license payments for wind turbines is by using the cost per kilo Watt (kW). A wind turbine transmission costs around \$50 per kW. The Archimedes drive would be able to be produced for around \$30 per kW. This saves the manufacturer about \$20 per kW. Taking a license fee of 20% of the value that the manufacturer is saving would amount to \$4 per kW. This means that if a transmission for a 3 MW turbine is produced a licenses fee of \$12,000 per transmission can be charged. This rule can be applied to a wide range of wind turbine transmissions. Another form of a license agreement is to charge a fixed fee per year. In order to ensure a constant revenue stream it would be beneficial to have a combination of a fixed and variable fee. At the start of the license agreement the fixed fee could be the main the source of revenue, and then as the production increases the variable fee will increase with it, making that the main source of revenue over time. This strategy can be applied to numerous other non-core industries to ensure a constant stream of revenue.

### 12.3. Intellectual Property Protection

The intellectual property (IP) of the Archimedes drive technology must be protected to ensure a successful market penetration. Currently, the core technology has been approved in the Netherlands and is in the PCT phase. A patent protection strategy must be determined to further protect the intellectual property. The next step, once the PCT phase has been passed for the core patent, is to file the patent for all countries which are capable of producing drive technology. These countries include most of the EU, the US, Canada, Australia, New Zealand, India, China, Japan and South Korea. Filing a patent in those countries insures IP protection for 20 years, however it does require the disclosure of a detailed overview of the technology to that country. This could be problematic for countries which do not enforce international patents as strictly, like China.

China is an important market for the Archimedes drive but requires special attention with regards to patent filling. In the market analysis (chapter 11), it was determined that China is the largest market for wind turbines and electric vehicles, while also being the fastest growing market for robotics. Large potential is possible in China with the emergence of new high-tech Chinese companies, potential customers of the Archimedes drive. However, as stated in the robotics market research (section 11.2), Chinese drive manufactures are also on the rise. This in combination with strict government regulations on foreign technology make it difficult to compete in China. Currently, these manufactures produce drives using expired patents technologies, focusing on high volume and low cost technology. These manufactures are protected by the government and have the manufacturing capabilities, therefore it would make sense to partner with one these companies in order to enter the Chinese market. A license agreement for the Chinese market can be agreed, giving a specific party rights to manufacture and sell the technology domestically. However, technology that has not been filed must remain a trade-secret to prevent it from being produced without IP protection. Apart from the Chinese market the Archimedes drive can be produced and distributed in-house.

Looking at IP protection, more patents need to be filed to ensure that no competitor can benefit from the technology. With the core patent multiple defense patents will need to be filed. These defense patents include possible work-around scenarios which apply a part of the working principle of the Archimedes drive to current transmission systems. With these defenses in place, manufactures would not be able to produce any comparable technology, giving exclusive right to the Archimedes drive. Despite this, patents do not exclude anyone from producing the patented technology. The main protection provided by a patent is that it will allow the patent holder to claim the technology as theirs (in court), when used by another company who hasn't paid any license fees to the patent holder. Any legal dispute in this context can and will require a (significant) amount of money. Because such financial means are unavailable in the starting phase, it will be difficult to defend the technology as belonging to the patent holder. Therefore in some cases it is more beneficial to rely on trade-secrets.

Taking the above into account, the best way forward for the Archimedes drive can be determined by the following steps for IP protection:

1. File core-patents in all industrial countries around the world;
2. Write and file defense patents to insure no work-around technology can be developed by competition;
3. Start negotiations with potential Chinese partner for the Chinese domestic market;
4. Rely on strict trade-secret until a patent can be filed;
5. Create a patent defense budget for legal costs;
6. Continually analyze current technological development to determine best IP protection.

If these above mentioned steps are used, the Archimedes drive will have the strongest patent protection.



# 13

## Conclusion Annotation Entrepreneurship

This entrepreneurship annotation part of the thesis focused on the business aspect of the technology used in the DOT wind turbine. The technology is novel and has the possibility to be applied in multiple industries. In chapter 10 an analysis was conducted to see how it compares to available technologies on the market. It was concluded that the drive has multiple attributes which sets it apart from the competition. Including cost savings and performance improvements, allowing current systems using this technology to be improved further.

Using those advantages a market research was conducted in chapter 11, to determine the best industries in which to sell the Archimedes drive. Multiple industries were discovered and the best three were chosen for a more detailed market analysis; wind turbine, robotic and electric vehicle industries. Each of these industries consists of different companies as possible clients who require different versions of the drive. An analysis of the competition was also conducted to see what was already on the market and if it was possible for the Archimedes drive to differentiate itself. Using that attained information a value proposition of the drive per industry was made. Looking at all the value propositions a general market penetration strategy was determined in chapter 11.4, concluding that the in-house production for the robotics industry should be performed first, then followed by the electric vehicle industry. Finally, for the wind turbine industry, a licensing strategy should be used.

Lastly an overview of the business plan was made in chapter 12. In this section the strategy used for in-house production and licensing was discussed. In the production of the technology, it was determined that the high-end robotics market should be targeted first. Once a sustainable amount of revenue is generated, more investments can be made in production to achieve economies of scale, allowing the drive to go after the low-end robotics market. In licensing the technology, a feasible strategy would be to figure out how much the technology is worth and base the license agreement on that. Finally, an IP protection strategy was determined. In this IP strategy it is important to focus on special protection in China and ensure that multiple patents are filed to prevent work-around scenarios. Overall, looking at this entrepreneurship annotation part it can be concluded that there is market potential for the Archimedes drive and it has the possibility to positively change multiple industries if the given steps in this part of the thesis are followed.



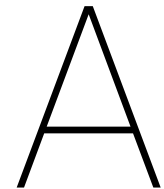
# Bibliography

- [1] P. Dvorak, *Extreme torsional loads damage more than wind turbine gearboxes*, Windpower Engineering and Development, <http://www.windpowerengineering.com>, (2016).
- [2] K. Zipp, *Gears and Gearbox 101*, Windpower Engineering and Development, <http://www.windpowerengineering.com>, (2012).
- [3] K. Zipp, *Wind Turbine Types*, Green Collar Job, <http://www.greencollarjobtraining-free.com>, (2010).
- [4] P.W.Carlin, A.S.Laxson, E.B.Muljadi, *he History and State of the Art of Variable-Speed wind turbine Technology*, Wind Energy, (2003).
- [5] Sheng, Shuangwen, *Monitoring of Wind Turbine Gearbox Condition through Oil and Wear Debris Analysis: A Full-Scale Testing Perspective*, Tribology Transactions, (2016).
- [6] Y. Feng, Y. Qiu, C. Crabtree and P.J. Tavner, *Monitoring wind turbine gearboxes*, Wind Energy, (2012).
- [7] A.J. Laguna, *The Delft Offshore Wind Turbine Concept*, Tu Delft, DUWIND (2009).
- [8] T. Verschoor, *WGR Design Report*, IMSystems, (2016).
- [9] J. Schorsch, *Patent: Compound Planetary Friction Drive*, Tu Delft, Delft (2014).
- [10] Y. Qiu, Y. Feng, J. Sun, W. Zhang and D. Infield, *Applying thermophysics for wind turbine drivetrain fault diagnosis using SCADA data* ISSN, Journal of IET Renewable Power Generation (2015).
- [11] T.A. Harris, *Rolling Bearing Analysis*, 4th Edition, (2001).
- [12] J.P. Holman, *Heat Transfer*, 9th Edition, (2002).
- [13] S. Lee, M.M. Yovanovich and K. Jafarpur, *Effects of Geometry and Orientation on Laminar Natural Convection From Isothermal Bodies*, Thermophysics and Heat Transfer, Vol. 5, (1991).
- [14] W.R. Smythe, *Charged Right Circular Cylinder*, American Journal of Physics, Vol. 27, (1956).
- [15] S.W. Churchill and R.U. Churchill, *A Comprehensive Correlating Equation for Heat and Component Transfer by Free Convection*, , Vol. 21, (1975).
- [16] J. Brandlein, P. Echmann, L. Hasbargen and K. Weigand, *Ball and Roller Bearings Theory, Design and Application*, 3rd Edition, (1999).
- [17] A. Palmgren, *Ball and Roller Bearing Engineering*, 3th Edition, SKF Engineering Burbank, Philadelphia, (1959).
- [18] SKF, *Deep groove ball bearing 61804*, <http://www.skf.com/group/products/bearings-units-housings/ball-bearings/deep-groove-ball-bearings/deep-groove-ball-bearings>, (2018).
- [19] S. Deng and Q. Jia, *Rolling Bearing Design Principle*, China Standards Press, Beijing, China, (2008).
- [20] T.A. Harris and M.N. Kotzalas, *Rolling Bearing Analysis*, John Wiley and Sons Inc., New York, USA, (2010).
- [21] X. Li, Y. Lv, K. Yan, J. Liu, and J. Hong, *Study on the influence of thermal characteristics of rolling bearings and spindle resulted in condition of improper assembly*, Journal of Applied Thermal Engineering, (2017).
- [22] F. Ma and Z. Li and B. Wu and Q. An, *An accurate calculation method for heat generation rate in grease-lubricated spherical roller bearings*, Proceedings of the Institution of Mechanical Engineers, Part J: Journal of Engineering Tribology, Massachusetts, (2016).

- [23] A. Azarkhin, *Steady-state temperature in a roll subject to surface heating and convection cooling*, Journal of Engineering Mathematics, (1994).
- [24] A. Wang and J. Wang, *Temperature distribution and scuffing of tapered roller bearing*, Chinese Journal of Mechanical Engineering, (2014).
- [25] G. Eckert, *Introduction to the Transfer of Heat and Mass*, McGraw-Hill, New York (1950).
- [26] M. Jakob, G. Hawkins, *Elements of Heat Transfer and Insulation*, McGraw-Hill, New York (1950).
- [27] G. Korn, T. Korn, *Mathematical Handbook for Scientists and Engineers*, McGraw-Hill, New York (1961).
- [28] Wolfram Mathworld, *Circle-Circle Intersection*, (2017), [mathworld.wolfram.com/Circle-CircleIntersection.html](http://mathworld.wolfram.com/Circle-CircleIntersection.html), 2018.
- [29] Wolfram Mathworld, *scipy.optimize.fsolve function*, (2014), <https://docs.scipy.org/doc/scipy-0.14.0/reference/generated/scipy.optimize.fsolve.html>, 2018.
- [30] Computational Statistics in Python, *Algorithms for Optimization and Root Finding for Multivariate Problems*, (2018), <https://people.duke.edu/~ccc14/sta-663/MultivariateOptimizationAlgorithms.html>, 2018.
- [31] R. Fletcher and M. J. D. Powell, *A rapidly convergent descent method for minimization*, Comput. J., v. 6, (1964).
- [32] Freedonia, *World Gears*, (2015), <https://www.freedoniagroup.com/industry-study/world-gears-3320.html>, 2018.
- [33] B. Schena, *Engineering Fellow*, Intuitive Surgical, (2016).
- [34] Global Wind Energy Council, *Wind Market Forecast*, (2018), <http://gwec.net/global-figures/market-forecast-2012-2016/>, 2018.
- [35] Global Wind Energy Council, *Wind Market Forecast*, (2015), <http://www.gwec.net/wp-content/uploads/2014/04/Market-Forecast-for-2016-2020-1.jpg>, 2018.
- [36] GlobeNewswire, *Top 15 wind suppliers in annual market*, (2015), <http://globenewswire.com/NewsRoom/AttachmentNg/ced854bc-6d00-4da2-a44c-99c53514abc4/en>, 2018.
- [37] Global Wind Energy Council, *Wind in Numbers*, (2016), <http://www.gwec.net/global-figures/wind-in-numbers/>, 2018.
- [38] OffShoreWind.biz, *Report on Wind Turbine Gearbox and Direct-Drive Systems Out Now*, (2014), <https://www.offshorewind.biz/2014/09/19/report-on-wind-turbine-gearbox-and-direct-drive-systems-out-now/>, 2018.
- [39] C. Moné, T. Stehly, B. Maples and E. Settle, *Cost of Wind Energy Review*, NREL, (2014), <http://www.nrel.gov/docs/fy16osti/64281.pdf>, 2018.
- [40] EWEA, *How a wind turbine comes together*, (2014), <http://www.wind-science.org/iresen/Medias>, 2018.
- [41] Youngji, *Looking inside Wind Turbine*, (2015), <https://medium.com/@youngji/looking-inside-wind-turbine-9e2888fb2ee>, 2018.
- [42] D. Ancona and J. McVeigh, *Wind Turbine Materials and Manufacturing Fact Sheet*, Princeton Energy Resources International, (2001), <http://www.perihq.com/documents/WindTurbineMaterialsandManufacturingFactSheet.pdf>, 2018.
- [43] Market Research Report, *Wind Turbine Gearbox and Direct-Drive Systems*, (2014), <https://www.marketresearchreports.com/blog/2014/09/23/wind-turbine-gearbox-and-direct-drive-systems-2014-update>, 2018.
- [44] IFR, *Executive Summary World Robotics*, Industrial Robots, (2017), <https://ifr.org/downloads/press/Executive-Summary-WR-2017-Industrial-Robots.pdf>, 2018.

- [45] Robotics and Automation News, *Top 14 industrial robot companies and how many robots they have around the world*, (2015), <https://roboticsandautomationnews.com/2015/07/21/top-8-industrial-robot-companies-and-how-many-robots-they-have-around-the-world/812/>, 2018.
- [46] Reuters, *China's Midea receives U.S. green light for Kuka takeover*, (2016), <https://www.reuters.com/article/us-kuka-m-a-mideamidea-group/chinas-midea-receives-u-s-green-light-for-kuka-takeover-idUSKBN14J0SP>, 2018.
- [47] Markets and Markets, *Collaborative Robots Market worth 3.3 Billion USD by 2022*, (2016), <https://www.prnewswire.com/news-releases/collaborative-robots-market-worth-33-billion-usd-by-2022-589249891.html>, 2018.
- [48] EV volumes, *Global Plug-in Vehicle Sales for 2017 – Final Results*, (2017), <http://www.ev-volumes.com/country/total-world-plug-in-vehicle-volumes/>, 2018.
- [49] Jose Pontes, *"China December 2017". EV Sales*, (2017), EV Sales, 2018.
- [50] Vaughan, Adam, *Electric and plug-in hybrid cars whiz past 3m mark worldwide*, (2017), The Guardian, 2018.
- [51] Technavio, *Electric Vehicle Transmission - Market Drivers and Forecast*, (2017), <https://www.businesswire.com/news/home/20170106005642/en/Electric-Vehicle-Transmission—Market-Drivers-Forecast>, 2018.
- [52] SKF, *LGHP 2, High performance, high temperature grease*, (2017), <http://www.skf.com/group/products/lubrication-solutions/lubricants/high-performance-high-temperature-grease/index.html> 2018.
- [53] Matrix Specialty Lubricants, *Lubemax WMT, Windmill Transmission Fluid*, (2017), <https://www.matrix-lubricants.com/en/applications/wind-power-industry>, 2018.
- [54] SKF, *Standardized boundary dimensions*, (2017), <http://www.skf.com/group/products/bearings-units-housings/principles/general-bearing-knowledge/bearing-basics/standardized-boundary-dimensions/index.html> 2018.
- [55] SKF, *Cylindrical roller bearings, single row*, (2017), <http://www.skf.com/group/products/bearings-units-housings/roller-bearings/cylindrical-roller-bearings/single-row-cylindrical-roller-bearings/single-row/index.html> 2018.
- [56] Cooper Bearings, *Full Row*, (2017), <https://www.cooperbearings.com/product.asp?prodtype=specialised-bearings&prod=full-row> 2018.
- [57] Odesie, *Chain Drives*, (2017), <https://www.myodesie.com/wiki/index/returnEntry/id/3058>, 2018.
- [58] KSB, *Gear Drive*, (2017), <https://www.ksb.com/centrifugal-pump-lexicon/gear-drive/192346/>, 2018.
- [59] Wikipedia, *Backlash (engineering)*, (2018), [https://en.wikipedia.org/wiki/Backlash\(engineering\)](https://en.wikipedia.org/wiki/Backlash(engineering)), 2018.
- [60] N. Busch, *Collaborative Robots Part 2: Benefits and Expanding Capabilities*, Bastian Solutions,(2017), <https://www.bastianolutions.com/blog/index.php/2017/11/16/part-two-collaborative-robot-benefits-and-capabilities/>, 2018.
- [61] J. Pontes, *EV Sales*, (2017), <http://ev-sales.blogspot.com/2017/01/europe-december-2016.html>, 2018.
- [62] J. Schorsch and R. Deen, *IMSystems Business Plan*, Innovative Mechatronic Systems, (2017), 2018.





## Calculation Tables

**TABLE 14.5.** Values of  $f_0$  vs Bearing Type and Lubrication

Bearing Type	Type of Lubrication			
	Grease	Oil Mist	Oil Bath	Oil Bath (vertical shaft) or Oil Jet
Deep groove ball <sup>a</sup>	0.7–2 <sup>b</sup>	1	2	4
Self-aligning ball <sup>c</sup>	1.5–2 <sup>b</sup>	0.7–1 <sup>b</sup>	1.5–2 <sup>b</sup>	3–4 <sup>b</sup>
Thrust ball	5.5	0.8	1.5	3
Angular-contact ball <sup>a</sup>	2	1.7	3.3	6.6
Cylindrical roller with cage <sup>a</sup>	0.6–1 <sup>b</sup>	1.5–2.8 <sup>b</sup>	2.2–4 <sup>b</sup>	2.2–4 <sup>b,d</sup>
full complement	5–10 <sup>b</sup>	—	5–10 <sup>b</sup>	—
Spherical roller <sup>c</sup>	3.5–7 <sup>b</sup>	1.7–3.5 <sup>b</sup>	3.5–7 <sup>b</sup>	7–14 <sup>b</sup>
Tapered roller <sup>a</sup>	6	3	6	8–10 <sup>b,d</sup>
Needle roller	12	6	12	24
Thrust cylindrical roller	9	—	3.5	8
Thrust spherical roller	—	—	2.5–5 <sup>b</sup>	5–10 <sup>b</sup>
Thrust needle roller	14	—	5	11

<sup>a</sup>Use  $2 \times f_0$  value for paired bearings or double row bearings.  
<sup>b</sup>Lower values are for light series bearings; higher values are for heavy series bearings.  
<sup>c</sup>Double row bearings only.  
<sup>d</sup>For oil bath lubrication and vertical shaft, use  $2 \times f_0$ .

Figure A.1: Values for  $f_0$  [11]

**TABLE 14.6.** Values of  $f_f$  for Radial Cylindrical Roller Bearings

Bearing Type	Type of Lubrication	
	Grease	Oil
With cage, optimum design	0.003	0.002
With cage, other designs	0.009	0.006
Full complement, single row	0.006	0.003
Full complement, double row	0.015	0.009

Figure A.2: Values for  $f_f$  [11]**TABLE 14.3** Values of  $z$  and  $y$ 

Ball Bearing Type	Nominal Contact Angle	$z$	$y$
Radial deep groove	0°	0.006–0.004 <sup>a</sup>	0.55
Angular contact	30–40°	0.001	0.33
Thrust	90°	0.0008	0.33
Double-row, self-aligning	10°	0.0003	0.40

<sup>a</sup>Lower values pertain to light series bearings; higher values pertain to heavy series bearings.

Figure A.3: Values for  $z$  and  $y$  [11]**TABLE 14.4.**  $f_1$  Roller Bearings

Roller Bearing Type	$f_1$
Radial cylindrical with cage	0.0002–0.0004 <sup>a</sup>
Radial cylindrical, full complement	0.00055
Tapered	0.0004
Radial needle	0.002
Thrust cylindrical	0.0015
Thrust needle	0.0015
Thrust spherical	0.00023–0.0005 <sup>a</sup>

<sup>a</sup>Lower values pertain to light series bearings; higher values pertain to heavy series bearings.

Figure A.4: Values for  $f_1$  for roller bearings [11]

**TABLE 21.4.** Values of  $X_s$  and  $Y_s$  for Radial Ball Bearings

Bearing Type	Single-Row Bearing		Double-Row Bearing	
	$X_s$	$Y_s^b$	$X_s$	$Y_s^b$
Radial contact groove ball bearing <sup>a,c</sup>	0.6	0.5	0.6	0.5
Angular-contact groove ball bearings				
$\alpha = 15^\circ$	0.5	0.47	1	0.94
$\alpha = 20^\circ$	0.5	0.42	1	0.84
$\alpha = 25^\circ$	0.5	0.38	1	0.76
$\alpha = 30^\circ$	0.5	0.33	1	0.66
$\alpha = 35^\circ$	0.5	0.29	1	0.58
$\alpha = 40^\circ$	0.5	0.26	1	0.52
Self-aligning ball bearings	0.5	0.22 ctn $\alpha$	1	0.44 ctn $\alpha$

<sup>a</sup> $P_o$  is always  $\geq F_r$ .

<sup>b</sup>Values of  $Y_o$  for intermediate contact angles are obtained by linear interpolation.

<sup>c</sup>Permissible maximum value of  $F_a/C_o$  depends on the bearing design (groove depth and internal clearance).

Figure A.5: Values for X and Y for radial ball bearings [11]

**TABLE 21.5.** Values of  $X_s$  and  $Y_s$  for Radial Roller Bearings<sup>a</sup>

Bearing Type	Single-Row Bearings <sup>b</sup>		Double-Row Bearings	
	$X_s$	$Y_s$	$X_s$	$Y_s$
Self-aligning and tapered roller bearings $\alpha \neq 0^\circ$	0.5	0.22 ctn $\alpha$	1	0.44 ctn $\alpha$

<sup>a</sup>The ability of radial roller bearings with  $\alpha = 0^\circ$  to support axial loads varies considerably with bearing design and execution. The bearing user should therefore consult the bearing manufacturer for recommendations regarding the evaluation of equivalent load in cases where bearings with  $\alpha = 0^\circ$  are subjected to axial load.

<sup>b</sup> $F_s$  is always  $\geq F_r$ . The elastic equivalent radial load for radial roller bearings with  $\alpha = 0^\circ$ , and subjected to radial load only is  $F_s = F_r$ .

Figure A.6: Values for X and Y for radial roller bearings [11]